QUANTITATIVE IMAGE ANALYSIS OF PERIPHERAL NERVES IN WHIPLASH INJURY PATIENTS

BY

KAMAKSHI PRADEEP ANANTHARAMAN

A thesis submitted for the degree of Doctor of Philosophy in Engineering in the Department of Engineering & Informatics At the University of Sussex

SEPTEMBER 2017

Declaration

I hereby declare that this thesis has not been and will not be submitted in whole or in part to another University for the award of any other degree.

Signed: Kamakshi P. A.

Date: 07th September 2017

Acknowledgements

I would like to thank the following people, if not for them, this work would not have been possible.

- My supervisor Dr. Rupert Young for being very supportive and patient with me during my research.
- My second supervisor Dr. Phil Birch for his constant timely advice and support.
- My husband Pradeep and our son Aniruddha for being the pillars of my strength and motivators during my research.
- My parents and in-laws for believing in my goals and supporting me.
- My siblings Kamini and Kaustubh for encouraging me to follow my heart and pursuing this research degree.
- E&D department colleagues for all the administrative support during my PhD.
- I would like to thank Dr. Andrew Dilley and Dr. Jane Greening of the Brighton and Sussex Medical School for their collaboration in providing data and their support for the thesis research.

Abstract

The research in this thesis has examined the use of texture and shape analysis to characterise Magnetic Resonance (MR) images of peripheral nerves in order to provide a potential quantitative tool for better diagnosis and treatments.

Texture and shape can be considered as inherent properties of all surfaces and have the potential to provide sensitive information which cannot be quantitatively perceived by human vision. Texture analysis has been successfully used in image classification of aerial and satellite imagery and the diagnosis and prognosis of several types of cancer. However, to date, it has never been used in investigating peripheral nerve damage. In this thesis, we study the application of texture and shape analysis to the peripheral nerves in the upper extremities of patients suffering from Whiplash Associated Disorders (WAD).

Specifically, quantitative texture analysis was performed on MR images of the carpal tunnel which contains the median nerve. The median nerve was studied to identify differences in textural patterns. Texture methods such as: first order features; co-occurrence matrices; run-length matrices and autocorrelation function were applied and their performance was assessed. Texture analysis was also performed to investigate nerve damage in the MR images of the brachial plexus, both in controls and patients.

Further, spatial domain shape metrics were used to quantify and study the morphological differences of the median nerve in controls and patients. This highlighted that some significant differences exist between groups and thus could potentially be reliably used in combination with clinical scale metrics to identify possible nerve damage.

As MR images contain noise, locating the median nerve accurately to perform image analysis is very important. Therefore, we further investigated the application of an enhanced correlation filtering method that could be trained on images of the median nerve and then applied to detect the median nerve in test images. The Optimal Trade-off Maximum Average Correlation Height (OT-MACH) filter includes the expected distortions in the target in the construction of the filter reference function. The OT-MACH filter was tuned in a bandpass to maximize the correlation peak and thereby successfully locate the position of the median nerve in the carpal tunnel.

This study has successfully demonstrated that texture and shape analysis can be used to investigate possible peripheral nerve damage. Further research is required using larger datasets to establish a quantitative image analysis tool to support clinical decision making and thereby improve patient care and treatment outcome.

Publication

Evidence for increased MRI signal intensity and morphological changes in the brachial plexus and median nerves of patients with chronic arm and neck pain following whiplash injury.

Jane Greening, Kamakshi Anantharaman, Rupert Young, Andrew Dilley

Submitted to the Journal of Orthopaedic and Sports Physical Therapy **(Accepted for Publication)**

Table of Contents

List of Figures

List of Tables

List of Symbols

μ	Mean
σ^2	Variance
μ^3	Skewness
μ^4	Kurtosis
E	Energy
H	Entropy
ϕ	Angle
α	Non-negative parameter
β	Non-negative parameter
γ	Non-negative parameter
σ	Standard Deviation

List of Abbreviations

ANN	Artificial Neural Networks
ASM	Average Similarity Measure
ATR	Automatic Target Recognition
BP	Brachial Plexus
COPI	Correlation Output Peak Intensity
CT	Carpal Tunnel
CT	Computed Tomography
CTS	Carpal Tunnel Syndrome
CUReT	Columbia- Utrecht Reflectance and Texture database
DCE-MRI	Dynamic Contrast Enhance Magnetic Resonance Imaging
DCIS	Ductal Carcinoma *In Situ*
DICOM	Digital Imaging and Communications in Medicine
DNN	Diffusion Neural Network
GLCM	Gray Level Co-occurrence Matrix
GLN	Gray Level Non-uniformity
HGRE	High Gray Level Run Emphasis
IDC	Invasive Ductal Carcinoma
LGRE	Low Gray level Run Emphasis
LRE	Long Run Emphasis
LRHGE	Long Run High Gray level Run Emphasis
LRLGE	Long Run Low Gray level Run Emphasis
MACE	Minimum Average Correlation Energy filter
MACH	Maximum Average Correlation Height filter
MGL	Mean Grey Level
MRI	Magnetic Resonance Imaging
MRN	Magnetic Resonance Neurography
MTD	Mega-Trend-Diffusion
MVSDF	Minimum Variance Synthetic Discriminant Function

NPV	Negative Predictive Value
NSAIDs	Non-Steroidal Anti- Inflammatory Drugs
NSCLC	Non-Small Cell Lung Cancer
ONV	Output Noise Variance
OT-MACH	Optimal Trade-Off Maximum Average Correlation Height Filter
PCA	Principal Component Analysis
PCE	Peak Correlation Energy
PET	Positron Emission Tomography
PPV	Positive Predictive Value
PSR	Peak -to- Sidelobe Ratio
PTSD	Post Traumatic Stress Disorder
RBF	Radial Basis Function
RLM	Run Length Matrix
RLN	Run Length Non- uniformity
RP	Run Percentage
RU Joint	Radioulnar Joint
SDF	Synthetic Discriminant Function
SEM	Standard Error of the Mean
SF-36	Short Form survey No-36
SI	Systems International
SPECT	Single Photon Emission Computed Tomography
SRE	Short Run Emphasis
SRHGE	Short Run High Gray level run Emphasis
STIR	Single Tau Inversion Recovery
SVM	Support Vector Machines
TA	Total Accuracy
TENS	Transcutaneous Electric Nerve Stimulation
TNR	True Negative Rate
TPR	True Positive Rate
VANET	Vehicular Ad-hoc Networks

VGL	Variance in Grey Level
WAD	Whiplash Associated Disorders

Chapter 1

Introduction

1.1 Introduction

Medical image processing was born because of advancements in medical imaging that took place in the last century. From x-rays to computed tomography, the past decades have seen incremental progress in the science and technology of imaging. Computed tomography enabled three-dimensional reconstruction of the human body. Hence, the need for accurate image reconstruction and visualization became of interest to scientists. Computers became more powerful and the necessity to analyse the improving images to find what the human eye could not perceive became a highly-researched area. A major proportion of the interpretation was possible using mathematical models and translating them into programming with specific techniques. This field came to be known as medical image analysis. Over the past two decades, computer algorithms became more complex and artificial intelligence models were also developed to interpret medical image data with the same flexibility as a human observer [1].

Medical Imaging can be described as a technique or process of creating a visual representation of the interior of a human body for clinical analysis and medical intervention. It helps build a database of information about normal anatomy and physiology and therefore helps identify abnormalities. Medical imaging is a combination of the fields of biomedical engineering, physics and computer science. As a crucial field

of scientific investigation in medicine, imaging modalities designate techniques that non-invasively produce images of the internal aspects of the body [2].

In a report by the European Science Foundation, it is described how medical imaging has changed the face of patient care. Medical imaging plays a central most crucial role in the healthcare system as it contributes to efficient diagnosis of diseases. It is important that diseases are diagnosed at the earliest stages, so treatment can be accurate for best patient outcome. Medical Imaging technology is growing at a rapid pace not only in the clinical setting in hospitals but also in research and development. Research in imaging is on two levels, namely: the biological study of the interior of the human body done by the medical specialist; secondly, research is done on the images derived from the imaging modalities by processing these images. Image processing of this medical data is proving to be very important in a supportive role to medical specialists [3]. This report states that medical imaging has a key role in the care of all organ systems and disease entities, and better and increased medical imaging research may benefit the entire process of health and disease management, including:

- prevention
- screening targeted sub-populations with increased risk of specific disease entities
- early detection of subclinical disease
- optimal choice of treatment based on personalised medicine
- prognosis
- non-invasive monitoring of treatment effects for response-adjusted treatment in case of poor response
- patient follow-up to adjust multi-drug therapy in chronic disease
- early detection of recurrence
- decision making tool for early-onset disease treatment and monitoring

- improved patient care
- early detection of life threatening diseases and recurrences of certain diseases
- individually tailored treatments
- lesser complications during and after surgeries
- more evidence-based decision making within healthcare
- better understanding and monitoring of how well the treatment is working for the patient

1.2 Problem Outline

In this thesis, quantitative image analysis is performed to investigate and analyse peripheral nerves in subjects who had suffered from whiplash injury in the past. These subjects had made full recovery after the motor accident; however, they slowly developed chronic pain in arms, shoulders and wrist which had no accompanying clinical manifestation. This study is a preliminary attempt to identify if medical image analysis can be used to characterise the peripheral nerves in the upper extremities of these subjects to investigate the cause of the chronic pain in whiplash injuries. This study used quantitative texture and shape techniques to analyse the peripheral nerves in the brachial plexus and the carpal tunnels of all the subjects that participated in this study. Texture analysis was done using first order features, co-occurrence matrices and run length matrices. Quantitative shape analysis was also performed using spatial domain shape metrics such as circularity, aspect ratio and other morphological features of the median nerve in the carpal tunnel.

1.3 Problem Rationale

Whiplash injury is one of the most common causes of neck injury and it occurs during rear-end collisions in motor vehicle accidents. The collision is believed to cause immense trauma when the head suddenly moves forward and then is pushed backwards due to the impact of the collision.

The most crucial problem is the diagnosis of whiplash. Although there are set guidelines to investigate the trauma caused by whiplash, it relies heavily on the doctor's judgement and the patient's description of how and where they feel pain which in some cases can be vague and irrelevant. There is a pressing need for development of a supportive tool that would help improve the diagnosis of whiplash and thereby improve patient care and treatment outcome.

The second most crucial issue regarding whiplash injuries is the economic burden it carries. In 2012, a report written by the Ministry of Justice investigated a consultation report concerning whiplash injuries in England and Wales. The report indicated that between 2006 and 2010, almost seventy percent of the road traffic accident personal insurance claims were for whiplash injuries. This rate was significantly higher than any other country in the then European Union. According to the Association of British Insurers, approximately ninety pounds of the cost of an average motor insurance premium stems from the cost of whiplash injuries. Whiplash injuries account for nearly two billion pounds of compensation payments per year [4]. The report also summarised the points based on which the government accepted that whiplash injury was a complex issue that needed attention. They decided to work on four areas of focus in order to make progress. These areas are listed below [5]:

- Improving the diagnosis of a whiplash injury

- Developing standards for diagnosis
- Challenging questionable claims
- Tackling the perception that exaggerated claims are acceptable.

The work in this thesis is an attempt to improve the diagnosis of whiplash injury by using advanced medical image analysis. To the best of our knowledge, no supportive tools or methods exist that are approved to be used by medical experts in diagnosis of whiplash injuries using medical imaging analysis. In this thesis, we investigated the hypothesis that application of quantitative image analysis could improve the diagnosis and treatment of whiplash associated disorders and symptoms and that it will provide a supportive tool to medical practitioners.

The next section explains what whiplash injury is and presents the relevant literature that will help understand the current procedures and techniques used in its diagnosis.

1.4 Whiplash Injury

The term “whiplash” was coined by an American orthopaedist Dr. H. E. Crowe in 1928. He described it as trauma caused to the soft tissues in the cervical spine from a sudden acceleration-deceleration force mechanism such as that which occurs in rear-end collisions in motor accidents [6]. As can be seen in the figure 1.1 below, there are phases of events that occur in cases of rear end collision. When the vehicle is hit from the rear end, the normal resting human body is forced back into the seat. This immediately affects the normal lordosis of the neck and it is forced to lose curvature and straighten. After the impact, the head and neck both move backwards until the acceleration has reached its peak and if the motor vehicle driver then has hit the brakes, deceleration occurs instantaneously throwing the head and neck into hyperflexion, as shown below. This throws the body and head forward. In this case, the body is held in position by the seat

belt; however, the neck and head decelerate forward. The impact of this collision can produce symptoms and injury at various levels of emergency [7]

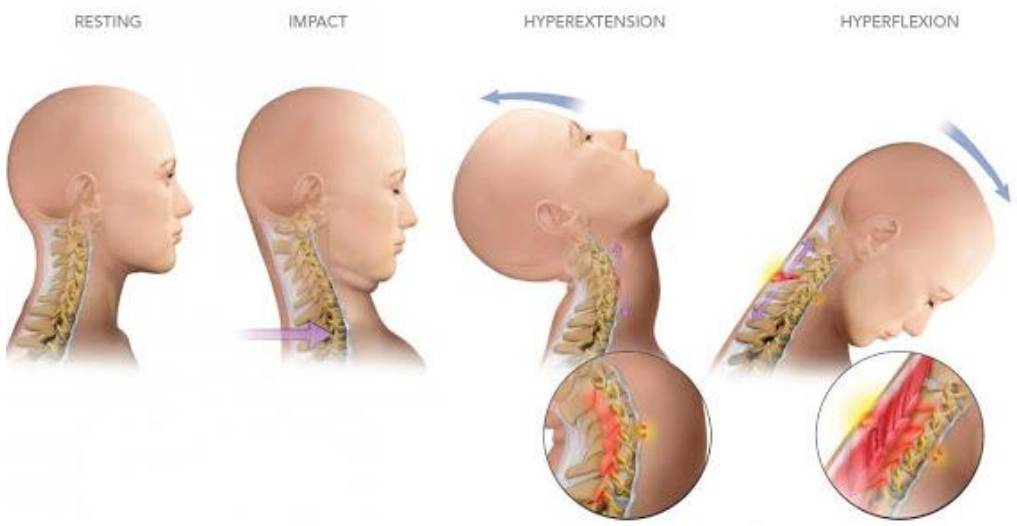

Figure 1.1: Phases of trauma caused during rear-end collision[8]

The history of whiplash is said to have its roots dating back to 1866, when the British physician Erichsen described the term “railway spine”. He explained in his lectures that although railway accidents sometimes had no evident blow or injury to the head or spine of the patients at the time of impact, it seemed to have caused trauma to the entire human nervous system therefore causing an array of clinical manifestations as all the patients presented similar symptoms of anxiety and depression which completely disrupted their normal way of life [6].

There is striking analogy in how the theories around railway spine evolved and similarly how the theories about whiplash injuries have evolved in the past four decades. The term ‘whiplash’ however has had many definitions over the years. The simple aspect of driving and using a motor vehicle has many socio-legal aspects to it such as insurance claims, insurance premium costs and legal compensations which have a tremendous impact on the economy of a nation. As these motor accidents not only caused direct injuries on

impact and led to many associated injuries that range from very minor sprains to severe damage leading to disability or impairment of a permanent nature, it was crucial that there was consistency in how whiplash injury was looked at. To tackle these clinical, socio-economic and legal concerns, a Canadian car insurance company set up a task force of experts from all the relevant fields to investigate whiplash injuries and set up a classification system which would make diagnosis, prognosis and treatments consistent. The result was the document called "Quebec Task Force Guidelines for Whiplash Associated Disorders". Whiplash associated disorders (WAD) encompass many clinical manifestations that follow whiplash injury such as neck pain, arm pain, memory impairment, poor concentration, anxiety and depression and the obvious physical trauma such as neck fractures or dislocation [6]. The following table lists the Quebec Task Force Whiplash Associated Disorders (WAD Classification) Scheme.

Grade	Injury and Symptoms	Signs
Grade 0 or WAD0	No complaints of neck pain or any possible physical injury	No physical sign or manifestation observed of any injury by medical practitioner.
Grade 1 or WAD1	Muscle sprain, neck stiffness, neck pain or tenderness in the cervical area	Normal motor range, normal reflexes and muscle strength in the limbs. X-ray is not necessary in this case.
Grade2 or WAD2	Possible muscle and/or ligament sprain. Neck and/ or back pain.	Tenderness in paraspinal muscles and restricted range of motion in spine. Normal reflexes and muscle strength in the limbs. X-ray shows no fracture/dislocation.
Grade3 or WAD3	Possible disc protrusion with nerve root impingement or spinal cord contusion without bony fracture/dislocation. Neck pain; back pain, arm pain; leg pain and numbness.	Reduction or absence of reflexes; muscle weakness; sensory changes; or all, suggestive of a nerve root injury or compression in the spinal cord. X-ray shows no fracture or dislocation.
Grade4 or WAD4	Cervical Fracture and/or dislocation. Neck pain, or neurological symptoms in limbs, urinary incontinence due to the involvement of the spinal cord.	Motor weakness and sensory changes if spinal cord is injured. X-ray shows fracture, dislocation or both if present. CT or MRI may show spinal injury.

Table 1.1: Quebec Task Force Whiplash Associated Disorders Classification Scheme [6] [7]

Thus, from the above classification, we can infer that adequate medical intervention is not advised at Grade 1 and Grade 2. However, the chronic pain resulting from whiplash often falls in the Grade 2 category shown in Table 1.1 and therefore patients suffer from endless pain without prescriptions to treat it fairly. In a paper by Sterling *et al*. [9] it is discussed that whiplash is a very significant public health problem with immense social and financial burden arising from patients who are involved in motor vehicle accidents and therefore suffer chronic pain and associated disability. According to a study on

Australian data in this paper, 60 % of people are said to report pain 6 months to 2 years post the motor vehicle accident. Therefore, whiplash is said to cause psychological and physical distress in patients very like post-traumatic stress disorder (PTSD).

It is important to understand the impact of neck and arm pain on the overall health status of an individual. The findings of a study by Daffner *et al.* [10] are discussed below. This study primarily focused on the effects that cervical spine conditions causing neck and or arm pain have on individuals' overall wellbeing. The study was conducted on SF-36 (Medical Outcomes Study) health survey data which is a multipurpose survey with 36 questions used to assess eight subscales and two summary scales which are scored from 0 to 100. The subscales record physical functions, bodily pain, general health, vitality, emotional and mental health and social functioning. The summary scales segregate the finding into a physical component scale and a mental component scale. Higher scores suggest better function. The three main findings of the study were: (i) patients with both neck and arm pain had significantly lower scores than those with either or isolated neck and arm pain; (ii) patients of working age i.e. <60 were adversely impacted by their symptoms as compared to older patients across all subscales; and (iii) longer symptom duration was associated with negative impact on mental health status. Although this study was not directly conducted on whiplash patients, the findings are relevant as whiplash associated injuries also arise from cervical spine trauma [10]. Identifying and investigating chronic pain beyond primary clinical care assessment is crucial and calls for a strong supportive framework for clinicians to implement evidence-based methods to treatment of chronic pain.

1.5 Diagnosis and Treatment

Peripheral neuropathies in most cases are evaluated by clinical examinations, electroneurography and electromyography. These techniques look at the structure of the nerves, the electrophysiological characteristics such as nerve conduction slowing, or complete block of conduction. Earlier, magnetic resonance imaging has been used for imaging peripheral nervous tissue for detection of focal intrinsic and extrinsic nerve lesions and it has been found to reveal alterations that were un-detected in electrophysiological examinations. The term magnetic resonance neurography was coined in the 1990s. It denoted the application of specific MR pulse sequences to visualize peripheral nerves and to differentiate them from the surrounding soft tissues [11]. This study summarised how both ultrasound and magnetic resonance imaging could provide information of the site and extent of the nerve injury. Although, ultrasound is more extensively used in such investigations, magnetic resonance provides superior soft-tissue contrast and better image quality of the nerve structures. In this study, MR images of the brachial plexus and carpal tunnel are used in the investigation; the MRI protocol is discussed in the following chapter.

The generic treatment prescribed for neck trauma in whiplash is the use of a Philadelphia collar for not less than two weeks. To address asymptomatic and symptomatic pain, administration of analgesics such as nonsteroidal anti- inflammatory drugs (NSAIDs) and myorelaxants is prescribed, respectively. To restore muscle tone and strength, physical training exercises and stretching are advised to correct posture and kinematics of the cervical spine. These are in some cases combined with physio-kinetic therapies, massage therapy, transcutaneous electric nerve stimulation (TENS) and ultrasound which all have pain supressing action. Surgical treatments are recommended only for permanent instable

forms such as articular and pillar fractures with protrusions, unilateral dislocations, severe sprains and discal hernias with medullar radicular lesions [7].

As this study involves application of texture and shape analysis to the MR images of the brachial plexus and carpal tunnel, the following section provides a brief overview of the anatomy of BP and CT and discusses the areas of interest in this study.

1.6 Anatomy of the Carpal Tunnel

The carpal tunnel (CT) is a canal located at the volar wrist. It is surrounded by the carpal bones and flexor retinaculum also known as the transverse carpal ligament. The carpal tunnel contains the median nerve and nine tendons. A detailed description of the carpal anatomy can be found in [7].

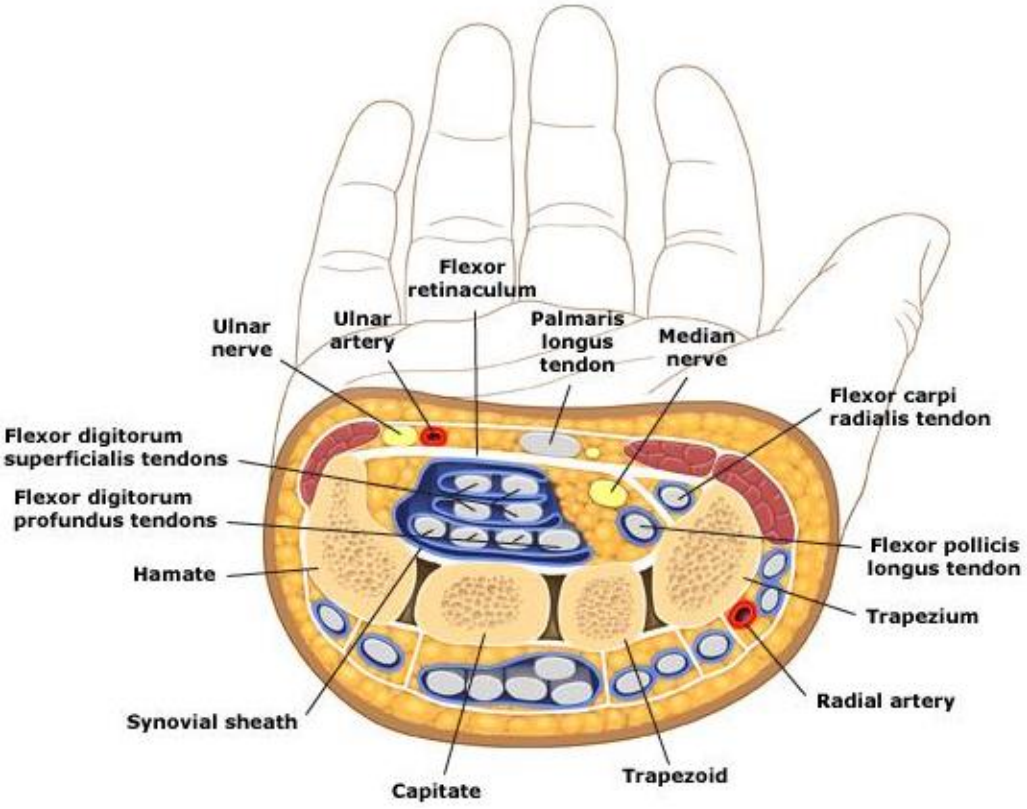

Figure 1.2: Anatomy of the carpal tunnel [12]

1.7 Anatomy of the Brachial Plexus

The brachial plexus is formed by articulation among the roots of four cervical nerves C5 to C8 and the first thoracic nerve T1. The brachial plexus oversees motor innervation of all muscles in the upper extremity. The median nerve is derived from the brachial plexus and runs through the upper arm into the forearm and then into the carpal tunnel as shown in the figure1.2 above. The detailed analysis of the brachial plexus anatomy can be found in [13]. Figure 1.3 below shows the anatomical structure of the brachial plexus.

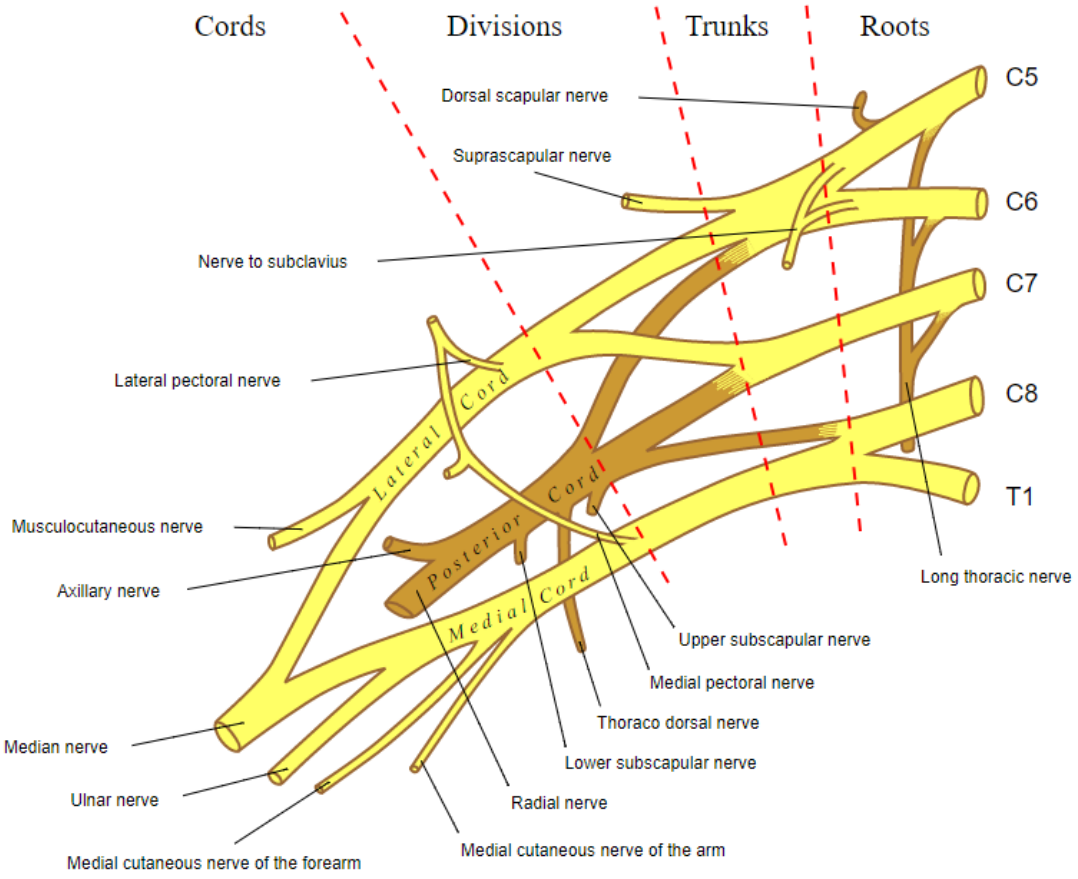

Figure 1.3: Anatomy of the Brachial Plexus [13]

1.8 Imaging in Peripheral Neuropathies

Medical image processing has become possible due to the enormous advancements in the medical imaging modalities used for capturing digital image data. Some of the widely used imaging modalities are X-rays, computed tomography (CT), magnetic resonance imaging (MRI), ultrasound, single photon emission computed tomography (SPECT) and positron emission tomography (PET) [1]. According to a study by Stoll *et al.* [11] the imaging of the peripheral nervous system using MRI and ultrasound has become a prominent choice in investigating nerve disorders and these are now being used in parallel with clinical examinations to investigate neuropathies [10]. However, clinical evaluations remain an integral part of nerve disorder investigations together with electromyography and nerve conduction studies [10]. A brief description of the ultrasound and MRI techniques is presented below.

1.8.1 Ultrasound Imaging

As the name suggests, this imaging technique uses the physics of sound propagation to create a two-dimensional real-time representation of the interior of the body. It consists of a transducer sensor that propagates sound waves and the reflection is picked up by athe receiver. The time taken for the waves to travel and then return to the receiver as an echo is translated into the depth of the echo source depending on the surface they hit such as different soft tissues and organs. Most of the ultrasound scanners used today use digital signal and image processing techniques [1].

1.8.2 Magnetic Resonance Imaging

In Magnetic Resonance Imaging (MRI), the patient is placed within an MRI scanner which forms a strong magnetic field around the area to be imaged. Then radiofrequency pulses producing an electromagnetic field are transmitted in a plane perpendicular to the magnet, resulting in protons becoming excited and moving out of their original position. When the protons return to their baseline state i.e. relax, energy is produced which can be transduced and in turn be translated into images. MRI scanning can discriminate between body substances based on their physical properties such as water and fat content in tissues. In MR images, some parts appear darker or brighter depending on the density of protons in that area, an increased density being associated with the darker area [1].

MRI requires a magnetic field that is both strong and uniform. The field strength of the magnet is measured in the SI unit of Tesla – and while the majority of systems operate at 1.5T, commercial systems are available between 0.2T–7T. Relaxation times for protons can vary and two times are commonly measured known as T1 and T2. T1 weighted images are useful for assessing cerebral cortex, identifying fatty tissues, characterizing focal liver lesions and in general for obtaining morphological information. T2 weighted images are used in detecting oedema and inflammation, revealing white matter lesions and assessing zonal anatomy in the prostrate and uterus.

It is an established fact that MRI is very good at soft tissue differentiation and it is widely used in investigating nerve lesions. Standard evaluation of peripheral nerves using MRI is done by using fluid sensitive fat suppressed heavily weighted T2 pulse sequences such as short tau inversion recovery (STIR) [14]. During an injury, the water content in the soft tissue increases causing a hyper-intense signal on MRI. [14]. The term magnetic resonance neurography was coined by Filler *et al.* [15]. In this study, they attempted to

use heavy weighted T2 pulse sequences to suppress surrounding tissue and render nerve as the brightest structure in an image. It shows how MRI helps in imaging the nerve but altering the pulse sequences gives better visibility by fat suppression using STIR as initially explained in [14].

In a study by Middleton *et al.* [16], MR imaging was used to investigate the carpal tunnel syndrome (CTS) in 10 patients suffering from CTS. CTS is a peripheral neuropathy caused by compression of the median nerve in the carpal tunnel. This can be caused by numerous causes such as diabetes, hypothyroidism and rheumatoid arthritis. This study identified MRI as the best method to image the carpal tunnel anatomy as the T2- weighted images helped identify the contents of the carpal tunnel accurately. The tendons, median nerve thickness and the carpal ligament were clearly visible for morphological analysis [16].

In another similar study by Pierre-Jerome *et al.* [17], MR imaging was used to quantify the morphological changes of the carpal tunnel after operative intervention in CTS. The study investigated 28 patients who underwent a total of 31 surgical interventions to relieve the compression in the carpal tunnel. MR imaging was performed before and after the operation. The morphological analysis was performed by assessing the area and volume of the carpal tunnel and the signal intensity emitted by the T2-weighted images of the median nerve. The results showed a decrease in signal intensity of the median nerve suggesting the successful decompression of the nerve after the surgery [17].

MRI has also been extensively used for investigating brachial plexus injury. A study by Yoshikawa *et al.* [18]investigates the different clinical manifestations of a brachial plexus injury and studies the imaging techniques used in evaluating the brachial plexus. It shows

how signal intensity changes in the spinal cord, nerve roots and paraspinal muscles indicate the presence of brachial pathology [18].

In a study by Andrew *et al.* [19] magnetic resonance neurography was used to study the nerve degeneration and regeneration in a 29-year-old patient who had a traumatic laceration of the right sciatic nerve in the lower thigh. T2 magnetic resonance neurography showed increased signal in the peroneal nerve distal to the site of traumatic injury at 4 months and 6 months after the emergency surgery. This indicated the degeneration of the nerve. A second surgery was performed to remove the degenerated nerve segment and grafting was done to bridge the gap. Eight months after this surgery, MRN started showing regeneration of the nerve with reduced signal intensity which was attributed to recovery and normalisation of the injury. This study specifically illustrated the ability of MRN to detect increased signal on T2 sequences in a traumatically injured degenerating human peripheral nerve. It provided evidence that chronically degenerated peripheral nerve could show increased signal for at least 3 years following trauma without recovery [19]. This study directly correlates to the kind of investigation being undertaken in this thesis and hence it can be inferred that the increase in signal intensity of the peripheral nerve in the brachial plexus and carpal tunnel could signal a pathology and quantifying this is of the utmost importance.

MR Neurography is therefore increasingly being used for evaluation of peripheral nerves. An interesting review of MR neurography is presented by Chhabra *et al.* [20]. It discusses how fat-suppressed T2-weighted images can be evaluated accurately using MR neurography. MR neurography allows accurate assessment of nerve intensity, fascicular pattern, size and perineural fibrosis or mass of nerve lesions. With further improvement in MR contrast agents and diffusion-based nerve and muscular imaging, MRN is likely to play a strong role in diagnosis and treatment of peripheral disorders [20].

1.9 Description of Data

Twenty-three subjects were recruited for the study, which included ten patients diagnosed with whiplash associated disorder and thirteen healthy control subjects. One patient withdrew from the study prior to imaging. The patients were recruited through physiotherapy clinics following a diagnosis of whiplash associated disorder. Patients were included if they met the Quebec Task Force Classification of whiplash grade II (neck complaints and musculoskeletal signs, including decreased range of motion and point tenderness in the neck) only and symptoms had been present for more than three months. All patients had painful symptoms in the upper limb. Patients were excluded if they were diagnosed with whiplash grade III (obvious neurological signs) or IV (fracture or dislocation), or if they had experienced concussion, loss of consciousness or head injury because of the accident, or they have reported a history of whiplash, neck pain or headaches that required treatment. Patients were also excluded if they reported any systemic illness, such as an endocrine, cardiovascular or metabolic disorder.

1.10 MRI Protocol

Magnetic resonance imaging (MRI) of the brachial plexus and wrist was performed using a Siemens 1.5 Tesla MRI. During imaging of the brachial plexus, all subjects were fitted with a head and neck transmit-receive radiofrequency coil. Coronal images of the proximal brachial plexus (roots and trunks) were obtained using a T1-weighted (TE = 17ms, TR = 518ms) and a T2-weighted short tau inversion recovery (STIR) sequence with flow suppression (TE = 78ms, TR = 5340ms and TI = 160ms; slice thickness = 3mm). In a short tau inversion recovery sequence, the spin echo is completed by a previous 180-degree inversion pulse. Fat has a short T1. Hence, by using a short T1, fat - suppressed images can be acquired with faster acquisition timings. As fat appears as a

hyper-intense signal, fat suppression is key to imaging the hyper- intense peripheral nerves [21]. T1-weighted images were used for anatomical reference. During imaging of the wrist, the most symptomatic side was imaged in patients, or dominant side in control subjects. An arm coil was positioned at the level of the carpal tunnel. Transverse images of the median nerve were obtained through the carpal tunnel, from the distal radio-ulnar joint to the base of the metacarpals, using a T1-weighted sequence (TE = 12ms, TR = 540) and a T2-weighted STIR sequence with flow suppression (TE = 76ms, TR = 3940ms and TI = 160ms; slice thickness = 3mm). MRI sequences were aligned perpendicular to the nerve axis. The slice thickness was 3mm.

1.11 Image Analysis Software

The image analysis done as a part of this thesis work was done using MATLAB R2017a. MATLAB is a multi-paradigm numerical computing environment and fourth generation programming language [22]. It allows matrix manipulations, plotting of functions and data, implementation of algorithms, creation of user interfaces and interfacing with programs written in other languages, including C, C++, Java, Fortran and Python. It comes with an Image Processing toolbox which provides a comprehensive set of reference-standard algorithms, functions and applications for image processing (Mathworks Inc. Natick, MA, USA).

1.12 Thesis Organisation and Summary of Achievements

An effort has been made in this thesis to study the application of quantitative texture and shape analysis methods to characterise the peripheral nerves in the brachial plexus and the carpal tunnel of patients suffering from whiplash associated disorders.

Chapter 1- Introduction

In this chapter, an overview of the work in the thesis is presented. The problem outline and problem rationale are discussed. A brief clinical background of whiplash injuries is provided followed by distinct aspects of medical image analysis such as imaging modalities and image analysis techniques. The chapter is concluded with an overview of the data that has been used in this thesis. A summary of the content of each chapter of the thesis and the achievements of research conducted is given below.

Chapter 2- Application of texture analysis using first order features and co-occurrence matrices

In this chapter, a detailed description of texture analysis methods is presented together with their applications in medical and non-medical fields. The application of first order features and gray level co-occurrence matrices to study the texture of the median nerve in the carpal tunnel is discussed with results and analysis.

Chapter 3- Application of texture analysis using Run Length Matrix and Autocorrelation

In this chapter, the application of gray level run lengths is investigated. The gray level run lengths are calculated for the median nerve in the carpal tunnel and the

nerve segments in the brachial plexus of the subjects involved in the study. Features are then extracted from these matrices to help characterise the texture of the nerves. The results are presented followed by statistical analysis to identify the features that demonstrate statistical significance in quantifying the nerves.

The two-dimensional autocorrelation function is computed for the nerve images. The texture signature is derived from the autocorrelation function for both x and y directions of the image. Features such as peak intensity values, peak widths and peak prominence are investigated to differentiate the patient nerves from the control nerves.

Chapter 4- Application of spatial domain shape metrics to study the deformation of the median nerve in the carpal tunnel

In this chapter, shape analysis is performed to investigate the deformation of the median nerve in the control group and patient group. Spatial domain shape metrics such as circularity, aspect ratio, nerve area and perimeter are used to distinguish the median nerve in patients from that in controls. The results are presented followed by a statistical analysis to identify statistically significant shape metrics.

Chapter 5- Application of the Optimal Tradeoff Maximum Average Correlation Height Filter (OT-MACH) to detect the median nerve in the carpal tunnel

In this chapter, an advanced correlation filter, the OT-MACH filter, is implemented to detect the location of the median nerve in the carpal tunnel. The application of this unconstrained correlation filter is investigated as it offers robust tolerance to intra-class variation in the median nerve whilst maintaining inter-

class discrimination. The results are presented for different experimental scenarios.

Chapter 6- Classification using features extracted from image data

In this chapter, a Support Vector Machine (SVM) classifier is used to classify median nerves as belonging to the patient or control group. The performance of SVM in binary classification of the small dataset is tested and the results are discussed. Principal component analysis (PCA) is used for dimensionality reduction of texture features to identify the principal components that effectively differentiate the patterns in the data. The results expressed in terms of accuracy, sensitivity and specificity of the classification methods are presented.

Chapter 7- Conclusions and future work

In this chapter, a synopsis of the thesis results is presented. The results are analysed and the feasibility of implementing the work in this thesis for clinical support is discussed. The opportunities for future work in this area are considered. The limitations of the experimental work undertaken in this thesis are also discussed.

Chapter 2

Texture Analysis Using First Order Features and Co-Occurrence Matrices

2.1 Overview

In the previous chapter, we discussed the various aspects of medical image processing and studied the nature of a whiplash injury. As described in the problem outline, in this thesis, we investigate application of texture and shape analysis to characterise the nerve damage due to whiplash injuries. In this chapter, we study the application of first order features to the median nerve in the carpal tunnel and the brachial plexus. We also investigate the application of grey-level co-occurrence matrices to the median nerve in the carpal tunnel.

2.2 Introduction to Texture Analysis

Texture can be described as an inherent property of every surface. It contains information about the surface and can be classified as fine, coarse, smooth irregular or periodic [23].

The subject area of texture analysis is about three decades old and has seen significant advances over this time. An exhaustive review on the different texture methods can be found in [24]. The use of texture analysis is purely application dependent and varies from being used for segmentation, classification or for reconstructing three-dimensional surface geometry [24]. In this study, we implement a statistical approach to understanding

the texture of the peripheral nerves and attempt to discriminate between normal subjects and patients suffering from WAD.

The most evident statistical information contained in an image can be found in an image histogram. The histogram contains the first order features of texture which are calculated using single pixels. The parameters that can be extracted from the image histogram are summarised below. A detailed explanation of these first order texture features can be found in [25] [26] [27].

Mean $\mu = \sum_{i=0}^{G=G-11} ip(i)$ **Equation 2.1**

Variance $\sigma^2 = \sum_{i=0}^{G-1} (i-\mu)^2 p(i)$ **Equation 2.2**

Skewness $\mu^3 = \mu^{-3} \sum_{i=0}^{G-1} (i-\mu)^3 p(i)$ **Equation 2.3**

Kurtosis $\mu^4 = \sigma^{-4} \sum_{i=0}^{G-1} (i-\mu)^4 p(i) - 3$ **Equation 2.4**

Energy $E = \sum_{i=0}^{G-1} [p(i)]^2$ **Equation 2.5**

Entropy $H = -\sum_{i=0}^{G-1} p(i) \log_2 [p(i)]$ **Equation 2.6**

Statistical approaches represent texture using the distribution and relationships of grey level values in the image. The most important of the statistical approaches that have found numerous applications across medical image analysis is co-occurrence matrices. Co-occurrence matrices are derived by extracting statistical information from the distribution of pixel-pairs in the image. A co-occurrence matrix can be effectively computed in two ways: directional or rotationally invariant [28]. To construct a rotationally invariant co-occurrence matrix, only pairs of pixels that are at a fixed distance from each other are

considered. Such matrices use only distance as a factor irrespective of the orientation of the line that joins the pixels. This can be expressed in the following equation [28]:

$$C(k,l;d) \equiv \sum_{i}\sum_{j}\sum_{\hat{n}} \delta(k - g(i,j))\delta(l - g((i,j) + d\hat{n}))) \qquad \textbf{Equation 2.7}$$

where $C(k,l;d)$ is the total number of pairs of pixels at distance d from each other such that the first one grey value k and the second has grey value l, $\hat{n}$ is the unit vector in a chosen direction, $g(i,j)$ is the grey value of a pixel (i,j), and $g((i,j) + d\hat{n})$ is the grey value of another pixel at distance d from the pixel (i,j) [28].

To capture the directional information in a co-occurrence matrix, in addition to considering the distance between two pairs of pixels, a reference direction can also be used such that the line that connects the pixel pairs then forms an angle with this reference direction [28]. These co-occurrence matrices have two main parameters of distance, d, and angle, ϕ, with respect to the reference direction. This co-occurrence matrix can be expressed in the equation below [28]

$$C(k,l;d,\phi) = \sum_{i}\sum_{j} \delta(k - g(i,j))\delta(l - g(i + d\cos\phi, j + d\sin\phi)) \qquad \textbf{Equation 2.8}$$

A recent review on the role of texture analysis in neurologic imaging applications defines texture as a multistep process [29]. It attempts to validate a hypothesis that by examining the nature of grey levels in medical images, texture features can be extracted which may help characterise the pathology and help discriminate between normal and diseased tissues [29]. An overview of the steps involved in texture analysis as described in [29] is presented in the figure 2.1 below.

Figure 2.1: Step-wise Process for Texture Analysis [29]

2.3 Applications of Texture Analysis

The applications of texture analysis are numerous and span across non-medical and medical fields. This section discusses some of the significant applications of texture analysis in the study of medical imagery.

In a study by Radulescu *et al.* [30] texture analysis was used to study the prediction that neuro-developmental abnormalities had an impact on the textural homogeneity of the brain tissue [30]. Textural features such as mean grey- level intensity (MGL), entropy and uniformity were extracted from filtered and non- filtered MR images of the brain. Spatial filtering was used to derive fine, medium and coarse textural integrity to study the brain tissue between controls and patients with Asperger syndrome. Results showed higher entropy and lower uniformity in the textures of the patient group [30].

In a similar study by Ganeshan *et al.* [31] texture analysis was applied on non-contrast enhanced computed tomography images of the liver to study the impact of malignancy in tumours on the apparently disease-free areas of the liver. It was observed in this study that texture was not altered on unfiltered images, whereas relative texture analysis following image filtration identified differences in fine to medium texture ratios in apparently disease-free areas of the liver in patients with hepatic metastases as compared to patients with no tumour and patients with extra-hepatic disease [31].

In a study by Orphanidou-Vlachou *et al.* [32] texture analysis was implemented to discriminate between brain tumours in children using T1- and T2- weighted MR images. Textural features were extracted from the image histogram, co-occurrence matrices produced for four directions and five inter-pixel distances, run length matrices, an autoregressive model and Haar wavelets. Feature reduction was done using principal component analysis and classification was performed using probabilistic neural networks and linear discriminant analysis. The results from this study showed that the features that

had the highest discriminating potential were all derived from the co-occurrence matrices and that texture analysis could be reliably used to differentiate brain tumours in children [32]. First order and second order features were also used for classification of Alzheimer's disease based on T2- weighted MR images of the brain in [33]. This study showed that first and second order based statistical features performed significantly better for all classifiers as compared to existing methods based on wavelet transforms [33].

In a study by Li *et al.* [34] age- related differences in the quantitative echo texture of the median nerve were studied using texture analysis. In this paper, the texture of a normalised median nerve was analysed to identify differences in texture between 10 healthy young volunteers and 10 elderly patients undergoing lower limb surgery. The aim of this study was to quantify the texture of the median nerve in a sonogram and to demonstrate the changes in echo intensity of the median nerve which possibly correlate to age related degeneration. Echo intensity and echo texture can be explained as a global measure of brightness of pixels in greyscale and variation in the greyscale values of the pixels in a sonographic image, respectively [34]. The images were normalised and a region of interest was manually segmented. Thresholding was then performed to convert the image to a binary image, during which each pixel above the greyscale value of 128 was marked as white and each below 128 was marked as black. The black area index was defined as the ratio of the black area to the total cross-sectional area of the median nerve. The white area index was defined as the ratio of the white area to the total cross-sectional area of the median nerve. Significant differences were found in the measures of cross sectional area of the nerve, echo intensity, white area index and black area index in elderly subjects as compared to the young subjects [34].

In the next section, we examine the application of texture analysis to MR images of the brachial plexus and the median nerve in the MR images of the carpal tunnel.

2.4 Application of first order features to MR images of the Brachial Plexus

A brief description of the anatomy of the brachial plexus has been given earlier in Section 1.7 of Chapter 1. In this section, we study the application of first order textural features on the MR images of the brachial plexus. The description of the image data used in this work and the MRI protocol used for acquisition has been summarised in Section 1.10 and Section 1.11 of Chapter 1.

2.4.1 Experimentation Method

The first order features derived from the histogram of the image were extracted by an algorithm developed in MATLAB [35]. The features extracted from the image histogram were mean grey-level (MGL), variance, skewness, kurtosis, energy and entropy.

For each subject, the MRI slices with the best visibility of brachial nerves were chosen by the medical expert. Among those slices, multiple images were chosen per subject and brachial nerves were segmented from the slice with the best visibility of that nerve. Segmentation was done manually under the supervision of the clinical expert.

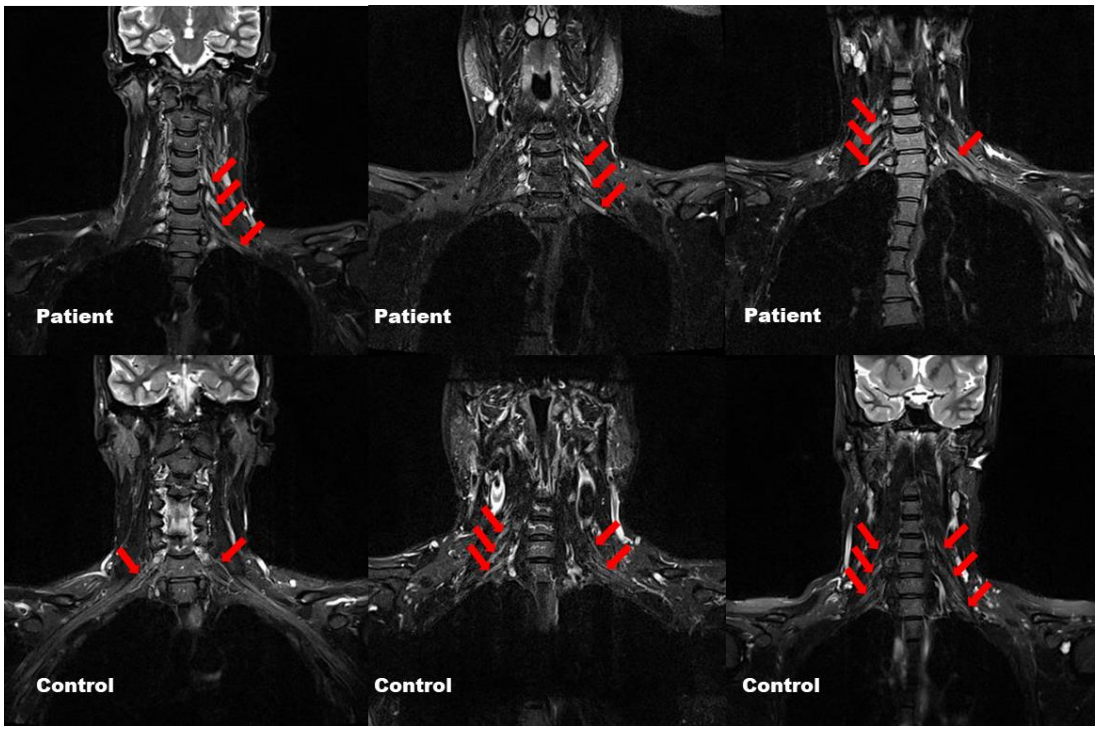

Figure 2.2: T2- weighted STIR image of the roots and trunks of brachial plexus

In Figure 2.2 above, MR images of the brachial plexus for different subjects are presented with the brachial nerves marked with red arrows. It is observed in the Figure 2.2 above that the brachial nerve roots appear brighter in the patients as compared to those in controls. The features were extracted from the brachial nerve roots C5, C6, C7 and C8 on both sides of the subject, the namely right and left side. These are clearly shown in the images below.

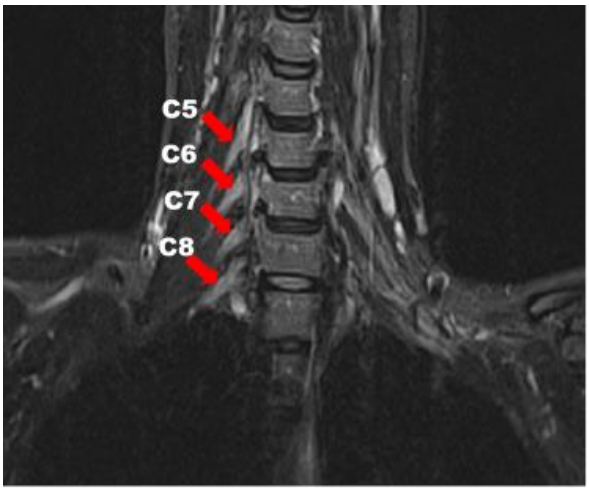

Figure 2.3: Brachial nerve roots on right side of the subject (Coronal view)

The brachial nerves are clearly labelled in figure 2.3 above. In the work described in this thesis, the right-hand side brachial nerves are presented in the results as RC5, RC6, RC7 and RC8 for better comprehension.

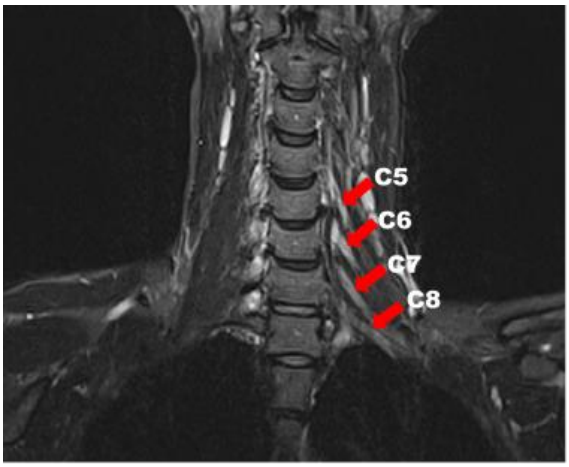

Figure 2.4: Brachial nerve roots on the left side of the subject (Coronal view)

The brachial nerves labelled in figure 2.4 above are the brachial nerve roots on the left side in the subject and are presented in the results as LC5, LC6, LC7 and LC8 for better comprehension.

2.4.2 Results

Table 2.1 below presents the results of the first order features extracted from the brachial nerve roots. The resultant values are the average of each group for the respective brachial nerve roots. The averages for the left and right brachial plexus roots are also calculated for the two groups. The last column in the table displays the average of the left and right side combined for each of the features. The detailed results for each control and each patient are provided in Appendix A [Part 1: Table A.1 to Table A.6].

	Mean Gray Level (MGL)										
	LC5	LC6	LC7	LC8	L-Avg	RC5	RC6	RC7	RC8	R-Avg	L+R
Controls	3.8120	4.5085	4.6341	2.9465	3.9753	3.3451	3.7795	4.1953	4.1271	3.8618	7.8371
Patients	3.2340	4.1229	4.5861	4.3852	4.0821	3.5727	4.1473	4.4659	4.0942	4.0700	8.1521
	Variance in Gray Level (VGL)										
	LC5	LC6	LC7	LC8	L-Avg	RC5	RC6	RC7	RC8	R-Avg	Kurt L+R
Controls	3.5270	3.9123	3.5125	2.6496	3.4003	2.7812	3.1528	3.4021	3.7518	3.2720	6.6723
Patients	3.1558	3.5656	3.1973	3.5525	3.3678	3.1431	3.9739	3.3125	3.5014	3.4828	6.8505
	Skewness										
	LC5	LC6	LC7	LC8	L-Avg	RC5	RC6	RC7	RC8	R-Avg	Skew L+R
Controls	0.6188	0.4203	0.4415	0.4547	0.4838	0.2828	0.5530	0.6231	0.3687	0.4569	0.9407
Patients	0.4193	0.4241	0.2712	0.3669	0.3704	0.6160	0.5477	0.5328	0.5554	0.5630	0.9334
	Kurtosis										
	LC5	LC6	LC7	LC8	L-Avg	RC5	RC6	RC7	RC8	R-Avg	Kurt L+R
Controls	2.6187	2.2964	2.4906	1.9948	2.3501	1.9613	2.8162	2.8901	2.1805	2.4620	4.8121
Patients	1.9125	2.4889	2.4526	2.4902	2.3360	2.7169	2.4499	2.5939	2.6293	2.5975	4.9335
	Energy										
	LC5	LC6	LC7	LC8	L-Avg	RC5	RC6	RC7	RC8	R-Avg	Energy L+R
Controls	0.1746	0.1603	0.1670	0.1103	0.1531	0.2936	0.5017	0.5461	0.4680	0.4524	0.6054
Patients	0.1243	0.1636	0.1675	0.1683	0.1559	0.1582	0.1636	0.1674	0.1813	0.1676	0.3235
	Entropy										
	LC5	LC6	LC7	LC8	L-Avg	RC5	RC6	RC7	RC8	R-Avg	Entropy L+R
Controls	1.9732	1.9644	1.9545	1.1751	1.7668	1.5636	1.7699	1.8984	1.8412	1.7683	3.5350
Patients	1.5353	1.9396	1.9145	1.9200	1.8274	1.5313	1.9639	1.9248	1.9203	1.8351	3.6624

Table 2.1: Results presented as an average of the first order features for controls and patients of the four brachial nerve roots

It can be observed in Table 2.1 above, that the average MGL values for the nerve roots on the left side are higher in patients than the same in the controls. Similarly, the average MGL values for the brachial nerve roots on the right side in patients are higher than the same in controls. This can be attributed to the increase in intensity of the brachial plexus

in patients which could be presenting a possible underlying neuropathy. As seen in Figure 2.2 earlier in this chapter, the brachial nerves appeared brighter in patients as compared to those in controls. The MGL values can be used to describe the intensity of the magnetic resonance signal emitted by the nerves.

2.4.3 Statistical analysis

To test if the first order features were statistically significant, unpaired t-tests were used to compare the mean values between groups. It was found that only MGL was statistically significant ($P<0.05$). The other features demonstrated differences in controls and patients; however, they were not statistically significant. Hence, only the MGL value was chosen as a feature of interest for further study of the nerves.

2.4.4 Normalisation of mean grey-level (MGL) values in the brachial plexus

Due to inherent variations in the receiver gain and variation in the position of the subject between sessions, which may affect overall signal intensity, the MGL values obtained from first order statistics were normalised to the signal intensity emitted by the spinal cord. This normalisation was crucial in removing any bias in results due to the subjects being scanned at separate times and to nullify any changes in intensity due to the interim maintenance of the MRI machine between scans. Therefore, instead of using the raw mean gray level (MGL) values, the signal intensity of the brachial nerves was expressed as a ratio and the results are presented in Table 2.2 below.

	LC5	LC6	LC7	LC8	L-Avg	RC5	RC6	RC7	RC8	R-Avg	L+R
Controls	0.4208	0.4806	0.5130	0.4764	0.4708	0.4325	0.4492	0.4660	0.4294	0.4454	0.4590
Patients	0.5377	0.5734	0.5301	0.4699	0.5233	0.5089	0.5436	0.5251	0.4888	0.5137	0.5179

Table 2.2: Signal intensity ratio of the brachial nerve roots

2.4.5 Statistical analysis of signal intensity ratio in the brachial plexus

There was no significant difference in signal intensity ratio between the left (mean = 0.47 (0.02 SEM)) and right side (mean = 0.45 (0.01 SEM)) in the healthy control group or the least (mean = 0.53 (0.02 SEM)) and most symptomatic side (mean = 0.52 (0.02 SEM)) in the patient group (P>0.64, paired t-test), and therefore data from each side was combined. The detailed results are provided in Appendix A. The mean combined signal intensity ratio was 13.6% greater in the patient group (mean = 0.52 (0.01 SEM)) compared to the healthy control group (mean = 0.46 (0.01 SEM)), a difference that was significant (P<0.05, unpaired t-test, see Figure 2.5 below). An examination of the individual cervical roots of the brachial plexus revealed a 22.6% and 20.0% increase in the signal intensity ratio in the C5 and C6 roots in patients compared to healthy controls (P<0.05, unpaired t-test, see Figure 2.6 below). The data from both the left and right side was combined to demonstrate the intensity ratio in the individual cervical roots and is presented in Figure 2.6 below. The signal intensity ratio of the C7 and C8 cervical roots was not significantly different between groups (P>0.20, unpaired t-test).

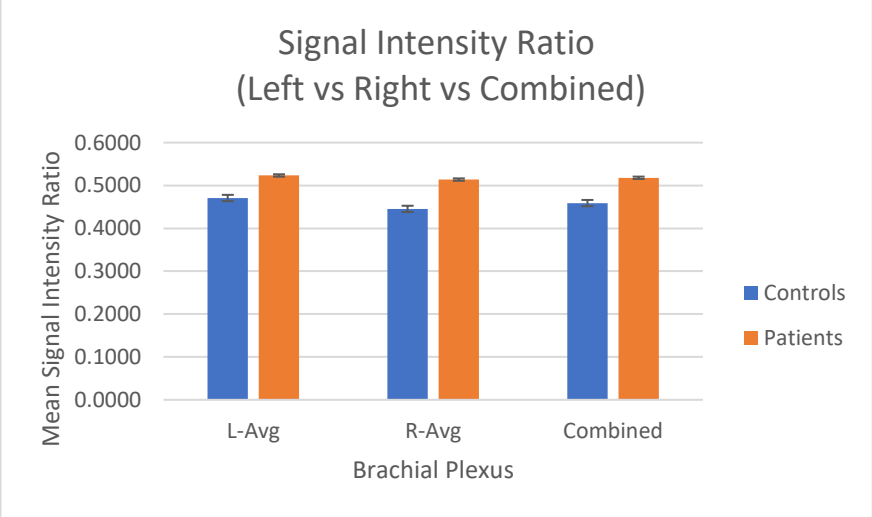

Figure 2.5: Signal intensity ratio for the brachial nerve roots

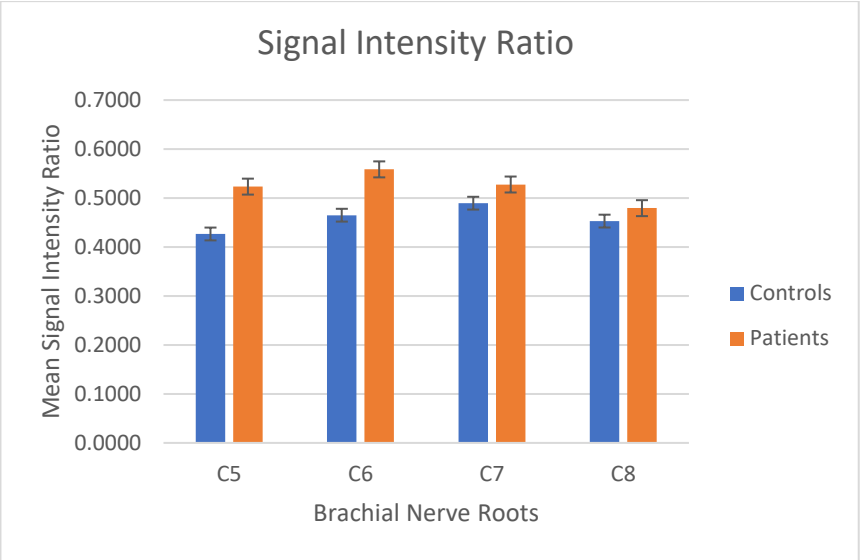

Figure 2.6: Signal intensity ratio for the individual cervical nerve roots

2.5 Application of first order features to median nerve in MR images of the carpal tunnel

A summary anatomy of the carpal tunnel has been given earlier in Section 1.6 of Chapter 1. In this section, we study the application of first order textural features on the MR images of the carpal tunnel with an aim to quantify the signal intensity emitted by the median nerve in the T2- weighted MR images. The description of the image data used in this work and the MRI protocol used for acquisition has been summarised in Section 1.10 and Section 1.11 of Chapter 1.

The first order features were extracted for the median nerve in the carpal tunnel at three locations, namely: the proximal carpal row, the radioulnar joint (RU Joint) and the distal carpal row. These positions in the carpal tunnel were selected based on the clinical assessments done by the clinician prior to image analysis. The figures of the carpal tunnel at these distinct locations are presented below.

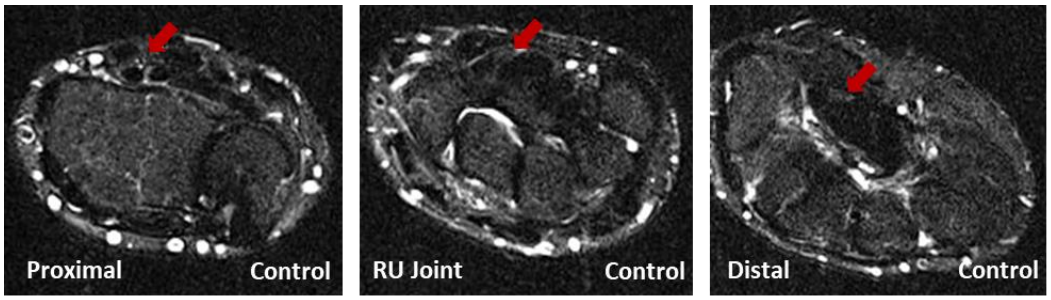

Figure 2.7: Median nerve in the carpal tunnel of a normal subject

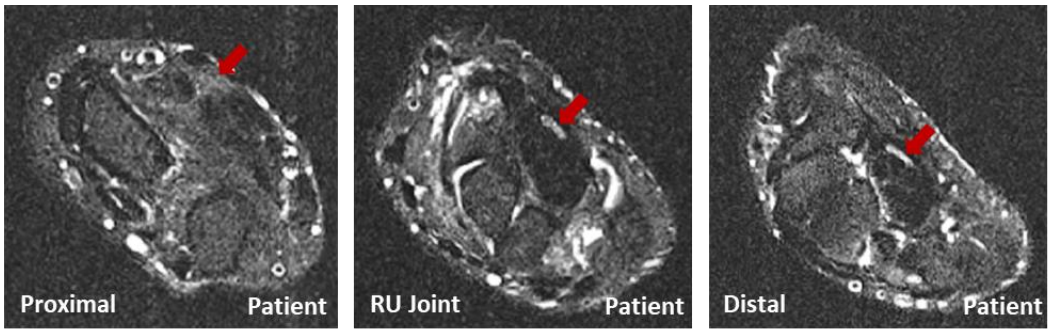

Figure 2.8: Median nerve in the carpal tunnel of a whiplash patient

The features extracted were mean grey level (MGL), variance in grey level (VGL), skewness, kurtosis, energy and entropy. As seen in the case of the brachial plexus in the earlier section, the mean grey level (MGL) was chosen as a significant feature as it correlated to the brightness of the median nerves in the patients. However, in order to avoid variations in signal that are encountered with surface coils and also to remove any biases created due to different acquisition times between subjects, the MGL value was expressed as a signal intensity ratio, which was calculated with respect to the signal intensity of the underlying bone at each location in the carpal row (head of radius, lunate or trapezoid for radioulnar joint location, proximal carpal row and distal carpal row location, respectively). The results for the mean signal intensity ratio calculations are presented in the next section. The detailed account of results for each subject at each location can be found in Appendix A [Part 2: Table A.7 and Table A.8].

2.5.1 Results

	Proximal	RU Joint	Distal	P+R+D
Controls	1.1026	1.3772	0.8126	1.0975
Patients	1.5895	2.0895	1.8734	1.8508

Table 2.3: Mean signal intensity ratio of the median nerve in carpal tunnel

The results presented in Table 2.3 above clearly show the increased signal intensity ratio in patients as compared to that in controls. Also, it can be observed that the signal intensity ratio increases in patients at all the three locations in the carpal tunnel and therefore the combined ratio is also high. This can be seen in Figure 2.9 presented below.

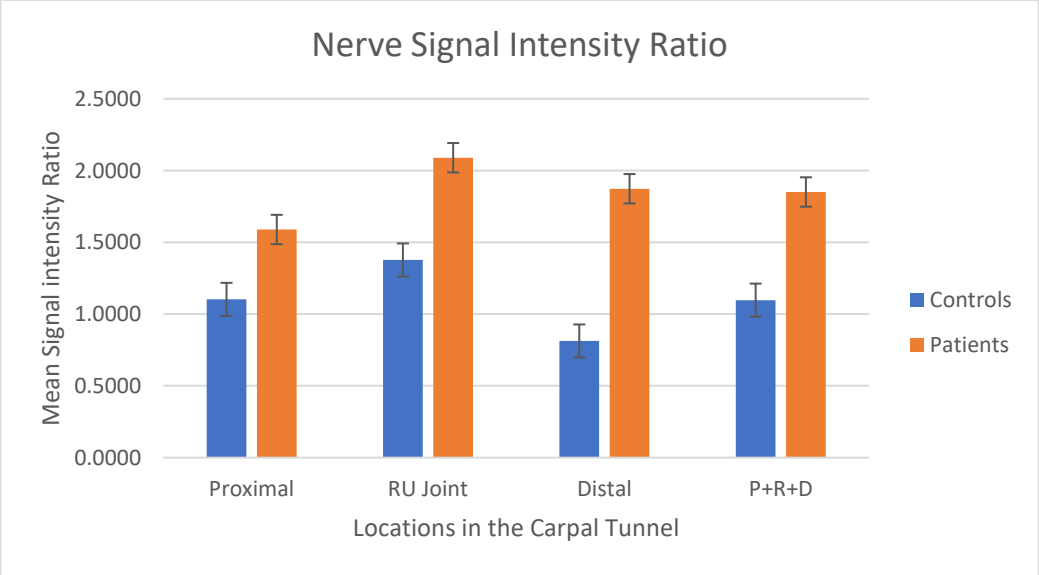

Figure 2.9: Mean signal intensity ratio of the median nerve

2.5.2 Statistical analysis of signal intensity ratio of the median nerve

The median nerve signal intensity data is summarised in Figure 2.3. In the healthy control group, the mean signal intensity ratio was 1.13 (0.06 SEM), 1.38 (0.09 SEM) and 0.81 (0.03 SEM) at the radioulnar joint, proximal and distal carpal row, respectively ($P<0.05$, one-way ANOVA; $P<0.05$ radioulnar joint vs proximal carpal row, proximal vs distal carpal row, radioulnar joint vs distal carpal row, Bonferroni *post-hoc* t-tests). In the patient group, the signal intensity ratio increased by 44.2% (mean ratio = 1.59 (0.05 SEM)), 51.7% (mean ratio = 2.09 (0.12 SEM)) and 130.5% (mean ratio = 1.87 (0.15 SEM)) at the radioulnar joint, proximal and distal carpal row, respectively, with differences that were significant ($P<0.05$ at each location, unpaired t-tests, Figure 2.9).

2.6 Application of GLCM to the median nerve in the carpal tunnel

The grey-level co-occurrence matrices were used to extract textural features of the median nerve in the carpal tunnel. As seen in the earlier section, for each subject three locations in the carpal tunnel were chosen to segment the median nerve, namely: proximal carpal row, radioulnar joint (RU Joint) and the distal carpal row.

The median nerve was manually segmented under the supervision of the clinician. For each median nerve, co-occurrence matrices were calculated for four directions $(\theta = 0°, 45°, 90°, 135°)$ and four inter-pixel distances $d = 1, d = 2, d = 3, d = 4$. Sixteen such matrices were created and each co-occurrence matrix was normalised and the results were extracted from the average of the multiple matrices. An algorithm was developed in MATLAB to extract the textural features as proposed by Haralick *et al*. [23] [35].

2.6.1 Results

The fourteen textures extracted from the co-occurrence matrices for each location in the carpal tunnel presented distinct results that could be used to differentiate between the control and the patient group. The results for the features at the respective three locations are presented in Table 2.4, 2.5 and 2.6 below.

2.6.2 Statistical Analysis

Paired and un-paired t-tests were used to validate the statistical significance of the extracted features. t-tests are used in the work in this study owing to the small sample size.

An unpaired t-test with a two tailed-distribution was done on features extracted from the median nerve at each of the carpal locations. At the proximal carpal row, only the sum entropy measure was statistically significant with a value ($P<0.05$, Table 2.4). The other

features although different in the two groups were not significant enough (P>0.1, Table 2.4). At the distal carpal row, information measures of correlation values were significant (P<0.05, Table 2.5). At the radioulnar joint, none of the features extracted were statistically significant with (P>0.19, Table 2.6).

Paired t-tests were used to study the differences between the various locations in the patient group. The contrast values were higher and statistically significant at the proximal location when compared to the distal and RU joint with a value (P<0.04). The angular second moment was also significant with a p value of (P<0.03).

	Proximal Carpal Row		
	Controls	**Patients**	**t-Test**
Angular Second Moment	2.6024	2.5800	0.97
Contrast	1.3613	1.2429	0.39
Correlation	0.0154	0.0121	0.24
Energy	0.0009	0.0010	0.84
Entropy	0.2835	0.2827	0.89
Maximum Probability	0.0027	0.0026	0.80
Sum of Squares:Variance	3.2825	3.1984	0.88
Sum Average	0.7676	0.7585	0.91
Sum Variance	7.7974	7.7250	0.97
Sum Entropy	0.1841	0.1795	0.03
Difference Variance	1.3632	1.2429	0.38
Difference Entropy	0.1372	0.1353	0.45
Information measures of Correlation	-0.0114	-0.0094	0.10
Maximum Correlation Coefficient	0.0476	0.0442	0.10

Table 2.4: Texture features extracted from GLCM at the proximal carpal row

	Distal Carpal Row		
	Controls	**Patients**	**t-test**
Angular Second Moment	2.9388	2.6605	0.70
Contrast	0.9294	0.9485	0.89
Correlation	0.0095	0.0106	0.74
Energy	0.0016	0.0010	0.17
Entropy	0.2557	0.2767	0.15
Maximum Probability	0.0039	0.0027	0.27
Sum of Squares:Variance	3.4101	3.1317	0.72
Sum Average	0.8087	0.7887	0.85
Sum Variance	8.7972	7.6680	0.63
Sum Entropy	0.1652	0.1746	0.28
Difference Variance	0.9294	0.9485	0.89
Difference Entropy	0.1234	0.1293	0.37
Information measures of Correlation	-0.0127	-0.0095	0.04
Maximum Correlation Coefficient	0.0470	0.0442	0.25

Table 2.5: Mean values for texture features extracted from GLCM at the distal location

	Radioulnar Joint		
	Controls	**Patients**	**t-test**
Angular Second Moment	2.4260	1.7705	0.60
Contrast	1.0858	0.9396	0.49
Correlation	0.0120	0.0128	0.70
Energy	0.0013	0.2706	0.25
Entropy	0.2238	0.2564	0.47
Maximum Probability	3.5382	0.0043	0.32
Sum of Squares:Variance	1.5573	2.2379	0.57
Sum Average	0.4879	0.6183	0.52
Sum Variance	3.4110	5.0896	0.60
Sum Entropy	0.0870	0.1662	0.49
Difference Variance	0.6050	0.9396	0.49
Difference Entropy	0.1459	0.1216	0.36
Information measures of Correlation	1.3129	-0.0088	0.19
Maximum Correlation Coefficient	0.3432	0.0413	0.29

Table 2.6: Mean values for texture features extracted from GLCM at the RU Joint

2.7 Conclusion

In this chapter, we investigated the application of texture analysis to quantify the nerve roots in the brachial plexus and the median nerve in the carpal tunnel. Texture analysis was performed using first and second order features. The results from first order features were analysed and the nerve signal intensity ratio was found to be statistically significant among the two groups. Although co-occurrence matrices are effective instruments for texture analysis, in this case, the results obtained could differentiate between patients and controls but their statistical significance could not be proved. In the following chapters, we test the implementation of run length matrices and autocorrelation functions on characterising the nerves in controls and whiplash patients.

Chapter 3

Texture Analysis using Gray Level Run Length Matrices (RLM) and Autocorrelation

3.1 Run Length Matrices

A gray level run can be described as a set of collinear pixel points that have the same gray level values in an image. The run length matrix consists of the number of times a gray level appeared in runs having any given direction. The texture measures obtained from this run length matrix are computed similarly to functions obtained from co-occurrence matrices used by Haralick [23]. The different run length features were first proposed by Galloway [36]. The traditional RLM features are summarised in Appendix B[Part-1] [37].

3.1.1 Applications

In a paper by Yu *et al.* [38] run length matrices (RLM) have been used in combination with gray level co-occurrence matrices for texture analysis of parametric T1 and T2 maps for the detection of hepatic fibrosis. The RLM features extracted (see Appendix B for definition of these terms) were short run emphasis (SRE), long run emphasis (LRE), gray-level non-uniformity (GLN), run-length non-uniformity (RLN), run percentage (RP), low gray level run emphasis (LGRE), high gray-level run emphasis (HGRE), short run high gray-level emphasis (SRHGE), long run low gray-level emphasis (LRLGE), and long run high gray-level emphasis (LRHGE). The rows contained the gray-levels and the columns represented the run lengths or the consecutive number of pixels with a particular gray level value. In this study, the results showed that the best discriminating texture features were SRHGE, LRLGE and LRHGE in T1 maps. High gray-level run emphasis (HGRE) was the best discriminating feature for T2 maps [38].

In another study by Rezatofighi *et al*. [39], run length features were extracted from polar transformed haematological images for automatic detection of red blood cells. The run length was defined in four directions. Features such as short run emphasis, long run emphasis, gray-level nonuniformity, run nonuniformity and run percentage were extracted to represent different textural properties. These five features were significant in determining intensity variations in the haematological images. Further, a two-layer perceptron with 40 neurons in the hidden layer was used for classification of the feature vectors. The study inferred that run length features used in combination with polar transformed images were successful in classifying different shapes of almost similar sizes even when some objects were overlapping [39].

In a breast tumour study by Afshin and Akbar [40], sonographic texture analysis was done using a run length matrix. The study results demonstrated that RLM texture features could differentiate between benign and malignant breast tumours with high accuracy. RLM features presented good classification accuracy of 98 percent with 96.8 percent sensitivity and 100 percent specificity. The study highlighted that RLM features performed better on ultrasound images and had a stronger potential to characterise benign and malignant tumours than other texture methods such as a GLCM, wavelet, shearlet and curvelet, and auto-covariance matrix [40].

In a study by Gupta *et al*. [41] used run length features to successfully classify gliomas from MR images of the brain using naive Bayes classifiers. The study not only identified brain tumours but also aided in grading the tumours based on their severity. The features used in the study were SRE, LRE, GLN, RLN, RP, LGRE, HGRE, Short run low gray level run emphasis (SRLGE), Short run high gray level emphasis (SRHGE), Long run low gray level emphasis (LRLGE) and Long run high gray level emphasis (LRHGE) [41].

In another such oncology research study, quantitative image features were extracted from tumours in non-small cell lung cancer (NSCLC) by Hunter *et al*. [42], to predict tumour volume shrinkage from pre-treatment CT images. The features extracted to build the quantitative feature model used were texture analysis such as intensity histograms, absolute gradient image, co-occurrence matrix and run length matrix. The feature model was used successfully to predict tumour shrinkage which is an indicator of treatment efficacy and future survival [42].

A study by Cai *et al*. [43], a novel method for identification of osteoporosis using a co-occurrence matrix and a run length matrix was investigated. Twenty female rates aged 3 months were used as experimental subjects in this study. They were divided into two

groups SHAM and OVX. The SHAM rats are the group of female rats that have faked (placebo) surgical intervention performed whereas OVX rats are the female rats in which ovariectomy (removal of ovaries) was performed. Texture analysis was performed on the photographed image of the thick bone tissue magnified under a microscope. The results showed significant differences in the run length features used for classification. The extracted texture features highlighted the microscopic pathological changes in the bone density that were invisible to the naked eye [43].

3.1.2 Experimentation Method

In this chapter, run length matrices was used to extract textural features of the median nerve in the carpal tunnel of patients who had a history of a whiplash injury and had pain symptoms in the hand and shoulder with no clinical representation.

The median nerve was manually segmented from the MR images of each subject. The region of interest that consisted of the median nerve was then used to extract the RLM features using an algorithm written in MATLAB [44] .

For each subject, the median nerve was segmented at three positions within the carpal tunnel, namely: proximal, radioulnar joint and distal. The RLM features were extracted for each subject at the above three locations. The run length matrix was defined by specifying four directions: 0º, 45º, 90º and 135º and then counting the occurrence of runs for each gray level and length of each run in each direction. The results obtained from all directions were added to form the resultant run length matrix and the features were extracted from them.

The run length features were also extracted from the nerve roots in the brachial plexus in the control and patient group. The nerve segments of the brachial plexus were manually segmented using labelled images provided by the medical expert. For each subject, eight

nerve segments were segmented from the brachial plexus on both the right and the left side. The nerve segments extracted belonged to C5, C6, C7 and C8 nerve roots for both right side and left side. The nerve roots were labelled as LC5, LC6, LC7 and LC8 for the left side and RC5, RC6, RC7 and RC8 for the right side. The RLM features extracted were SRE, LRE, GLN, RP, RLN, LGRE and HGRE like those extracted for the median nerve in the carpal tunnel. The detailed overview of the results is placed in the Appendix B [Part-2: Table B.1 to Table B.6].

3.1.3 Analysis of the Median Nerve in Carpal Tunnel

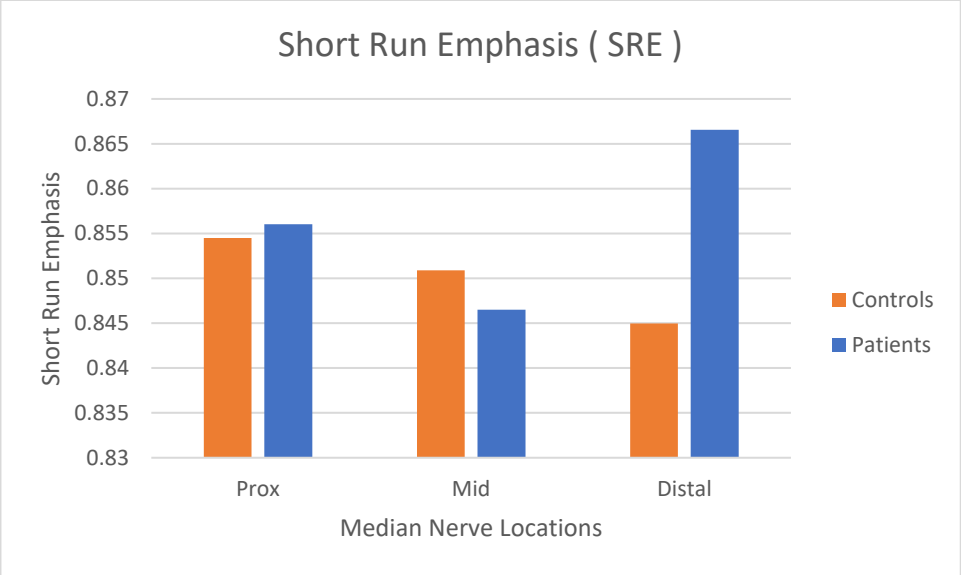

Figure 3.1: The figure shows the SRE values for the controls and the patients at the three distinct locations inside the carpal tunnel namely: the proximal, middle and distal positions.

As can be observed in the above figure, the SRE values for patients is similar but slightly higher than controls in the proximal location. The SRE value is much higher in patients at the distal location in the carpal tunnel. In the middle location, however, the SRE value is lower than the controls. The values plotted above are the average values across the control and patient group, respectively. Therefore, it can be determined that the distribution of short runs is higher in patients at distal locations, suggesting a finer texture of the median nerve owing to the flattening or compression of the nerve.

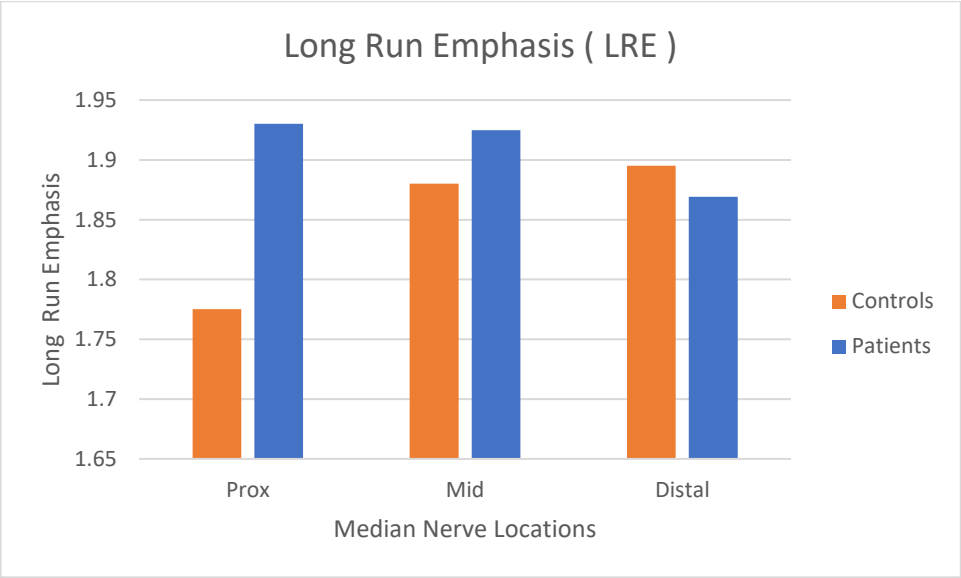

Figure 3.2: The figure shows the LRE values for the controls and the patients at the three distinct locations inside the carpal tunnel, namely: proximal carpal row, radioulnar joint and distal carpal row.

As can be observed in the above figure, the LRE values for patients is considerably higher in patients at the proximal location. This suggests that the texture of median nerve is coarse at this location owing to the enlargement of the median nerve in the proximal location that has been observed in the shape analysis chapter. The LRE value is slightly higher in patients at the middle location as compared to controls and therefore indicates that texture of the nerve is similar in coarseness at this location. However, we observed that the LRE value at the distal location is less than controls, therefore suggesting that the coarseness is reduced due to nerve flattening and supports the higher SRE value seen in the figure 3.2.

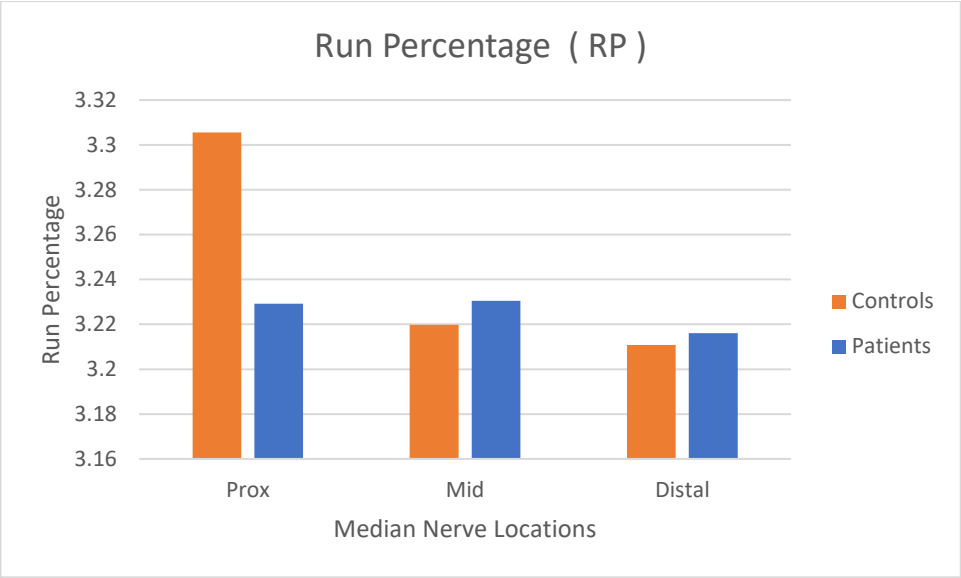

Figure 3.3: The figure shows the RP values for the controls and the patients at the three distinct locations inside the carpal tunnel, namely: proximal, middle and distal positions.

The results of the run percentage (RP) measure the homogeneity in all the runs across the image are shown in the figure above. We observe that at both mid and distal positions, the run percentage in patients is slightly higher than in controls, signifying a not very distinct change in the number of runs between the two groups. This does suggest that the RP value in patients is higher because there is higher variation in the gray values across the median nerve. However, when we look at the RP values of the median nerve in the proximal location inside the carpal tunnel, controls have a significantly higher number of runs than patients at the same location. This may be suggestive of the fact that the length of runs is almost the same for all gray levels in the image.

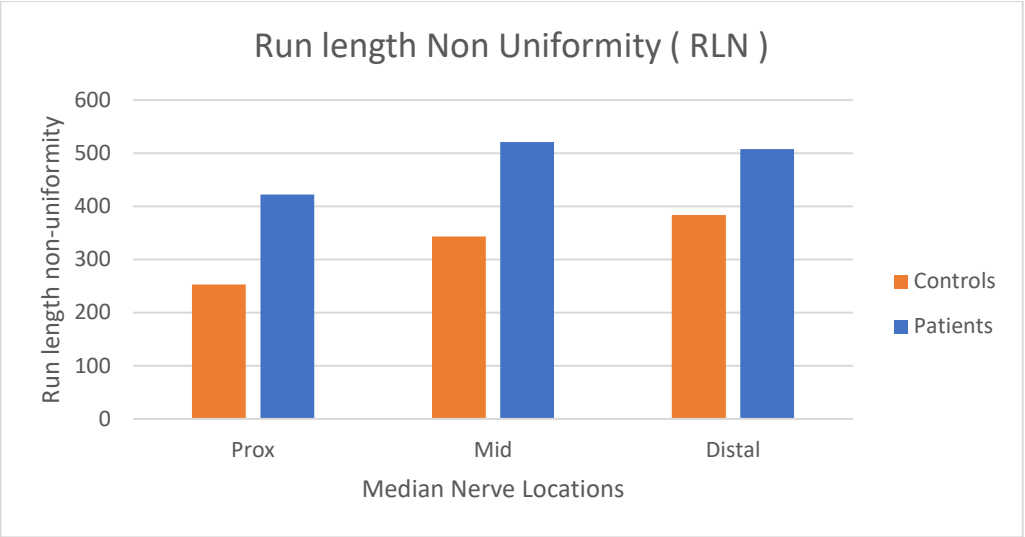

Figure 3.4: The figure shows the RLN values for the controls and the patients at the three distinct locations inside the carpal tunnel, namely: proximal, middle and distal positions.

Run length non-uniformity (RLN) results show that at all the three locations in the carpal tunnel, patients have higher RLN values than controls ($P < 0.05$). This suggests that the number of run lengths in the patient nerves are not alike and differs due to varying gray levels in the image.

In controls, on the contrary, the number of the run lengths are lower, suggesting that there is similarity in the length of runs throughout the image due to less intensity variation and a more constant number of gray levels.

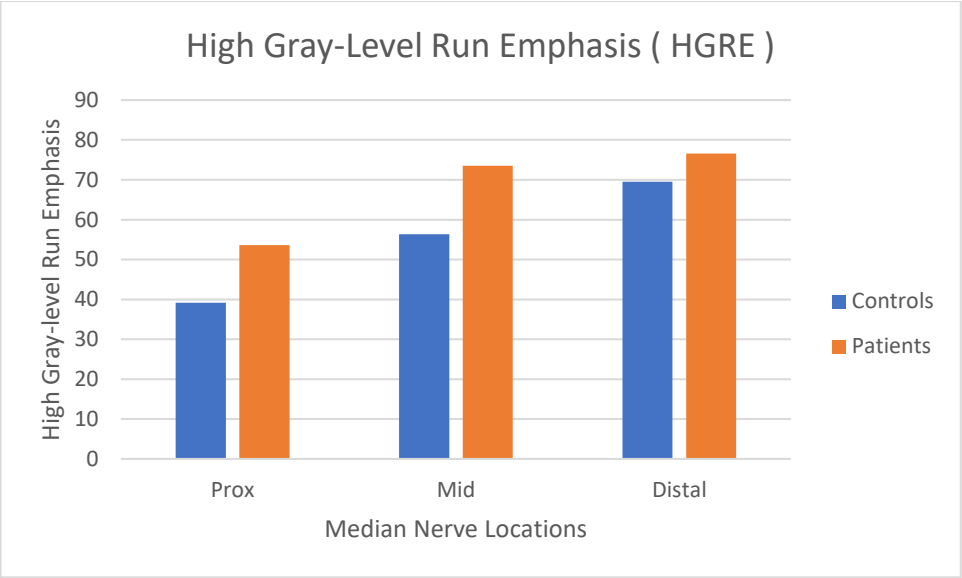

Figure 3.5: The figure shows the HGRE values for the controls and the patients at the three distinct locations inside the carpal tunnel, namely: proximal, middle and distal position.

The results for high gray-level run emphasis measure the distribution of high gray level values. It can be observed that the median nerves of the patients at all three locations have a higher HGRE value than their corresponding controls in that location. The median nerves of the patients are visibly brighter suggesting a possible inflammation, and this is clearly indicated by high HGRE values. HGRE values are like GLN values which measure the non-uniformity between gray levels across the median nerve in patients and controls. GLN values are lower if the gray level values are alike through the image. GLN values for patients were significantly higher than controls in all the three locations, therefore indicating the higher intensity variations in patient nerves as observed on MRI and helping to quantify this.

3.1.4 Statistical Analysis

Statistical analysis was performed on all features extracted from the RLM matrix. Un-paired t-tests were used to compare the mean RLM features between controls and patients. The statistically noteworthy features with $P < 0.05$ were the GLN values at proximal location ($P = 0.008537$), RLN values at proximal ($P = 0.0000$), radioulnar joint ($P = 000912$) and distal ($P=0.0317$) locations and HGRE values at the proximal ($P = 0.007601$) location.

3.1.5 Results in the Brachial Plexus

In the case of the brachial plexus, the RLM features were investigated for each of the nerve roots in the brachial plexus on both sides of the subject. A total of ten values were extracted for the five roots on each side of the brachial plexus. In addition to this, the mean values across all the nerve roots were calculated for each left and right side, respectively, for each feature. The detailed results are provided in Appendix B [Part 3-Table B.7].

3.1.6 Analysis of the Brachial Plexus results

The RLM features extracted from the brachial nerve segments are presented by averaging the values of the nerve roots for the left side and the right side and both combined. As it could not be ascertained whether only the dominant side of the subject was affected by whiplash, the results below are presented as an average of the sets of nerves on the left-hand side of the subject, the right hand side of the subject and the left and right side values combined. This is done for both the control and the patient group. The mean values are presented for each of the extracted features and discussed below.

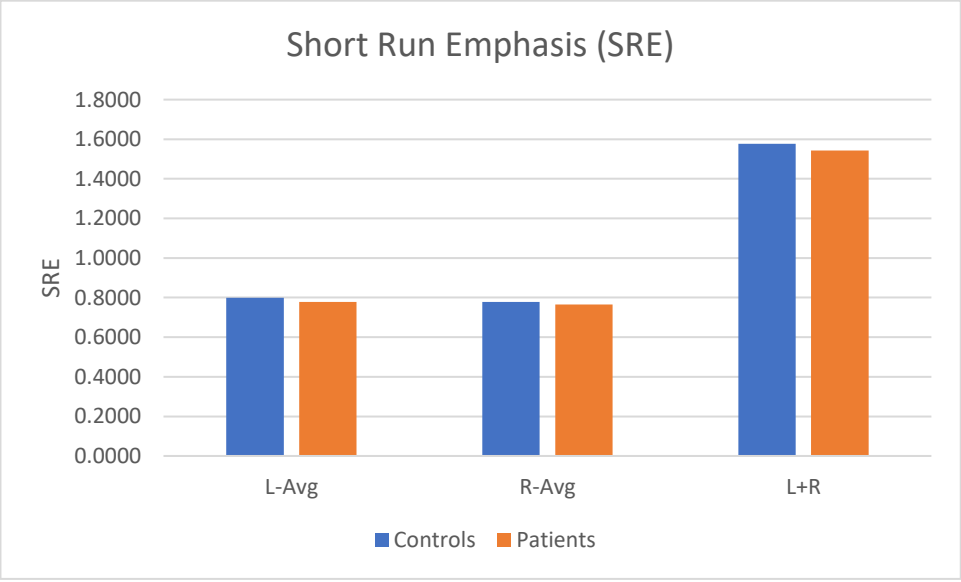

Figure 3.6: Mean Short Run Emphasis (SRE) values for nerve segments of the brachial plexus on the left side, right side and both sides combined, for controls and patients.

As can be observed in figure 3.6, the SRE values on both the left and right side of both the groups are similar. The values are plotted above are the average values of C5, C6, C7 and C8 on both sides. Therefore, it can be seen that the distribution of short runs is slightly less in patients as compared to that in controls but is not a significant feature.

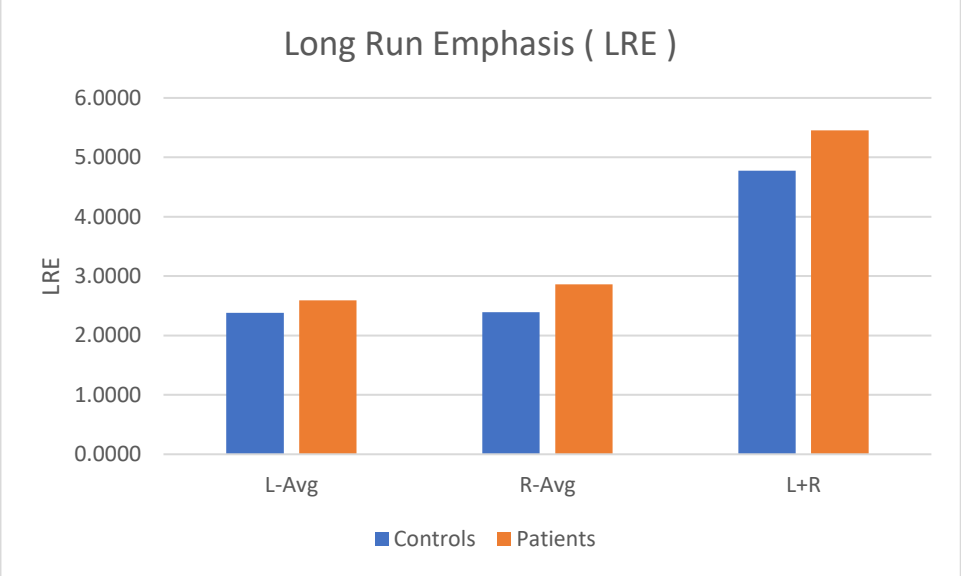

Figure 3.7: Mean Long Run Emphasis (LRE) values for nerve segments of the brachial plexus on the left side, right side and both sides combined, for controls and patients.

As can be observed in figure 3.7, the mean LRE values for the left side and the right side are higher in patients than that in the controls. The mean LRE values for both sides combined are also significantly higher in the patient group than that in the control group. The statistical analysis of this result is presented in the next section in this chapter.

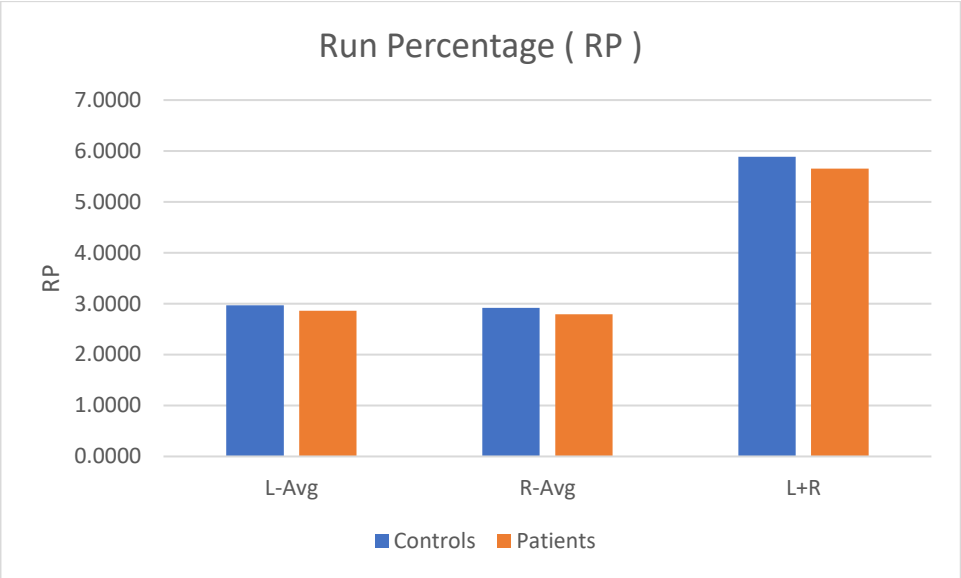

Figure 3.8: Mean Run Percentage (RP) values for nerve segments of the brachial plexus on the left side, right side and both sides combined, for controls and patients.

The mean RP values of the brachial plexus are lower than those of the control group on both left and right sides of the patient group and for the left and right side combined, as shown in figure 3.8 above. Run percentage is simply the ratio of the number of runs to the number of pixels in the region of interest and does not consider the changes in the gray level values. These values may be attributed to the overall size of the nerves in both the control and patient groups.

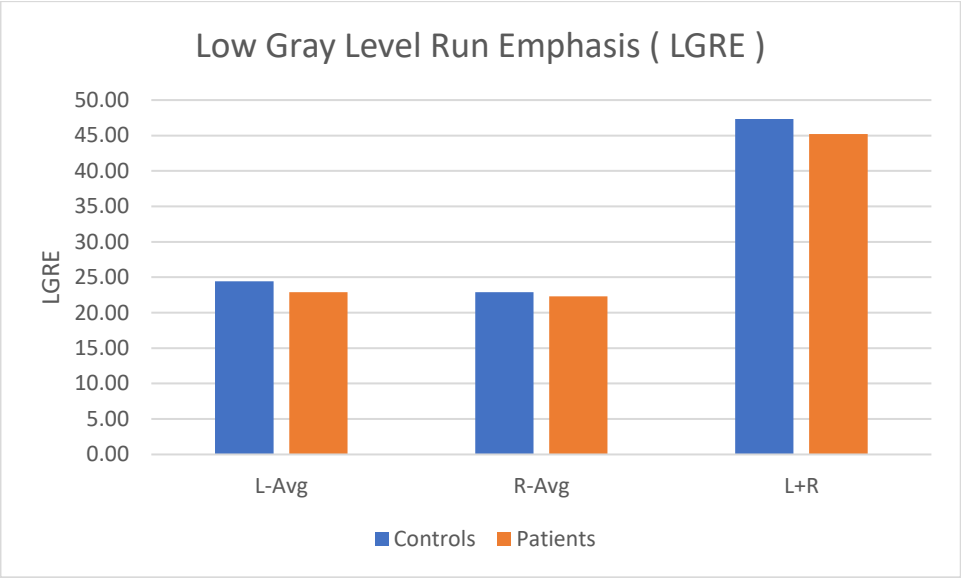

Figure 3.9: Mean low gray level values (LGRE) values for nerve segments of the brachial plexus on the left side, right side and both sides combined, for controls and patients.

This measure is attributed to the number of gray level runs for the low gray level values in the image. In this case, [Refer Appendix, Table A.20], shows that the runs of low gray level values are higher in controls than those in patients. This can be explained as the nerve segments in controls having lower gray level values than those in patients which are brighter i.e. have higher gray level values. This is verified by the HGRE values between the two groups shown in figure 3.10 below.

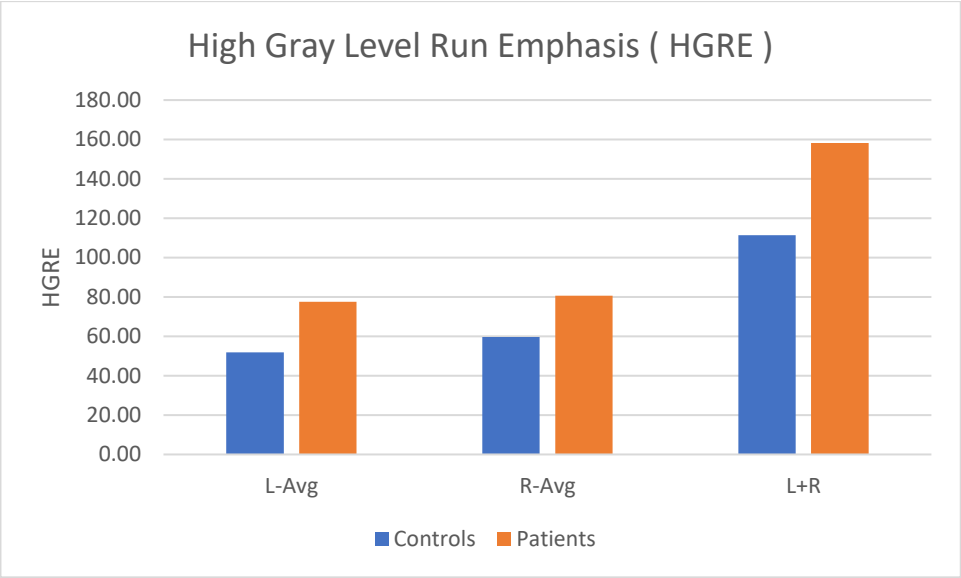

Figure 3.10: Mean high gray level values (HGRE) values for nerve segments of the brachial plexus on the left side, right side and both sides combined, for controls and patients.

Unlike the LGRE values discussed above, mean HGRE values demonstrate that the number of runs of high gray level values are significantly higher in patients than those in controls. This can correlate to the brightness of the nerve segments in patients. It is observed in the MR images of the brachial plexus that the nerve segments in the patients showed higher intensity and so appeared brighter than the nerve segments in controls. As these patients were suffering from whiplash associated disorder (WAD) but had no clinical manifestation in nerve conduction studies, these measures could possibly be used to help improve the diagnosis of WAD in patients.

3.1.7 Statistical Analysis

Unpaired t-tests were performed on all the RLM features extracted and discussed in the previous sections. Although the features differentiated between the nerve segments in patients from those in controls, only a few measures were statistically significant, which are reported below. The LRE measure was considered as statistically significant in all three groups, namely: left average, right average and L+R combined ($P<0.04$, $P<004$, $P<0.0015$), respectively. The GLN measures were the most significant in L+R combined ($P<0.0004$) and in left and right side ($P<0.0011$, $P<0.0032$), respectively. The HGRE measure was the most statistically significant in all three groups, namely: left, right and L+R combined ($P<0.0058$, $P<0.0005$ and $P<0.0165$), respectively.

3.1.8 Conclusion

Texture analysis has been extensively used in both medical and non-medical fields for characterising objects based on their surface texture. In this chapter, we used second order features extracted using gray level run length matrices. The features such as SRE, LRE, GLN, RP, RLN, LGRE and HGRE were extracted from the median nerve in the carpal tunnel and the nerve segments in the brachial plexus to characterise the textural differences between the control group and the patient group. The results demonstrated that some of the RLM measures could differentiate between controls and patients with a statistically significant value of $P<0.05$. Hence, it can be inferred that these measures could be used to study the texture of the nerves in patients suffering from WAD. These preliminary findings need to be established on a larger dataset. However, this study provided an opportunity to use image texture analysis and investigate their possible application to improve diagnosis and thereby improve patient care in the treatment of whiplash injuries.

3.2 The Autocorrelation Function

In the previous section 3.1, texture measures were extracted from run lengths by scanning the image line by line. The length of each gray level run was noted and features were extracted from them. An extension of the above process to two dimensions can be used to study the spatial frequency of the gray values using the autocorrelation function of the image [45].

The autocorrelation function is calculated by correlating an image with itself. As correlation in the spatial domain can be expressed as multiplication in the spatial frequency domain, the autocorrelation function of an image can be determined by the multiplication of the Fourier transform of the image with its complex conjugate. In this section, the autocorrelation function was obtained using an m-file in MATLAB [44].

A paper by Van Gool *et al.*[46] explained autocorrelation as method to study directionality in patterns. It pointed out that the autocorrelation function and the power spectrum are the transforms of each other [46]. Also, another study by Unser *et al.* [47] investigated the use of autocorrelation features for automated inspection of textured materials. A study by Wood [48] used autocorrelation of sub-images of textile fabrics to identify defects in the texture of textiles.

3.2.1 Experimentation Method

In this section, the autocorrelation function for each image was computed using the m-file in MATLAB [44]. The texture signatures in the x and y direction of the image were plotted and features were extracted from the valleys and peaks plotted in the texture signatures. The full width at half maximum height of the peak was calculated for each texture signature in both dimensions of the image. The local maxima of each peak were calculated using the ‘findpeaks’ function in MATLAB. The prominence of the peak was

calculated. The prominence of a peak measures how much the peak stands out due to its intrinsic height and its location relative to the other peaks [44].

The autocorrelation function of the median nerve in the distal carpal row in the carpal tunnel was computed for each control and patient. The autocorrelation plots for all the subjects are provided in the Appendix.

3.2.2 Analysis of results

The figure 3.11 below shows the surface view of the autocorrelation function. It can be observed that the patient nerve has a more prominent peak as compared to a flatter peak of the control nerve shown in figure 3.14 below. The patient nerve was observed to be more compressed and flatter and this can be attributed to the higher peak height. The brightness of the median nerve in patients was also higher than controls and this can be seen in the higher results of peak intensity values and prominence.

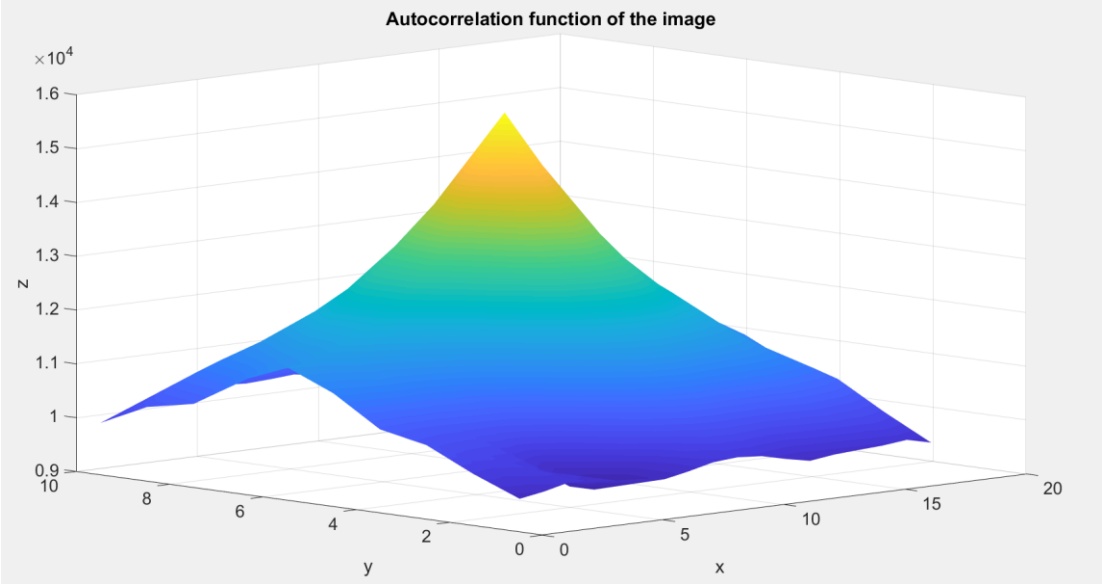

Figure 3.11: Autocorrelation function of a patient nerve

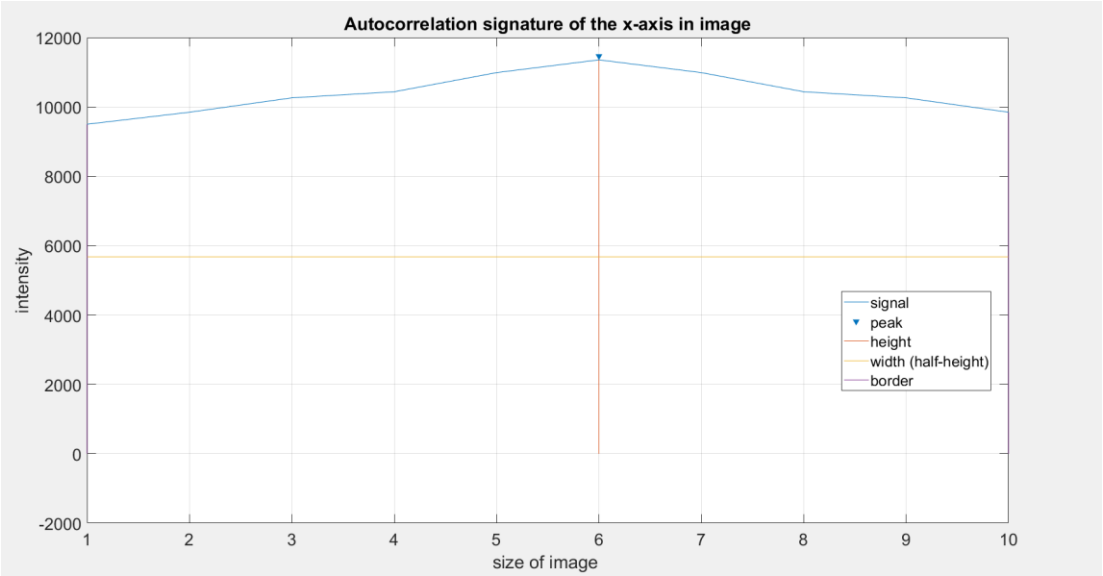

Figure 3.12: Texture Signature of the median nerve in the x-direction (patient)

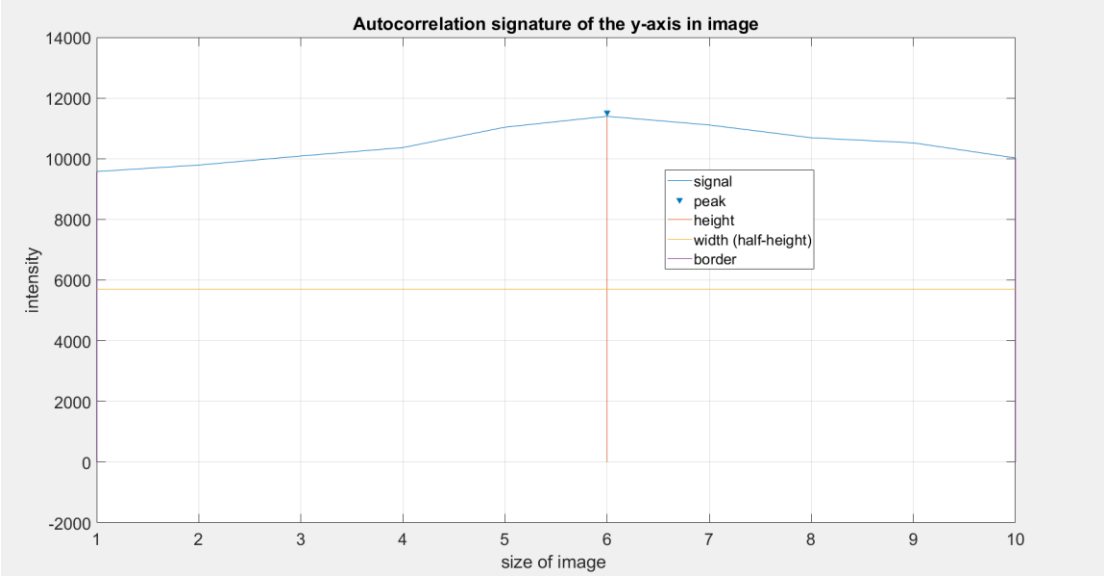

Figure 3.13: Texture Signature of the median nerve in the y-direction (patient)

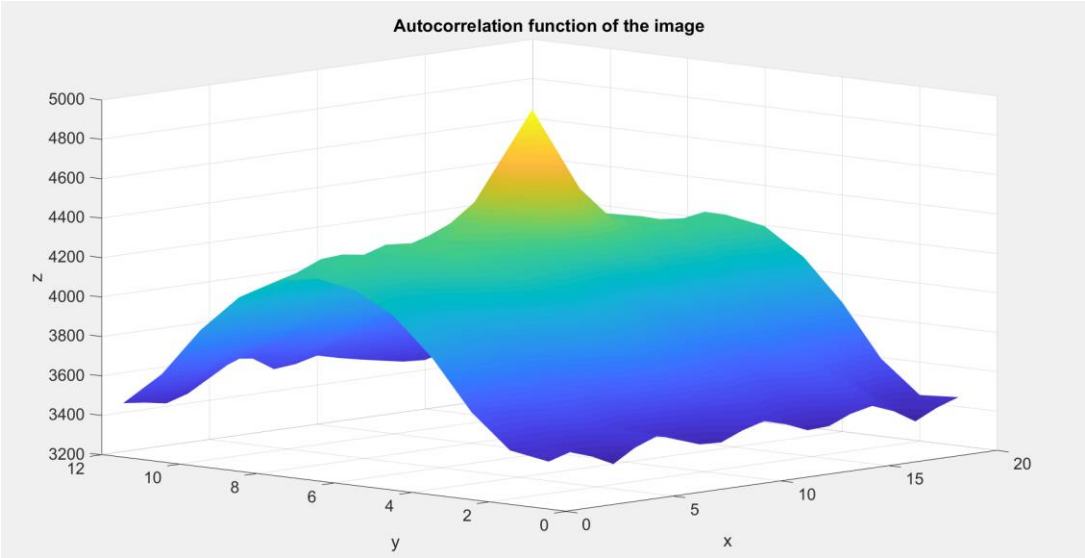

Figure 3.14: Autocorrelation function of a control nerve

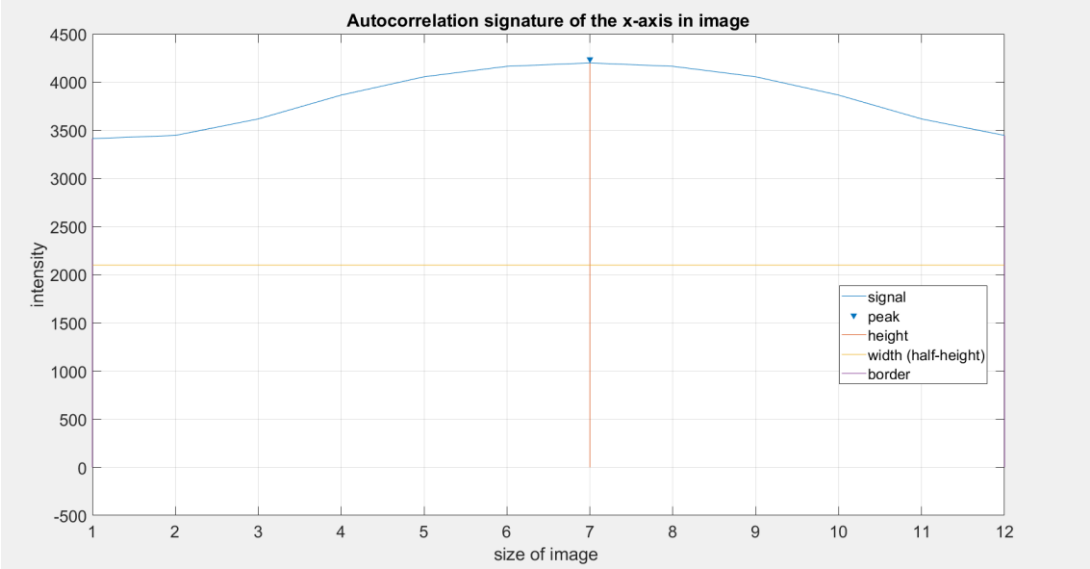

Figure 3.15: Texture Signature of the median nerve in the x-direction (control)

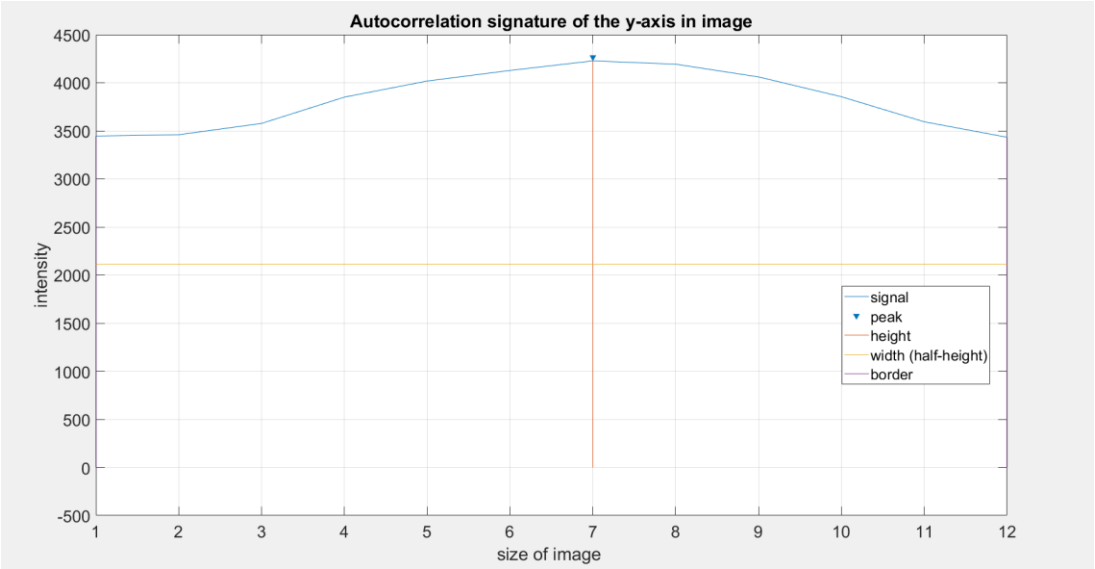

Figure 3.16: Texture Signature of the median nerve in the y-direction (control)

The results for three controls and patients are presented below. For detailed autocorrelation plots for each control and patient, please refer to Appendix C.

Subject	x-direction			y-direction		
	Peaks	Widths	Prominence	Peaks	Widths	Prominence
Patient	10411	1.5535	450.4334	10764	2.4928	1140.2
Patient	11356	3.4016	1509.5	11399	3.4363	1373.3
Patient	18829	2.6182	981.551	19687	1.6088	1421.4
Control	5270.9	5.6641	868.2338	5390.3	5.5244	1035.8
Control	6055.9	5.1275	655.4615	6226.4	4.7205	899.2
Control	4199.1	6.3409	752.875	4227.7	6.1188	781.4

Table 3.1: Autocorrelation peak features of median nerve in controls and patients

It can be seen in Table 3.1 above; the average peak values are higher in patients than controls and this can be attributed to the increased brightness that is observed on the MRI signal. Also, the peak widths are higher in controls as the peaks are flatter in controls as compared to those in patients. The prominence values which show the distinctness of the peak also are higher in patients as compared to those in controls as the flatter and compressed nerves have higher peak heights and therefore higher prominence values.

3.3 Conclusion

This chapter investigated the application of run length matrices and autocorrelation for characterisation of nerves in patients and controls. Run length features were successful in differentiating between normal and patient nerves using unpaired t-tests with features such as LRE, GLN and HGRE having values $P<0.05$. The application of the autocorrelation function was useful in characterising the increased intensity of pixel values in patient nerves and could be used in a larger study as a measure of brightness.

Chapter 4

Application of spatial domain shape metrics to quantify median nerve deformation

4.1 Overview

In the previous chapter, we investigated how texture measures can be used to characterise the median nerve in normal subjects and patients suffering from whiplash associated disorders. Although texture measures show consistent differences between controls and patients, only a few of the measures were statistically significant in characterising the nerve. While doing texture analysis, we observed the morphological changes of the median nerve. Therefore, shape analysis was used to investigate these changes in the shape of the median nerve in the carpal tunnel of the patients. In this chapter, we attempt to quantify the morphology of the median nerve using spatial domain shape metrics.

4.2 Introduction

Texture analysis and shape analysis are interrelated. However, shape analysis is primarily done on a binary image where pixels are either 0's or 1's such that all the pixels that belong to the feature being measured are 1's and the background consists of 0's [49]. Innumerable shape representation and description techniques exist. The choice of the technique would be application dependent. In a review by Zhang *et al.* [50] they summarise the widely-used shape analysis methods. In this review, a shape representation technique can be considered good if it is tolerant of noise, distortion, scale changes, affine transformations, rotations and translational changes. These changes are tolerated by human visual perception almost instantly as we observe shapes. For example, sometimes we can assume shapes in cloud formations although there may be no clear context to do so. Such a tolerant recognition determines the robustness of the shape descriptor [50]. Shape analysis in terms of representing or describing an image can be broadly classified into two categories, namely: contour based methods and region based methods. Contour based methods extract the shape features from the boundary information alone. Contour shape techniques can be further classified as a global approach or structural approach. Continuous approaches or global approaches generally derive all the features from the integral boundary used to describe the shape [50]. Structural approaches or discrete approaches generally divide the boundary of the shape into segments using a set criterion; in this case the shape is represented as a string or a graph. The following chart describes the different shape analysis techniques [50].

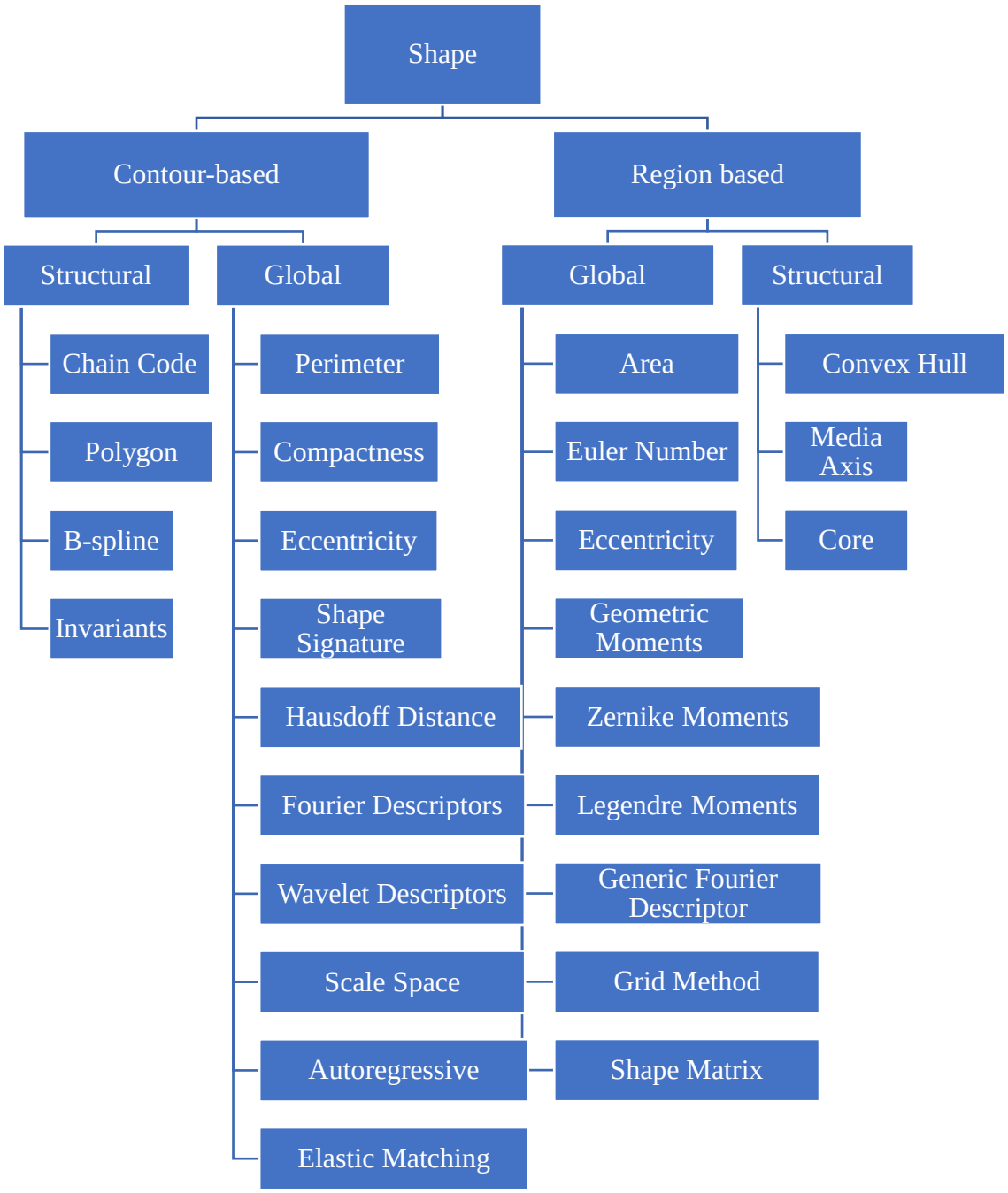

Figure 4.1: Shape representation and description techniques [50]

The median nerve in the carpal tunnel has been extensively studied for the investigation of carpal tunnel syndrome (CTS). Carpal tunnel syndrome is a compression neuropathy of the median nerve at the wrist. The diagnostic procedure for CTS is almost always clinical and is confirmed by nerve conduction studies. A study by Yoshii *et al*. [51] in 2013 investigated the correlation between deformation and displacement of the median nerve and the surrounding tendons during finger motion using images acquired by ultrasound. In this study, the median nerve deformation was studied using deformation indices such as area, perimeter, aspect ratio and circularity. The average of the five parameters was calculated for healthy subjects and patients suffering from carpal tunnel syndrome. The median nerve displacement was defined as the distance of the centroid coordinates between the finger extension and flexion positions. The displacements in the ulnar and radial directions were defined as positive and negative, respectively and in the palmar and dorsal directions were defined as positive and negative, respectively. The study found statistically significant differences in the deformation indices of perimeter, aspect ratio and circularity. The perimeter and circularity deformation indices showed positive correlations with the palmar-dorsal displacement. The deformation indices of area and aspect ratio showed negative correlations with the palmar-dorsal displacements and this was potentially due to nerve enlargement which restricted movement of the nerve in the palmar direction due to non-availability of space within the tunnel [51]. The study described in this chapter implemented the above deformation indices to quantify the median nerve in patients suffering from whiplash associated disorders.

A similar study was done by Wang *et al.* [52] in 2014 which investigated the median nerve deformation and transverse displacement during six different hand and wrist movements in patients with carpal tunnel syndrome. Dynamic ultrasound images were obtained in six positions and image analysis was performed to analyse deformation and

displacement of the nerve. The results showed there were significant differences between the deformation ratios of area, perimeter and circularity of the median nerve. The deformation ratio of the median nerve perimeter was significantly high in CTS patients as compared to that in normal subjects ($P<0.009$). The deformation ratio of circularity in CTS patients was significantly less than that in normal subjects for wrist flexion with fingers extended, wrist flexion with fingers flexed and wrist ulnar deviation with fingers extended ($P=0.009$, $P=0.004$ and $P<0.001$, respectively) [52].

A study by Filius *et al.* [53] in 2015 investigated the changes in shape and displacement of the median nerve and tendons in carpal tunnel syndrome using multidimensional ultrasound imaging of the wrist. The parameters used to study the deformation of the nerve were area, perimeter, circularity, area deformation ratio, perimeter deformation ratio, circularity deformation ratio and centre of mass. The deformation ratio was defined as the value in the final position divided by the value of the initial position. Transverse endpoint displacement of the nerve and tendons were based on centre of mass calculations. The main findings of this study were increased area of the median nerve in patients with carpal tunnel syndrome and these changes increased with an increase in the severity of CTS in patients. Altered cross sectional area of the median nerve was the best discriminator between controls and CTS patients. This study demonstrated that other parameters such as circularity ratio change in CTS patients could help increase the accuracy of ultrasound imaging [53].

In 2010, a study by Bhooshan *et al.* [54] investigated computerised characterisation of image based prognostic markers to differentiate between invasive and non-invasive breast lesions and metastatic versus non-metastatic breast lesions in dynamic contrast enhanced MR images. The study demonstrated that computer extracted kinetic and morphologic features of lesions had the potential to facilitate characterisation and differentiation of

lesions. The shape features used were size of the lesion, circularity, irregularity of the lesion surface, margin sharpness, variance in margin sharpness and variance in radial gradient histogram. The results showed that circularity could be used as an effective feature for classifying ductal carcinoma *in situ* (DCIS) and invasive ductal carcinoma (IDC) [54].

A study by Agner *et al.* [55] in 2011 defined a novel DCE-MRI descriptor called textural kinetics that attempted to capture spatiotemporal changes in breast lesion texture in order to distinguish malignant from benign lesions. The study qualitatively and quantitatively demonstrated that textural kinetic features outperformed signal intensity kinetics and lesion morphology features in distinguishing benign from malignant lesions. It demonstrated that when texture features were used in combination with shape features, the pairing resulted in an improved diagnostic of breast cancer lesions on DCE-MRI [55].

4.3 Shape descriptors

To study the shape of the median nerve, three locations in the carpal tunnel were selected for study by the clinician. For each subject, the median nerve was manually segmented from the MR image of the carpal tunnel using an image clearly labelled by the medical expert. The three locations used within the carpal tunnel were the proximal carpal row, the radioulnar joint and the distal carpal row. The algorithm to analyse the 16-bit DICOM images was written in MATLAB [56]. The shape metrics calculated were the area of the nerve region, the perimeter, the length of the major axis and the length of the minor axis. From these simple global descriptors, measures of eccentricity, circularity, aspect ratio, area and perimeter were calculated.

Circularity referred to how much the shape resembled a circle and therefore a value of 1 would signify a perfect circle. It can be calculated using the formula [51]:

$$\boldsymbol{Circularity} = \frac{\boldsymbol{Perimeter^2}}{\boldsymbol{4\pi\ Area}} \qquad \textbf{Equation 4.1}$$

Aspect Ratio can be expressed as the ratio of the major axis to the minor axis of the shape [51]:

$$\boldsymbol{Aspect\ Ratio} = \frac{\boldsymbol{Minor\ Axis\ Length}}{\boldsymbol{Major\ Axis\ Length}} \qquad \textbf{Equation 4.2}$$

Eccentricity can be expressed as a flattening ratio and is said to be 1 for a line segment and 0 for a circle. It is expressed as ratio of the distance between the foci of the ellipse and its major axis length.

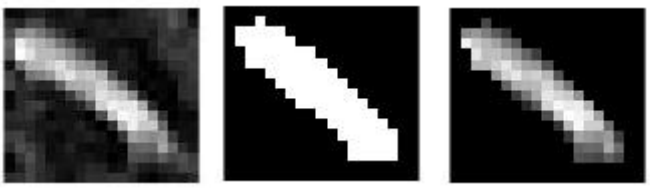

Figure 4.2(a) The median nerve is displayed in this figure with (b) the binary mask and (c) the masked image of the nerve

4.4 Summary of results

The results for the shape measures are summarised in the Table 4.1 below. The area measure for controls and patients is expressed in pixels and then in mm^2 . The conversion from pixels to mm^2 was done using the acquisition parameters set for the MRI scanner: Acquisition matrix: 320x288 / Field of view: 120x120 / Resolution: 0.375x0.4167 (interpolated to 0.375x0.375) mm per pixel and slice thickness: 3 mm (with 0.3 mm gap between adjacent slices). For detailed results, please refer to Appendix D [Table D.1, Table D.2 and Table D.3].

Shape Measures	Radioulnar		Proximal		Distal	
	Controls	Patients	Controls	Patients	Controls	Patients
Eccentricity	0.6781	0.8695	0.7533	0.8905	0.8007	0.9280
Circularity	1.0693	0.7476	0.9433	0.6776	0.8856	0.6582
Area	191.7131	354.0516	309.9184	470.7465	327.4983	365.2587
Area(mm2)	5.1569	6.9415	6.5191	8.0462	6.7373	7.1258
Aspect Ratio	1.4072	2.2074	1.6169	2.4633	1.8587	2.8688

Table 4.1: Mean Shape Measures at proximal, radioulnar and distal carpal row location in the carpal tunnel of controls and patients.

4.5 Analysis of shape quantification results

In this study, it was observed that all the spatial domain shape metrics used to characterise the shape of the median nerve were successful in quantifying the median nerve shape in the control and patient group. The differences in the shape at each location in the carpal tunnel, namely: radioulnar joint, proximal carpal row and distal carpal row are demonstrated using the bar charts shown below for each shape metric.

4.5.1 Circularity

As can be observed in Figure 4.3 below, circularity in controls is higher than the patient group. Also, this holds true at each of the nerve locations in the carpal tunnel. This means that the regular shape of the median nerve is rounder and this has been compromised in the patient group due to an underlying neuropathy that must be investigated clinically.

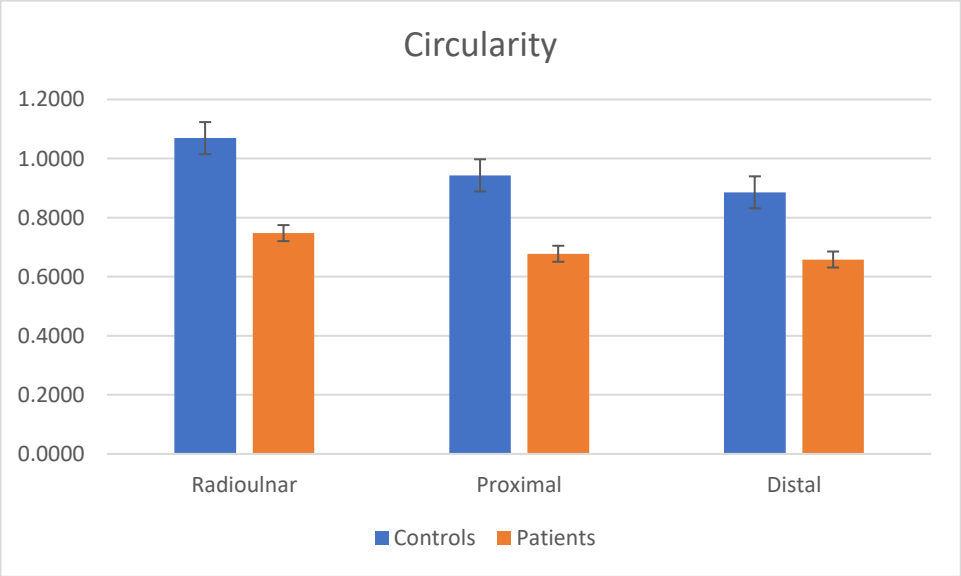

Figure 4.3: Circularity in controls and patients at radioulnar, proximal and distal locations in the carpal tunnel.

4.5.2 Eccentricity

As seen above, the normal round shape of the median nerve was altered in patients and this can be further emphasised by the Eccentricity measure. This measure was significantly higher in the patient group as seen in Figure 4.4 below. The shape of the median nerve in patients seemed to be elongated due to a possible pathology. Eccentricity was observed to be higher at all the three locations in the carpal tunnel.

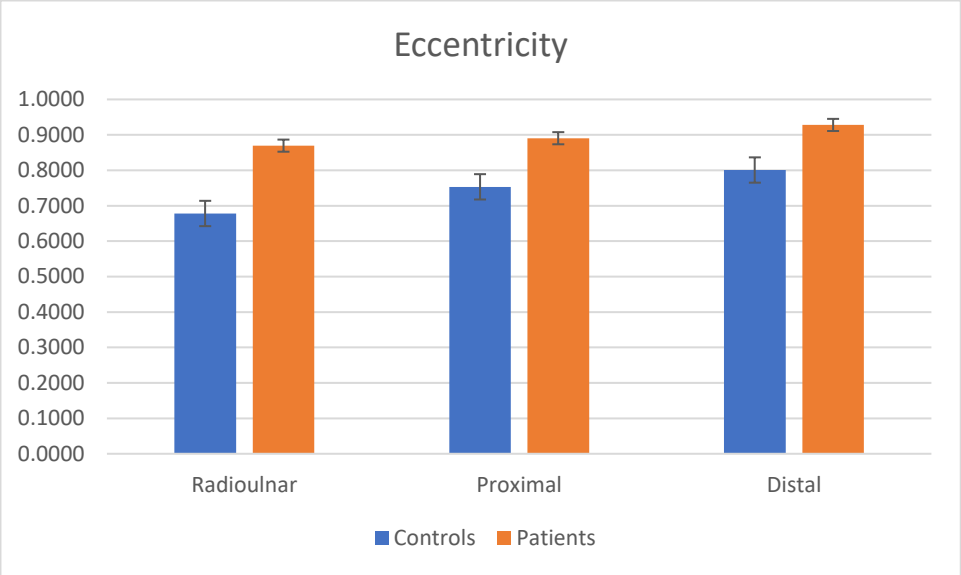

Figure 4.4: Eccentricity in controls and patients at radioulnar, proximal and distal locations in the carpal tunnel.

4.5.3 Median Nerve Area

The median nerve showed possible enlargement of shape due to inflammation or an underlying pathology that was not clearly evident in the clinical findings. Increased area of the median nerve could be signifying a neuropathy that needs to be further investigated by the medical experts. As can be observed in Figure 4.5 and Figure 4.6 below, the area of the median nerve was higher in patients at all the three locations within the carpal tunnel.

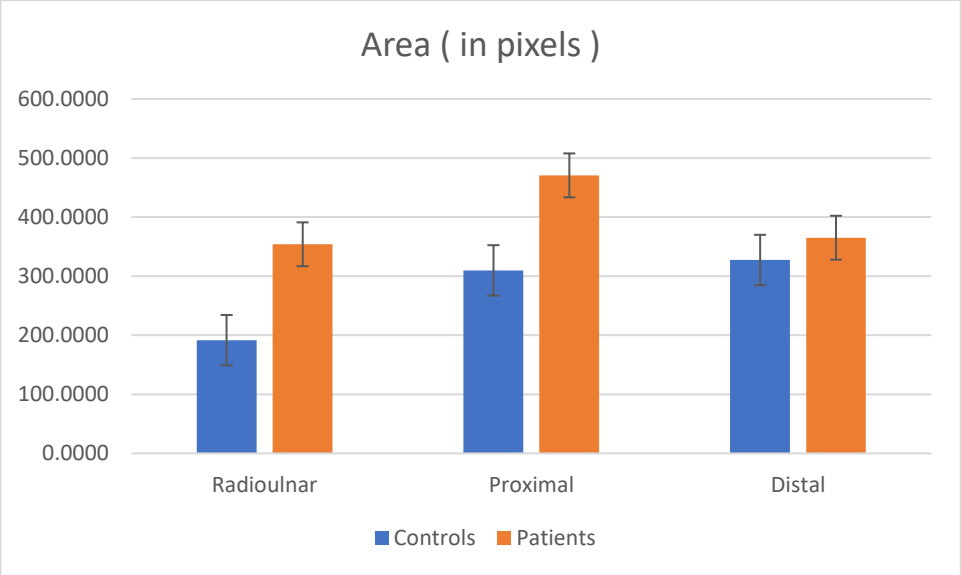

Figure 4.5: Area (in pixels) in controls and patients at radioulnar, proximal and distal locations in the carpal tunnel.

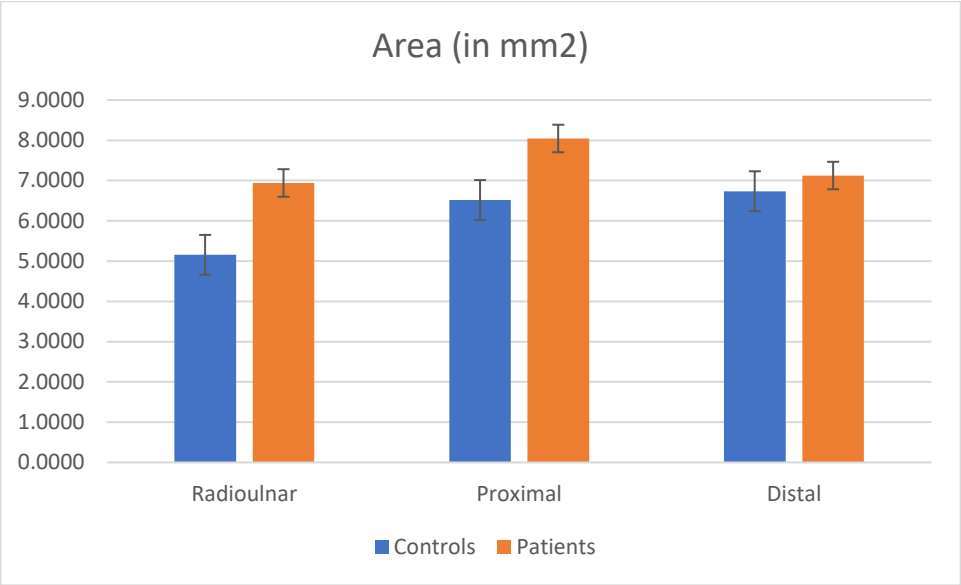

Figure 4.6: Area (in mm^2) in controls and patients at radioulnar, proximal and distal locations in the carpal tunnel.

4.5.4 Median Nerve Perimeter

The median nerve perimeter measure was examined between the control group and the patient group. The perimeter values were investigated at the three locations namely: the radioulnar joint; proximal carpal row; and distal carpal row in the carpal tunnel and are shown in Table 4.2 below. Differences were observed between controls and patients at all the three locations. The mean perimeter measure was higher in patients than that in controls. The higher perimeter of the median nerve boundary (in pixels) could be correlated to its enlargement in patients.

(in pixels)	Controls	Patients	T-test
Radioulnar	32.1296	37.7286	0.1212
Proximal	30.9076	36.3333	0.0665
Distal	25.8030	34.8919	0.0734
P+R+D	29.6134	36.3179	0.0088

Table 4.2: Perimeter measures between controls and patient at radioulnar, proximal and distal carpal rows in the carpal tunnel.

4.5.5 Aspect Ratio

The aspect ratio of the median nerve was higher in the patient group demonstrating the flattened shape of the nerve. This nerve flattening was observed by the medical experts in the MRI of the carpal tunnel. Aspect ratio has been a useful measure in quantifying this observed flattening of the nerve in patients. It was also observed to be consistent across the three locations within the carpal tunnel as can be seen from the Figure 4.7 below.

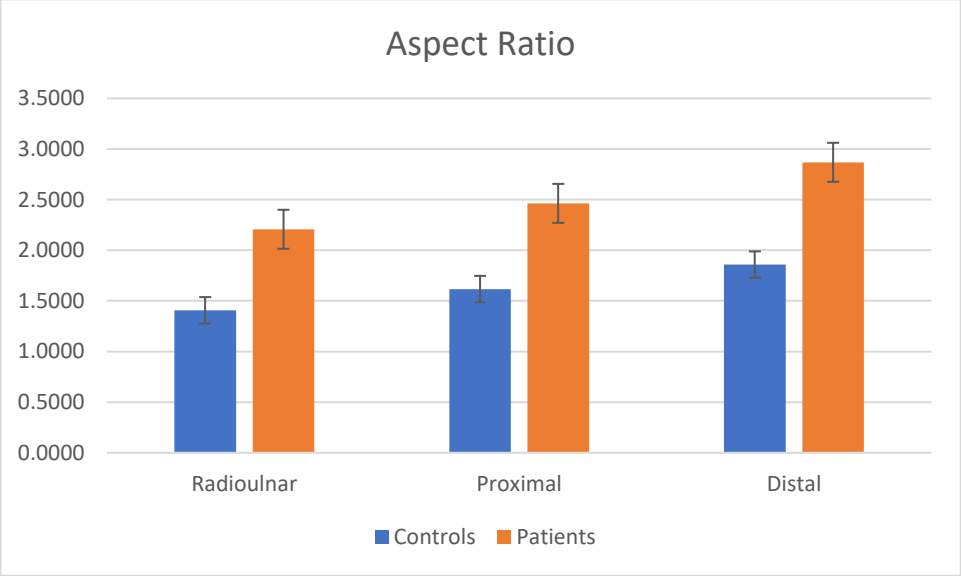

Figure 4.7: Aspect ratio in controls and patients at radioulnar, proximal and distal locations in the carpal tunnel.

4.6 Statistical Analysis

The median nerve area data is summarised in Table 4.1 above. In the healthy control group, the mean area was 5.16 (0.18 SEM), 6.52 (0.30 SEM) and 6.47 (0.24 SEM) mm^2 at the radioulnar joint, proximal and distal carpal row respectively, differences that were significant ($P<0.05$, one-way ANOVA; $P<0.05$, radioulnar joint vs proximal and distal carpal row, Bonferroni *post-hoc* t-test). In the patient group, the nerve area increased by 34.6% at the radioulnar joint (mean = 6.94 (0.48 SEM) mm^2) and 23.4% at the proximal carpal row (mean = 8.05 (0.46 SEM) mm^2) compared to the control group ($p<0.05$, unpaired t-tests). The nerve area at the distal carpal row (mean = 7.13 (0.29 SEM) mm^2) was comparable to the control group ($p = 0.31$, unpaired t-tests).

In the healthy control group, the aspect ratios were 1.41 (0.05 SEM), 1.62 (0.08 SEM) and 1.86 (0.17 SEM) at the radioulnar joint, proximal and distal carpal row respectively ($P<0.05$, one-way ANOVA; $P<0.05$ radioulnar joint vs distal carpal row, Bonferroni *post-hoc* t-test). In the patient group, the nerve was significantly flatter at each location compared to the control group (mean = 2.21 (0.17 SEM), 2.46 (0.19 SEM) and 2.87 (0.22 SEM) at the radioulnar joint, proximal and distal carpal row respectively; $p<0.05$, unpaired t-tests) (as shown in Figure 4.7). Correspondingly, the circularity was also decreased at each location in the patient group as compared to that in the control group (as shown in Figure 4.3).

The perimeter measure, as shown in Table 4.2, was significantly higher as an average of all the three locations within the carpal tunnel in patients than that in controls. The statistical significance of this measure is demonstrated using an unpaired t-test ($P<0.008$).

4.7 Conclusion

In this chapter, we described the implementation of spatial domain shape metrics such as eccentricity, circularity, aspect ratio and the nerve area to quantify the shape of the median nerve. It was observed that all the shape metrics could characterise the shape differences between the control group and the patient group. Statistical analysis proved the statistical significance of these measures. Therefore, it can be concluded that these measures could be reliably used in characterising potential damage to a patient's nerve

The morphological changes demonstrated by shape analysis need further investigation by medical experts to identify the underlying pathology that could be causing them. Also, the shape analysis study needs to be undertaken on a larger dataset to establish the findings of this preliminary study.

Chapter 5

Detection of the median nerve in the carpal tunnel using the OT- MACH filter

5.1 Introduction

In this chapter, the Optimal Trade-Off Maximum Average Correlation Height (OT-MACH) filter was applied to the MR images of the carpal tunnel for detection and localisation of the median nerve [57] . As seen in the earlier chapters, the quantification of the median nerve structure was very effective in classifying the median nerves between controls and patients. It is crucial that the location of the median nerve be accurately identified before implementing segmentation and quantification due to the presence of noise and clutter in the form of the tendons that surround the median nerve.

Traditionally, Synthetic Discriminant Filters (SDF) are applied for such a task of object detection by imposing hard constraints on the output of the filter. However, in this case, due to presence of variable background clutter, the SDF is not a viable option. The MACH filter on the other hand, employs unconstrained correlation criteria. It was introduced as a distortion invariant correlation filter and has diverse applications in the field of surveillance and security for automatic target detection. To the best of our knowledge, it has never been implemented in a medical image analysis problem to detect and locate objects of interest.

The MACH filter avoids the problem of selecting constraints such as in SDF filters by acquiring a large average peak without assigning constraints to individual training images by employing unconstrained correlation criteria. The OT-MACH filter has improved performance as compared to the traditional MACH filter and the results of experimentation using the OT-MACH filter are presented in this chapter.

5.2 The MACH Filter

The traditional MACH filter can be expressed in its simplest form using a filter transfer function as given below:

$$h = (S + \gamma \cdot I)^{-1} \cdot m \qquad \textbf{Equation 5.1}$$

The MACH filter transfer function, in equation 5.1 above, has the capability to adjust the correlation planes to a suitable value for optimizing the performance. The MACH filter's ability to handle distortions depends largely on the expected distortion within the training sets which are used in the design of the filter. The detailed design of the MACH filter is described in the following papers [57] [58] [59] [60].The robustness of the MACH filter is due to the inclusion of Average Similarity Measure (ASM) criterion in the denominator of the transfer function along with the Output Noise Variance (ONV) which reduces the sensitivity to distortions and contributes to the removal of the hard constraints on the correlation peak. The MACH filter's ability to handle distortions depends largely on the expected distortion within the training set which are used in the design of the filter.

The MACH filter discussed above utilizes the unconstrained correlation criteria to detect target objects from cluttered backgrounds. Although robust in nature the classical MACH has room for improvements and hence over the years a lot of advancements have been

proposed. One such advancement is the OT-MACH and this is discussed in the following section.

5.3 The OT-MACH filter

In this section, an OT-MACH filter has been designed to test the effectiveness at detecting the location of the median nerve in the carpal tunnel. The major aim of the OT-MACH filter is to find the optimal compromise between good discrimination ability and distortion tolerance in the presence of noise. The MACH filter, as seen earlier, maximizes the height of the correlation peak with respect to the distortions in the training images. As the peak height of the MACH filter is unconstrained, it makes it difficult to interpret the results demonstrated by the correlation.

The OT-MACH filter can be described by the filter transfer function given below [57]:

$$h = \frac{m_x^*}{\alpha C + \beta D_x + \gamma S_x} \qquad \textbf{Equation 5.2}$$

In the OT-MACH filter transfer function α, β and γ are the non-negative parameters, m_x is the average of the training image vector $x_1, x_2, ..., x_N$ (in the frequency domain), and C is the diagonal power spectral density matrix of additive input noise. It is usually set as the white noise covariance matrix, $C = \sigma^2 I$. Also D_x is the diagonal average power spectral density of the training images and S_x denotes the similarity matrix of the training images [57].

In the case of the OT-MACH filter the different values of α, β and γ control the filter's behaviour to match different application requirements. If $\beta=\gamma=0$, the resulting filter behaves much like a MVSDF filter with relatively good noise tolerance but broad peaks. If $\alpha=\gamma=0$ then the filter behaves more like a MACE filter which generally exhibits sharp

peaks and good clutter suppression but is very sensitive to distortion of the target object [59]. If $\alpha=\beta=0$, the filter gives high tolerance for distortion but is less discriminating

5.4 Performance Metrics for correlation filters

To define the criteria of detection it is necessary to calculate some basic measures to represent the quality of the output correlation plane.

The most basic measure of the correlation plane is the correlation output peak intensity (COPI) which is defined as [61] :

$$COPI = \left\{ \left| C(x, y) \right|^2 \right\} \qquad \textbf{Equation 5.3}$$

where the value of $C(x, y)$ is the amplitude of the output correlation plane at position (x, y).

To provide the best detection capability and performance it is necessary for a filter to yield a sharp correlation peak as well as a high COPI value, while keeping side lobes to a minimum. The filter's ability to do this can be measured using the peak-to-correlation energy (PCE) measure.

The basis of the PCE measure is that the correlation peak intensity should be as high as possible while the overall correlation energy in the plane should be as low as possible. A high PCE value therefore implies that the filter performs well. The PCE ratio is generally defined as [61]:

$$PCE = \frac{COPI}{Energy} \qquad \textbf{Equation 5.4}$$

where *Energy* is the total correlation plane energy and is defined as:

$$Energy = \sum \left| C(x, y) \right|^2 \qquad \textbf{Equation 5.5}$$

Also, another parameter in defining the performance of a correlation filter is Peak to Side Lobe Ratio (PSR) which forms an important criterion especially in the case when multiple objects are present in the input scene. In most cases considering just the COPI values would not be enough to analyse the performance of the filter. The PSR is calculated by subtracting the mean of the correlation plane from the COPI and then dividing it by the standard deviation of the correlation plane [62]:

$$PSR = \frac{(COPI - MEAN)}{\sigma} \qquad \textbf{Equation 5.6}$$

where σ denotes the standard deviation of the correlation plane intensity values. The PSR of the target object should be greater than background clutter. It can be used in the case when the difference between the two COPI values of the target and reference objects is negligible.

PSR is a metric that has been widely used to measure the sharpness of the correlation peaks. When the target belongs to a true class, the PSR values should be high and in the case of false class objects the PSR value should be low. Now in order to effectively compute PSR the test image is cross-correlated with the reference image and the output correlation plane is scanned for the largest value. When computing the detection criteria many projections should be used instead of a single projection of inner products as this enables the correlation filter to produce a specific response facilitating an accurate detection. It has also been observed that the PSR metric is invariant to changes in illumination of the training images [63] [64].

5.5 Applications

The MACH filter has been used for automatic pedestrian detection and tracking by Han and Yao [65]. It is known that automatic pedestrian tracking and detection can be challenging as the appearance of pedestrians changes with alterations such as clothes, pose and size. Also, the weather and illumination conditions vary and the tracking and detection must be processed in dynamic scenes. The MACH filter has been combined with a particle filter to locate the targets in real time. This study has proven the effectiveness of the filters when there is a block or occlusion in tracking. The study applied the MACH filter to synthesize a composite filter using the frequency characteristics of pedestrians' different views, mainly for the detection of the pedestrians. Once the position was given by the correlation filter, a particle filter was used to track the people. The MACH filter is known to be distortion tolerant and gives a reliable estimation to relocate them. Fast Fourier transforms were performed on different views of the pedestrians in the training dataset and then were combined into a MACH detection filter. If the output was a peak, it was assumed that there was a pedestrian. The results suggested that the combination of MACH based correlation to detect, and the particle filter to track, pedestrians was robust even when there were occlusions [65].

Also in a study by Rodriguez *et al*. [66] a spatio-temporal Maximum Average Correlation Height filter was used for action recognition and is termed as the Action-MACH. In this study, the MACH filter is trained on video templates which include various human actions such as jumping jacks. These actions are then tested with a data set [66].

Having diverse applications in the field of surveillance and security, the MACH filter has also been used in automatic target recognition (ATR) of Forward Looking Infrared images [67]. In the security and defence industry infrared cameras are used for target

recognition as it is impossible to camouflage the heat generated from targets which may be humans, animals or vehicles. These thermal images are obtained by sensing the radiation in the infrared spectrum, which is either emitted or reflected by the objects in the scene as mentioned earlier. The application of the OT-MACH has been tested in one such study by Alkandri [68].

In another study by Nagachetan *et al*. [69] the OT-MACH filter has been implemented as a robust tracker for motor vehicles from aerial video imagery. The algorithm designed in this paper allowed the operator to manually select the object of interest. The filter exhibited good tolerance to changes in lighting, scale and orientation [69].

In a recent study by Gardezi *et al.* [70] the spatial domain OT-MACH was implemented for vehicle monitoring. In this paper, VANET parameters were combined with the OT - MACH filter to reduce the processing overhead when working with large video datasets [70].

5.6 Experimentation

All implementations of the OT-MACH filter are realised via the frequency domain in order to increase the speed of calculation and to allow ease of tuning of the filter transfer function [57-59]. The most crucial step in tuning the OT-MACH filter is the choice of the values for the α , β and γ parameters. In this experiment, three training sets were created. The first training set comprised of median nerve images in the distal location in the carpal tunnel of a patient. The median nerve of a single patient was rotated and resized using bilinear interpolation to create a set of the same sized training images. This training set was used to test the performance of the OT-MACH filter to rotational invariance. The second set consisted of the median nerves of all the patients from the dataset at the distal location. This training set was used to test how intra-class variation among patients affected the performance of the OT-MACH filter. The third set was used to test the performance of the filter for out of class images of the median nerve.

The image containing the median nerve at the distal location in the carpal tunnel was used as the target image and used to test the filter. It is shown in Figure 5.1 below.

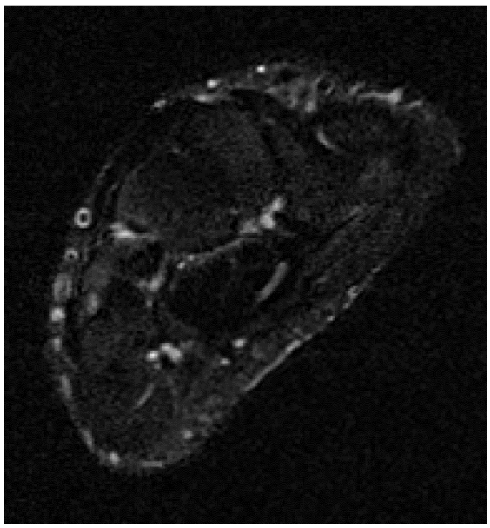

Figure 5.1: A MR image of the carpal tunnel used for testing the OT-MACH filter

5.6.1 Case I

In this step, a single image of the median nerve was used to train the filter. The same image was given as input for correlation much like an autocorrelation function.

The performance parameters used in the OT-MACH filter function were set to $\alpha = 0.1$, $\beta = 0.1$ and $\gamma = 0.001$. The α value was set as low as possible for a sharper correlation peak. The high β value resulted in poor distortion tolerance but gave a sharp correlation peak. The gamma values were set to low to maximize the ability of the filter to discriminate between in-class and out of class nerve images.

As expected, the results produced a sharp correlation peak and no out of class peaks. The average peak to correlation energy (PCE) value of the resultant correlation plane was 0.076. This is an ideal case scenario as there was no background clutter and no orientation changes. The result of the correlation can be seen in figure 5.2 below.

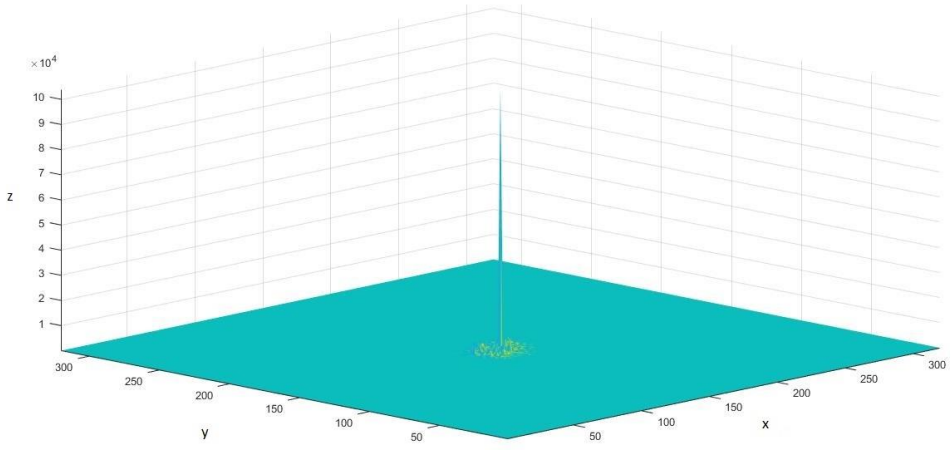

Figure 5.2: Correlation output of OT-MACH using a single image and the same test image.

5.6.2 Case II

The performance parameters used in the OT-MACH filter function were set to α = 0.01, β = 0.01 and γ = 0.001. In this case, we used the same parameter values as in Case I. However, instead of using a single nerve image to train the filter, a set of training images was used to train the filter. As can be seen in the figure 5.3 below, the location of the nerve was not detected due to background noise and multiple peaks. The correlation filter was unable to detect the location of the median nerve with the parameter values given above. The resultant values for PCE, COPI and PSR of the peak were: 0.0009, 0.005, 7.6376, respectively. However, the maximum peak was not at the location of the nerve.

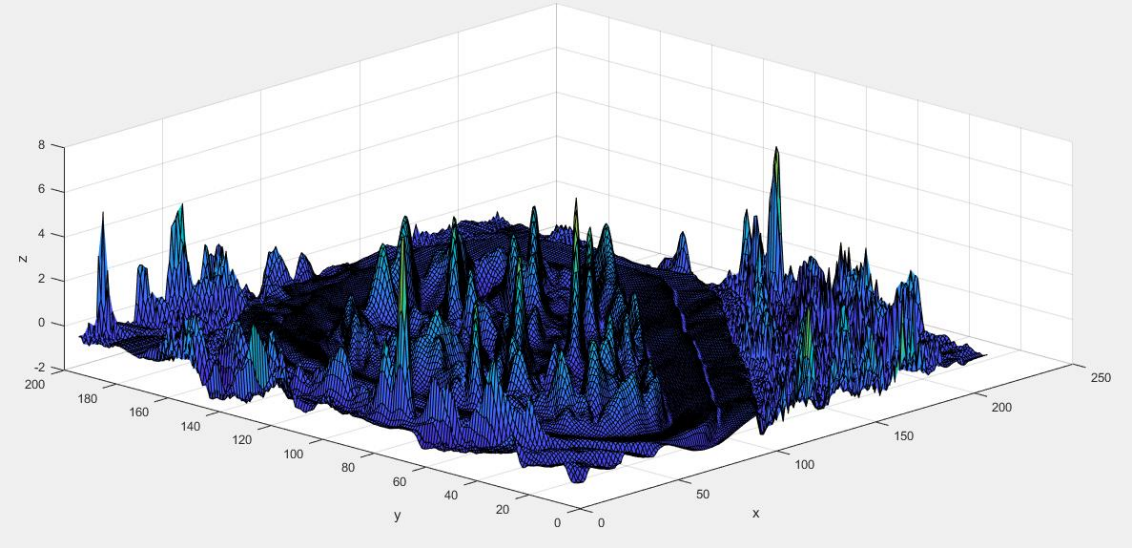

Figure 5.3: Correlation output of OT-MACH in Case II

5.6.3 Case III

The performance parameters used in the OT-MACH filter function were set to α = 0.001, β = 0.01 and γ = 0.001. In this case, we used the same parameter values as in Case I. However, instead of using the same nerve image as a test image, the composite image of nine in-class training images was used. As it can be seen in the figure 5.4 below, the location of the nerve was not detected due to background noise and multiple peaks. The correlation filter was unable to detect the location of the median nerve with the parameter values given above. The resultant values for PCE, COPI and PSR of the peak were: 0.0009, 0.005, 7.6376, respectively. However, the maximum peak was not at nerve location.

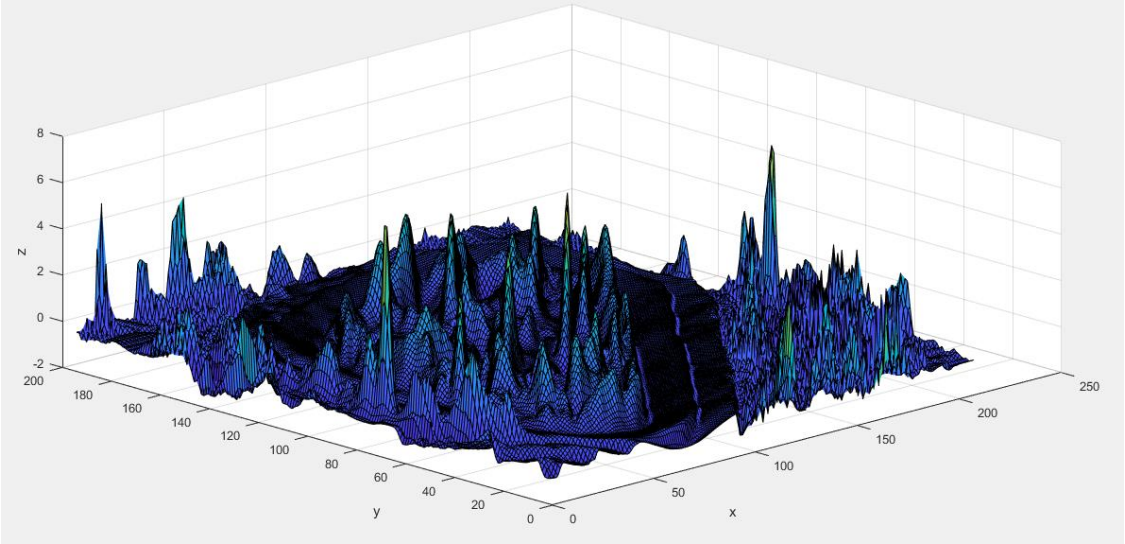

Figure 5.4: Correlation output of OT-MACH in case III

5.6.4 Case IV

The performance parameters used in the OT-MACH filter function were set to α = 0.0001, β = 0.01 and γ = 0.001. When filter was correlated with the test image, a peak was observed at the location of the nerve in the carpal tunnel. Although the peak was distinct, it was surrounded by noise peaks. As it can be seen in the figure 5.5 below, the location of the nerve is detected but is not significant enough due to background noise and multiple peaks. Therefore, further experimentation is needed to find a balance in the parameter values that suppress the noise peaks. The resultant values for PCE, COPI and PSR of the peak were: 0.0012, 11.6863, 9.7094, respectively. It can be observed that the COPI value improved significantly as compared to Case III. Also, the maximum peak height was higher than in the previous case.

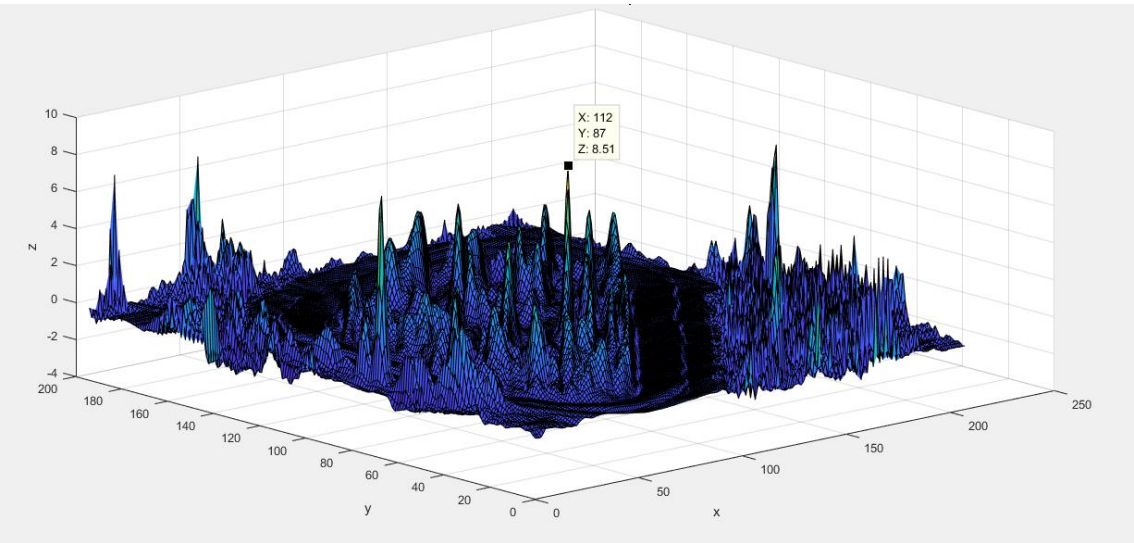

Figure 5.5: Correlation output of OT-MACH in Case IV

5.6.5 Case V

The performance parameters used in the OT-MACH filter function were set to α = 0.00001, β = 0.01 and γ = 0.001. It can be observed in figure 5.6 below that the filter was successful in suppressing noise and giving a distinct correlation peak output at the location of the median nerve inside the carpal tunnel. The resultant values for PCE, COPI and PSR of the peak were: 0.0015, 59.9154 and 19.7662, respectively. The PCE and PSR values improved considerably as compared to those in Case IV. Therefore, it can be inferred that the parameter values used in this case have found a near optimum output. To see if any further change would improve the correlation output further, a few more parameter values are tested in the following cases.

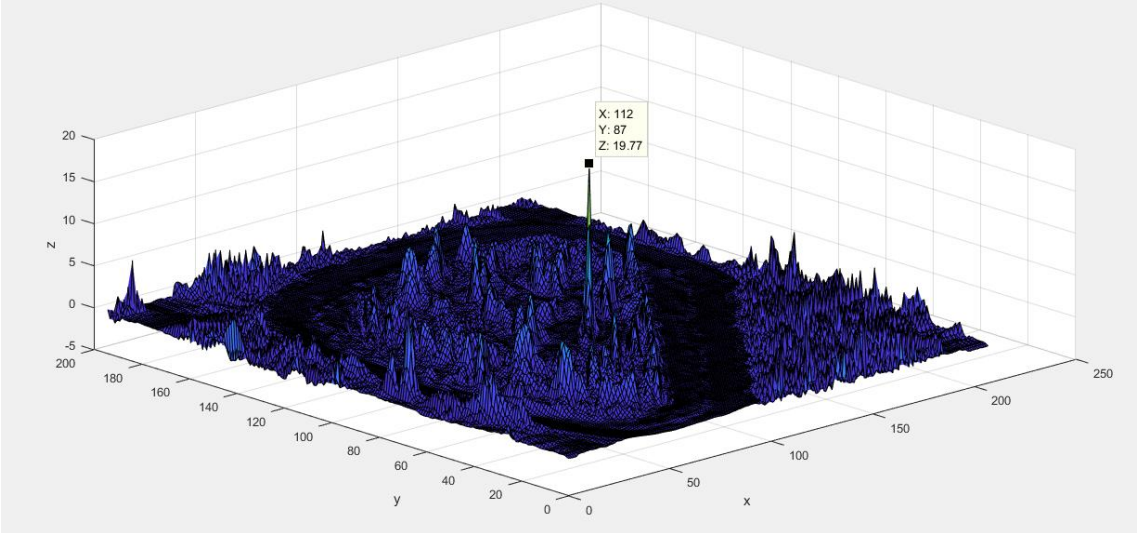

Figure 5.6: Correlation output of OT-MACH in Case V

5.6.6 Case VI

The performance parameters used in the OT-MACH filter function were set to α = 0.000001, β = 0.01 and γ = 0.001. The resultant values for PCE, COPI and PSR of the peak were: 0.0027, 382.1690 and 65.2435, respectively. As seen in the figure 5.7, a prominent peak is observed at the location with a good suppression of the noise peaks. Also, the PSR value is significantly improved from the previous Case V.

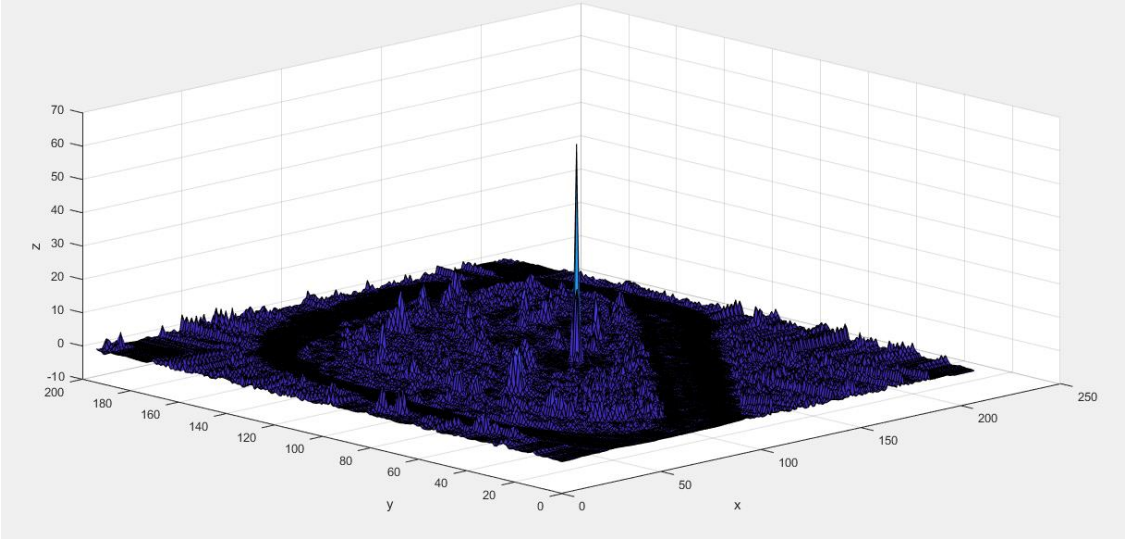

Figure 5.7: Correlation output of OT-MACH in case VI

5.6.7 Case VII

The performance parameters used in the OT-MACH filter function were set to α = 0.0000001, β = 0.01 and γ = 0.001. The output of the correlation peak was further improved by reducing the α value. As seen in figure 5.8 below, noise suppression has improved significantly owing to the low α value. The resultant values for PCE, COPI and PSR of the peak were: 0.0029, 1863.8 and 85.2645, respectively. It was found that any further change in the α value did not improve the performance metrics of the correlation output. Hence, further experimentation was done by changing the β value in the following cases.

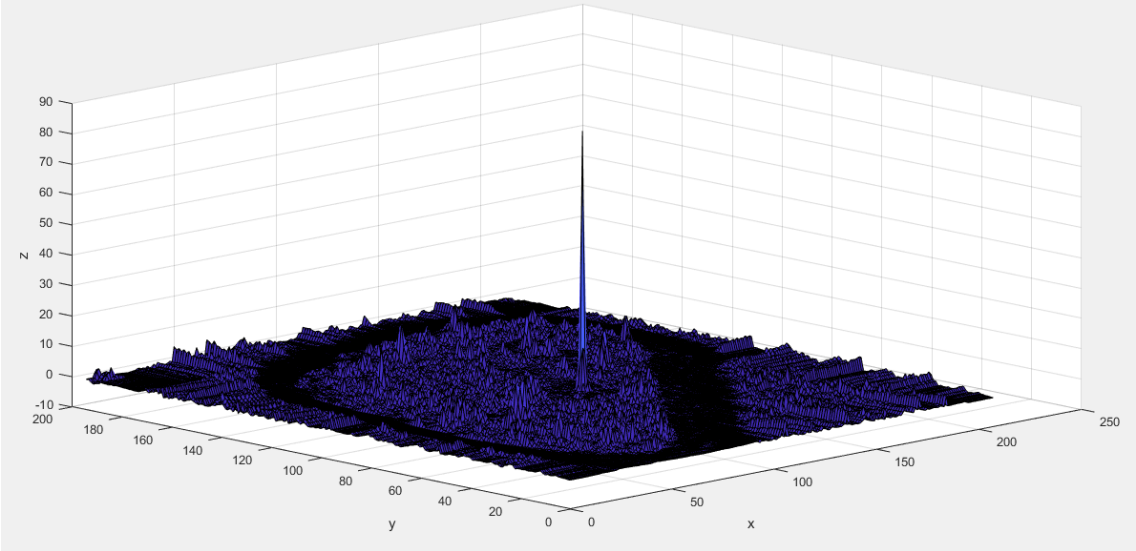

Figure 5.8: Correlation output of OT-MACH in Case VII

5.6.8 Case VIII

The performance parameters used in the OT-MACH filter function were set to α = 0.0000001, β = 0.001 and γ = 0.001. The β value was reduced to 0.001 and the correlation output was examined. The correlation output can be seen below in figure 5.9. The resultant values for PCE, COPI and PSR of the peak were: 0.0027, 38217.0 and 65.2435, respectively. It was observed that although the COPI value increased drastically, the PCE and PSR values decreased as compared to those in Case VII.

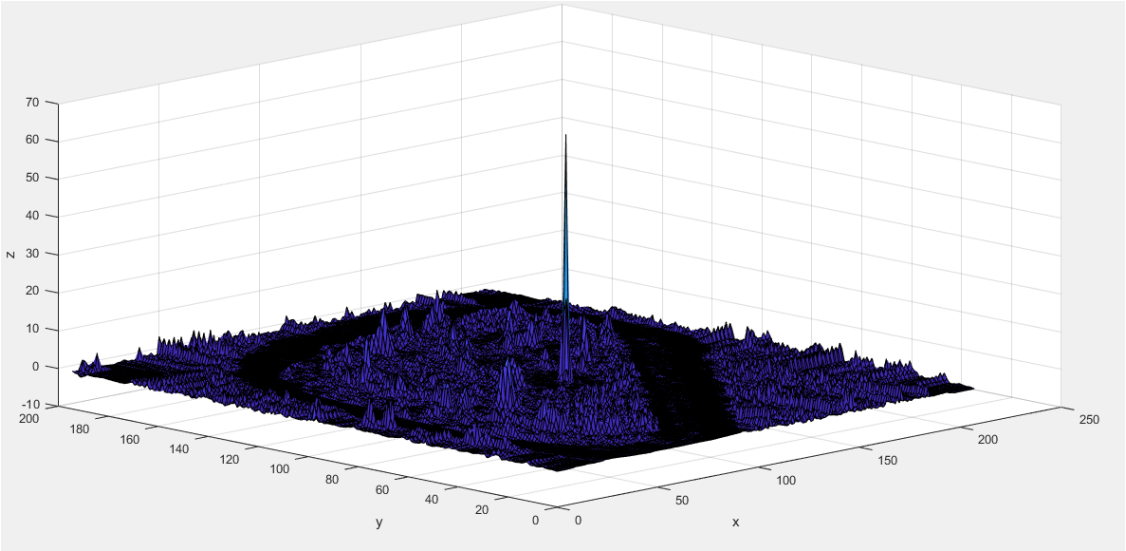

Figure 5.9: Correlation output of OT-MACH in Case VIII

5.6.9 Case IX

The performance parameters used in the OT-MACH filter function were set to α = 0.0000001, β = 0.1 and γ = 0.001. In this case, the β value was increased to observe how this would affect the correlation output. It can be observed in the figure 5.10 below, that although the correlation output showed a distinct peak and improved noise suppression like previous Case VIII, the performance metrics were adversely affected. The values of PCE, COPI and PSR were: 0.0021, 43.8479 and 59.0208, respectively. The PCE and PSR values decreased as compared to those in the previous cases.

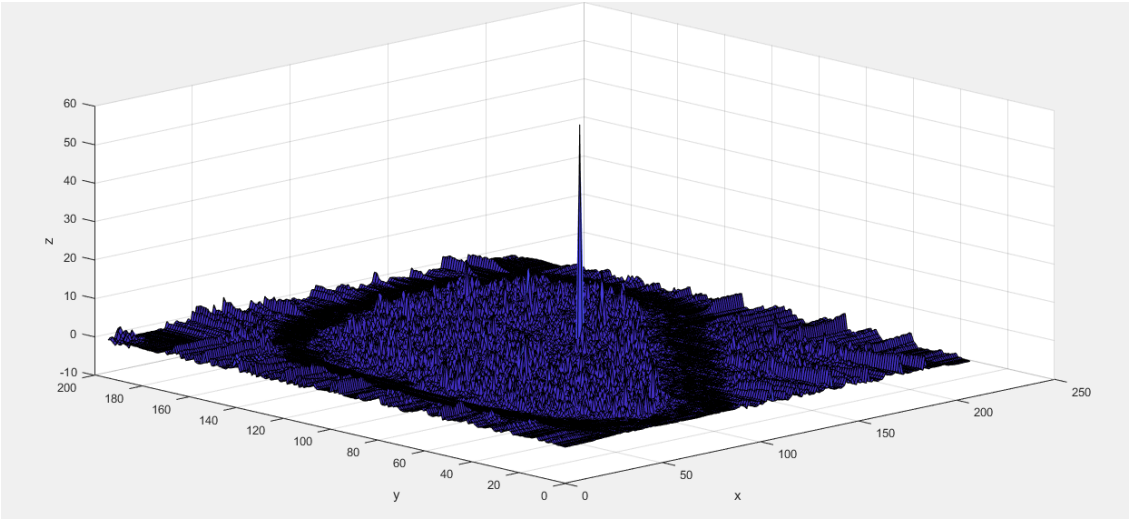

Figure 5.10: Correlation output of OT-MACH in Case IX

5.6.10 Case X

The performance parameters used in the OT-MACH filter function were set to α = 0.0000001, β = 0.2 and γ = 0.001. In this case, we increased the β parameter value to 0.2 and there was no meaningful change in the correlation output. The resultant values for PCE, COPI and PSR of the peak were: 0.0018, 12.4183 and 49.1168, respectively. The correlation output can be seen in figure 5.11 below.

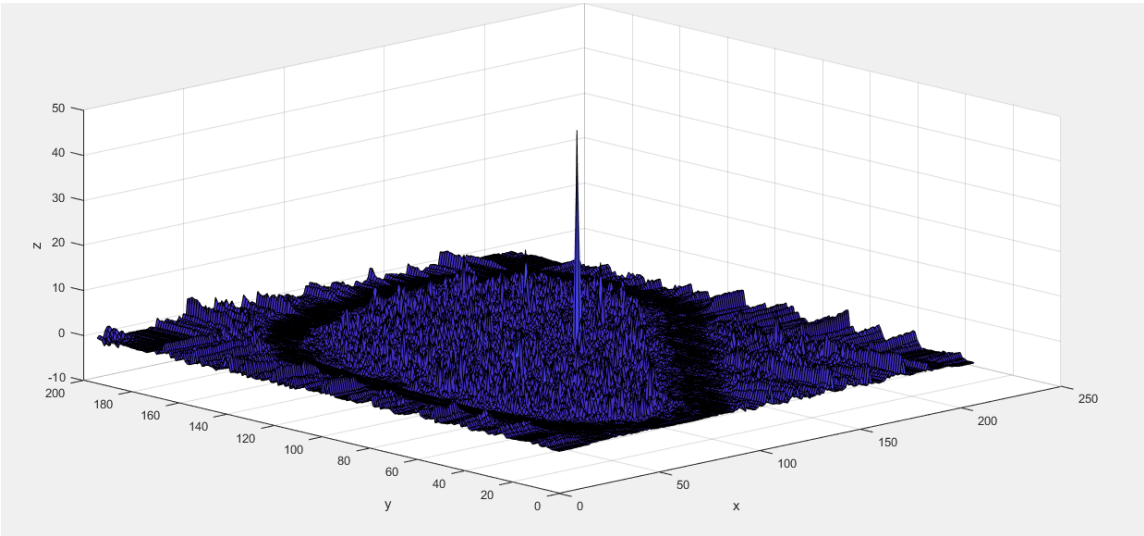

Figure 5.11: Correlation output of OT-MACH in Case X

5.6.11 Case XI

The performance parameters used in the OT-MACH filter function were set to α = 0.0000001, β = 0.5 and γ = 0.001. In this case, we increased the β parameter value to 0.5 and the values of the performance metrics were affected. The resultant values for PCE, COPI and PSR of the peak were 0.0015, 2.2038 and 38.9475 respectively. The correlation output can be seen in figure 5.12 below.

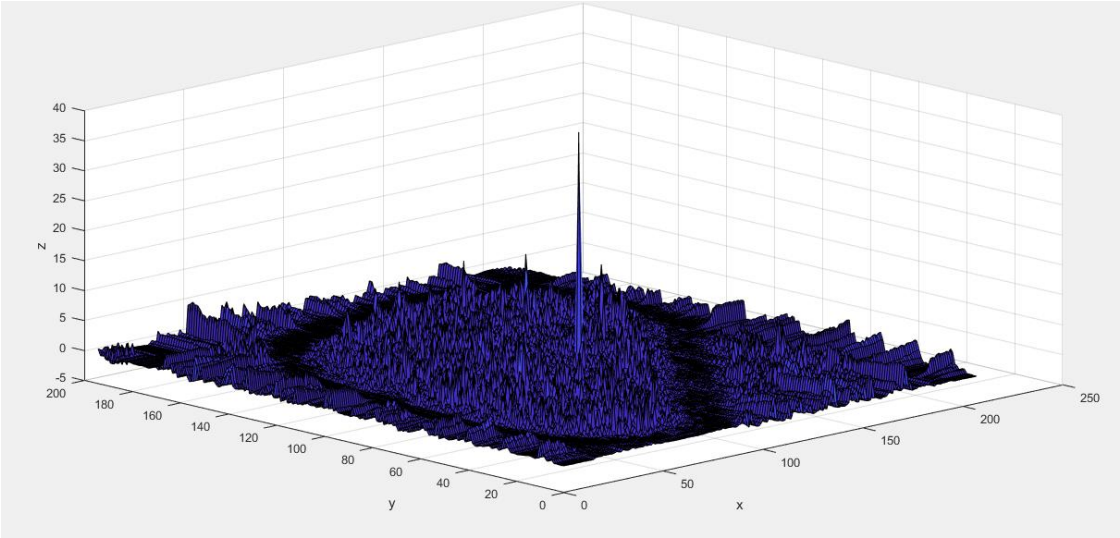

Figure 5.12: Correlation output of OT-MACH in Case XI

5.6.12 Case XII

The performance parameters used in the OT-MACH filter function were set to α = 0.0000001, β = 0.5 and γ = 0.001. In this case, we increased the β parameter value to 0.9 and the values of the performance metrics were affected. The resultant values for PCE, COPI and PSR of the peak were: 0.0013, 0.7134 and 34.4294, respectively. The correlation output can be seen in figure 5.13 below.

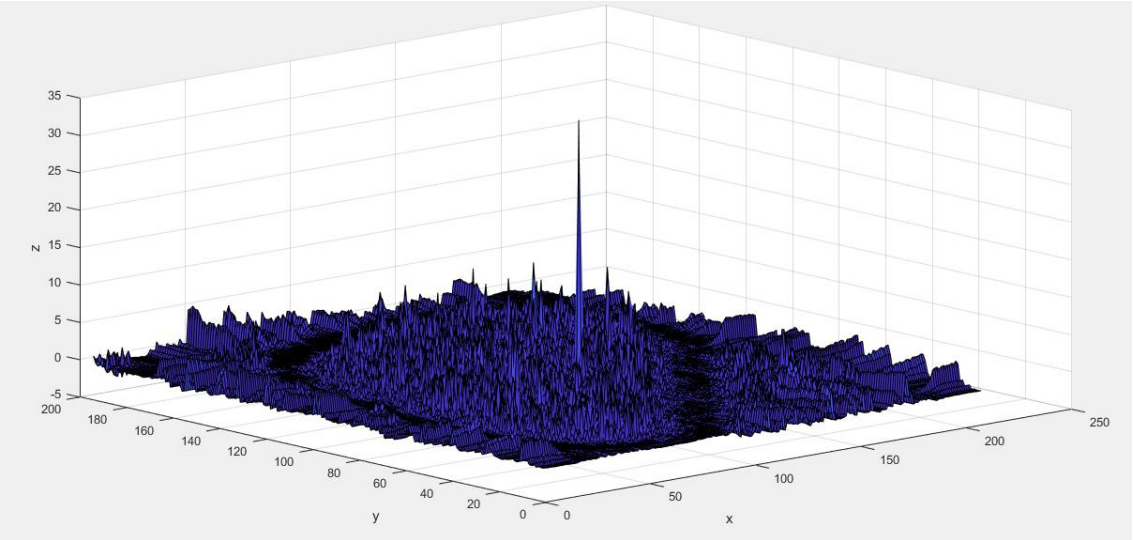

Figure 5.13: Correlation output of OT-MACH in Case XII

The following table 5.1 summarizes the performance metrics and the parameter values used in the experimentation in this chapter.

	α	**β**	γ	**PCE**	**COPI**	**PSR**
Case I	0.1	0.1	0.001	0.0274	0.2387	15.8304
Case II	0.01	0.01	0.001	0.0009	0.0055	7.6376
Case III	0.001	0.01	0.001	0.0009	0.4339	8.0223
Case IV	0.0001	0.01	0.001	0.0012	11.6863	9.7094
Case V	0.00001	0.01	0.001	0.0015	59.9154	19.7662
Case VI	0.000001	0.01	0.001	0.0027	382.1690	65.2435
Case VII	0.0000001	0.01	0.001	0.0029	1863.8000	85.2645
Case VIII	0.0000001	0.001	0.001	0.0027	38217.0000	65.2435
Case IX	0.0000001	0.1	0.001	0.0021	43.8479	59.0208
Case X	0.0000001	0.2	0.001	0.0018	12.4183	49.1168
Case XI	0.0000001	0.5	0.001	0.0015	2.2038	38.9475
Case XII	0.0000001	0.9	0.001	0.0013	0.7134	34.4294

Table 5.1: Summary of filter parameters and performance metrics

5.7 Conclusion

In this chapter, the filter design of the MACH filter, and its enhancement the OT-MACH, were discussed. The filter function of the OT-MACH filter was tested using different values of the α, β, and γ parameters to detect the location of the median nerve in the carpal tunnel images. It was observed that the OT-MACH filter could detect the location when the training set consists of reference images rotated at different angles to produce rotational invariance. However, when the filter was trained using nerve images of different subjects to accommodate intra-class variation, a sharp peak was detected at the location of the nerve but also with numerous out of class peaks. This could be due to the overall quality of the MR image and the various aspects of the anatomy of the carpal tunnel that caused a high amount of noise and false detections.

When the α was decreased and the β and γ values were kept constant, the correlation output improved and there was a distinct correlation peak with very good noise suppression that was robust against intra-class variation. When an optimum value of α was found, increases in the β value was investigated. It was observed that increasing the β value did not improve the correlation output. Although the correlation peak remained distinct, the performance metrics were adversely affected. When we changed the γ values, no change in the performance of the correlation output was observed.

Chapter 6

Classification Using Features Extracted from Image Data

6.1 Introduction

In the previous chapters, features were extracted using texture analysis methods such as co-occurrence matrices, run length matrices, autocorrelation and spatial domain shape metrics. We attempted to study the patterns of texture and shape that may help classify the nerves as belonging to the control or patient group. In any pattern recognition problem, the most important and the last step is classification. Classification enables identification of classes that a pattern belongs to. In machine learning and statistics, the classification process involves developing a classifier that is trained on a set of training data. This classification model is then used on test data to validate the robustness of the model. As the work in this thesis involves classifying nerves into two categories namely normal or patient nerve, this is a binary classification problem.

6.2 Methods of Binary Classification

A brief overview of the different methods of binary classification is presented.

6.2.1 Decision Trees

A decision tree algorithm can be designed for classification and regression. In classification, it can be described as binary classification tree [71]. A decision tree has a

multistage decision process. Decision trees mainly consist of nodes that are labelled as features, edges labelled as values and the leaves can be expressed as class labels. These class labels enable the classifier decision. Decision trees are efficient classifiers that can model complex non-linear decision boundaries by breaking up a complex decision into a number of simpler decisions at the nodes in the tree structure [72].

6.2.2 Random Forests

Random forests also called random decision forests can be defined as an ensemble learning classification method. Ensemble learning combines different learning algorithms to improve the predictive performance of classifiers as compared to them being used individually. It combines the decisions made by multiple decision trees using a majority vote decision rule [73]. These decision trees are created by constructing bootstrap samples of the data. The first random forest algorithm was created using the random subspace method [74] [75].

6.2.3 Bayesian networks

Bayesian networks provide a probabilistic graphical model of variables and the relationships between them. This representation can be provided a priori or can be learned from the available data. The structure allows multivariate density functions to be specified using a chain rule. Bayesian networks are used to model many complex problems in spite of its oversimplified assumptions and performs well even when small amounts of data are available [71].

6.2.4 Support Vector Machines

Support Vector Machines (SVMs) is a supervised classification approach that has been widely researched and used in classification problems [71]. SVMs work on the basic

principle of creating the best separating hyperplane between pattern vectors in the training data to distinguish between the members of the two classes. It can either be applied directly to variables or in a transformed feature space [76]. For data that is linearly separable, SVMs can used a linear classification function to create a hyperplane that passes between the two classes. In this case, the new test data can be classified simply by testing the sign of this linear function. As many such hyperplanes exist, SVMs provide robustness by using the hyperplane that maximizes the margin between the two classes ensuring optimal classification. SVMs are mainly used in binary classification but multiclass SVMs also exist which work based on a one against all binary classifier or multiple one against one situations [76].

6.2.5 Artificial Neural Networks

Artificial neural networks are an effective method of classification. They have been widely used in research and for industrial applications. Artificial neural networks have many variations that depend on the number of neurons used, number of layers and the different weights used while training a neural network for a classification problem [71] [77]. The design of the neural network is application dependent and has found diverse applications in the fields of biometrics, object recognition, medical diagnosis and complex machine vision problems. The most promising and widely researched field of ANNs is Deep Learning. Deep Learning solves complex machine vision problems by representing a complex problem as numerous simpler representations. The best example of a deep learning model is a multilayer perceptron (MLP) that can be simply described as a function mapping input values to output values [78]. Deep Learning models have multiple hidden neural network layers that create simpler representations of data, the depth creation improving performance [79]. Deep learning research has also gained

momentum due to the increases in computing power available with parallel processing units.

6.3 Classification using Small Datasets

As seen in the previous section, classification is a crucial step in any machine vision or pattern recognition problems. As supervised classification methods used for binary classification are trained on a training dataset and a predictive model is created, the size of the dataset is very important. In cases such as in this thesis, the amount of data available for training was very small as this was a preliminary study conducted to analyse the nerves in whiplash patients. Nonetheless, classification models need to be built and implemented for given small data problems. In this section, we review some of the techniques used for effectively learning from smaller datasets.

6.3.1 Diffusion Neural Network

Diffusion neural networks (DNNs) are designed by a combination of back-propagation neural networks with information diffusion methods [71]. The information diffusion techniques were suggested to combat the small data sample problem by using fuzzy set theory and are used to derive more patterns for training from the original small dataset [80] [81]. DNNs reduce the error of conventional back-propagation networks by about 48 percent [80]. However, as the symmetric diffusion techniques oversimplify the generation of new samples, it can cause under-estimation or over estimation of the data range and lead to a reduction in accuracy. This led to the development of the mega-trend-diffusion technique that combined data trend estimation and mega diffusion to avoid over estimation [80]. However, this increases the complexity of the computations involved in DNNs as compared to those in ANNs.

6.3.2 Mega Trend Diffusion Function

As discussed earlier, the mega-trend diffusion technique is a combination of data trend estimates and information diffusion. It has been found to greatly improve learning accuracy as compared to a traditional back-propagation neural network. A detailed overview of mega-trend-diffusion (MTD) can be found in [80] [82] [83].

6.3.3 Bootstrap Resampling Method

The Bootstrap resampling method involves choosing random samples with replacement from a data set and analysing each sample the same way [44]. It is often used in preliminary studies where initial available data is small. Using bootstrap methods, predictive models can be built faster as the random resampling increases the amount of training data by creating virtual samples [71]. Having insufficient data to train a classification model might make the model fragile and reduce the robustness of the classifier. As in most pilot runs and preliminary investigations data samples are small, bootstrap methods are used. A detailed overview of the bootstrap methods can be found in [84] [85]. The error rate can be decreased by executing the bootstrap procedure once for every input factor.

6.4 Experimentation Method

In this section, the method used to approach the Whiplash classification problem is addressed. Classification is approached in two ways, namely SVM classification using shape features and SVM classification using texture features. This is done to analyse which of the two feature sets are more robust at classifying the nerves into two classes, namely control and patient. The shape features used in the SVM classifier were analysed for statistical significance using the t-test as described in Chapter 4. Although the metrics were statistically different between controls and patients, the data set is small and might make the classification model fragile and reduce the robustness. Therefore, first SVM is used on the original data and the accuracy is noted. Then, bootstrapping is used to resample the input data and this resampled data is used for classification using SVM. This is done to analyse to determine if, by using bootstrapping resampling, the accuracy can be improved further.

The texture features used in the second SVM classifier were extracted from co-occurrence matrices and run length matrices. These features demonstrated differences between the control and patient group; however, the statistical significance could not be proved. Also, for each subject, 23 texture features were extracted in three locations of the median nerve in the carpal tunnel. Identifying a separating hyperplane using SVM in the original data is tested. In addition to this, principal component analysis (PCA) is used to identify the principal components that describe the largest possible variance in the data. PCA is a statistical procedure used for dimensionality reduction [86]. It uses an orthogonal transformation to convert a set of possibly correlated variables into a set of linearly

uncorrelated variables called principal components. The classification models are built and tested using MATLAB [56].

6.5 Performance Measures

Performance of the classification model is tested for diagnostic accuracy. Diagnostic accuracy relates to the ability of the model to discriminate between normal nerves and the target condition in this case the inflammation of nerves caused by whiplash injuries [87]. The performance measures used to evaluate the classifier accuracy are: sensitivity or True Positive Rate (TPR); specificity or True Negative Rate (TNR); total accuracy (TA); positive predictive value (PPV); and negative predictive value (NPV). A full explanation of these measures can be found in [88].

6.6 Applications

In a study by Al Samarraie *et al.* [89] texture classification was performed on two databases namely, the Outex and Columbia-Utrecht Reflectance and Texture database (CUReT) databases, using random forests and support vector machines. Texture features were extracted using bi- orthogonal wavelet transforms, first order features and co-occurrence matrices. Classification was performed primarily using individual feature sets and then all features combined. The results demonstrated that the SVM classifier gave a higher precision rate in classification of textures and required much less time for training the model [89].

In a study by Yu-Len *et al.* [90] SVM was used to classify benign and malignant breast tumours on ultrasound images. The proposed computer assisted diagnostic system (CAD) using SVM performed with high specificity and sensitivity in differentiating tumours using ultrasound images.

In another study by Pulido *et al.* [91] an SVM classifier is used for classifying weeds and vegetable crop images. The SVM classifier used a Radial Basis Function (RBF) kernel. The features used for classification were extracted from co-occurrence matrices and principal component analysis (PCA) was performed to create principal components with the largest variance in data. The classification performance was over 90 percent [91]. This study showed the effectiveness of using dimensionality reduction to enrich the feature space before using the SVM classifier. A similar approach is taken in the work in this section to classify peripheral nerves.

Another study by Kumari *et al.* [92] used similar methods as above to classify brain anomalies from MRI images. In this study, T2-weighted MRI brain images were used for feature extraction. PCA was used to select the most valuable features followed by SVM classification. An SVM classifier was trained using both linear and nonlinear kernels and the performance was assessed [92].

In a study by Soumya *et al.* [93]texture analysis was performed and SVM classification using non-linear kernels was effectively implemented for classification of tissue for staging cervical cancer in MRI images. This was performed using both T1- weighted and T2-weighted MRI images. The SVM classifier was successful in staging the cervical cancer with high accuracy [93].

6.7 Analysis of Classification Models

6.7.1 SVM using Shape Metrics

SVM classification was performed on the shape measures that demonstrated the morphological changes in the nerves in patients as compared to that in controls. SVM classification was first performed using the linear kernel and the accuracy was analysed. Then. SVM using a radial basis function (RBF) kernel and polynomial kernel function was performed. It was observed that using the RBF kernel reduced the measures of sensitivity and specificity. The outcome using the polynomial kernel was similar to that using the linear kernel and the accuracy remained unchanged. Also, the results below were derived only from a single iteration of the classification model. Multiple iterations of the algorithm and testing with cross validation methods might improve the performance which can be tested in further work with a larger dataset. The results of the SVM classification are summarised in Table 6.1 below.

SVM Classification without Bootstrapping					
Classification Kernel	**Sensitivity TPR**	**Specificity TNR**	**PPV**	**NPV**	**Total Accuracy**
SVM (Linear Kernel Function)	100%	100%	100%	100%	100%
SVM (Gaussian or RBF Kernel)	85%	100%	100%	88.80%	93.75%
SVM (Polynomial Kernel Function	100%	100%	100%	100%	100%

Table 6.1: SVM Results using shape measures

As the overall dataset is very small, bootstrapping resampling was used to create 1000 samples. Of these, 500 samples were used for training using an SVM classifier and 500 samples were used for testing. This was done to analyse the robustness of the classifier on a larger dataset. Bootstrapping was done by calculating the correlation co-efficient between shape measures and resampling was done using these correlation measures. When SVM classification was performed using the resampled data the overall accuracy of the classification reduced to 78 percent. The sensitivity and specificity scores were also affected. This could be attributed to the correlation scores between the metrics as although correlation is an effective measure to assess the linearity between variables, it was unclear if the variables correlated positively or negatively with each other and this would have affected the training set. Bootstrapping is an effective way of resampling, but it did not improve the accuracy with our dataset as the number of subjects in the dataset was too small to be resampled.

6.7.2 Principal Component Analysis of Texture Measures

As seen earlier, texture features were extracted from co-occurrence matrices and run length matrices for each subject. As 23 features were extracted per subjects, the dimensionality of the data was increased. When SVM was used directly on the high dimensionality data to classify the nerves, the overall accuracy was 70 percent. The specificity value was 100 percent, so all the normal nerves were classified as normal. However, the sensitivity was very low at 33 percent, so the classifier was unable to classify patient nerves accurately. Hence, to reduce the dimensionality and extract the features that preserved maximum variance in the data, principal component analysis was performed. The principal components were extracted from the data using an algorithm provided in MATLAB [44].

The first three principal components demonstrated the maximum variance in data and therefore were used. The scatter plot showing the result of PCA is shown below in Figure 6.1.

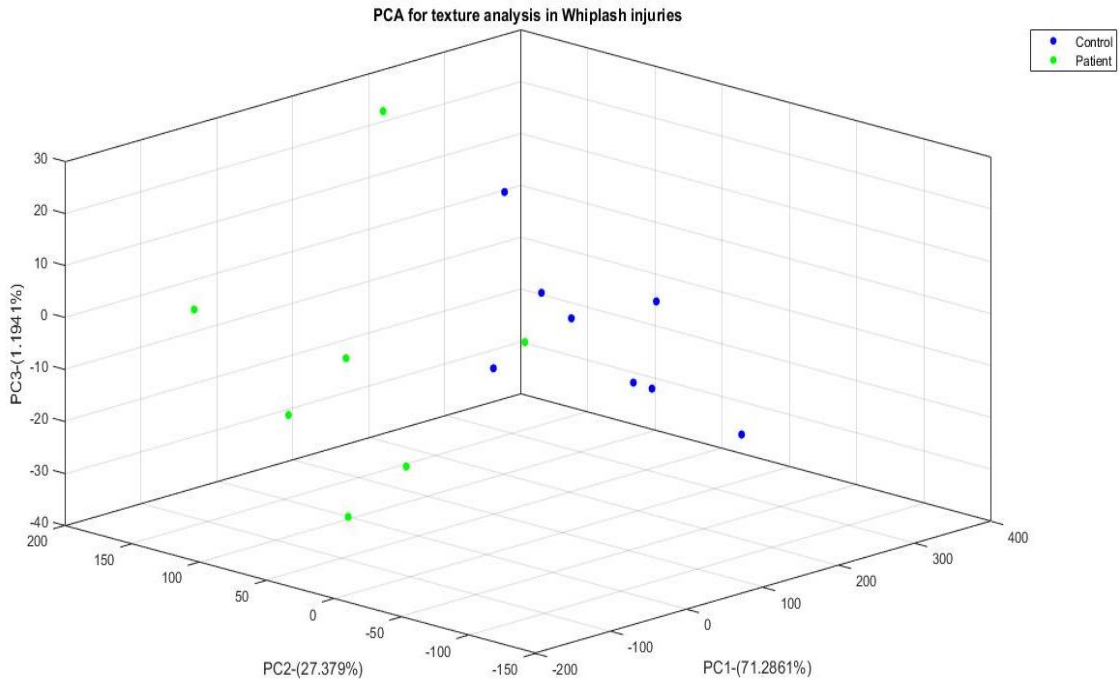

Figure 6.1 PCA plot using texture features

As can be observed from Figure 6.1, the first principal component extracted the features with maximum variance of 71 percent. The second principal component accounted for 27 percent of the variance in the internal structure of the data and the third component was 1.194 percent. Therefore, it can be deduced that the first component acquired from PCA was the most accurate at classifying data with only one outlier. As seen in the figure, the first component alone was able to classify all but one patient accurately.

6.8 Conclusion

Support Vector Machine and Principal Component Analysis are effective ways of classifying data. In this section, we used SVM to classify the nerves as normal or belonging to patients suffering from whiplash associated disorders. This classification was performed using the morphological features of the nerve extracted as described in earlier chapters. The accuracy rates and the sensitivity and specificity measures of the classification demonstrate that SVM can be reliably used to classify peripheral nerves as normal or as damaged in this study. However, bootstrapping resampling used to increase the dataset reduced the overall accuracy of the results due to the initial small size of dataset.

PCA was used to find the maximum variance in the high dimensional texture features extracted from the MRI image data. It can be seen from the analysis in the Section 6.7.2, that PCA can be used to reduce the dimensionality and thereby create a feature space of principal components which segregate the data more effectively.

Chapter 7

Conclusions and Future Work

7.1 Overview

Whiplash injuries are the most common occurring injury in a rear end motor vehicle collision. When the accident happens, the impact of the collision can cause severe trauma to the cervical spine of the people involved. These injuries are regarded as whiplash due to the stretch they cause in the neck when the collision occurs, like a whiplash. Also important, are the economic burden that whiplash injuries have on society and the overall effects of whiplash on the wellbeing of the patient.

As the diagnosis of whiplash associated disorders lies solely on the judgment of a clinician and the patients' description of the pain, there is an inherent aspect of human error or misconception involved which could lead to poor treatment, slow recovery or both.

This brings us to the problem that is addressed in this thesis. Seeing the nature of the injury and the differences in judgment of different clinicians in judging and treating pain in Whiplash Associated Disorder patients, there is a pressing need for a supportive tool that would help in characterising nerves without having any a priori knowledge, purely based on the medical images.

Thus, the work in this thesis attempted to use quantitative measures to characterise the peripheral nerves involved in a whiplash injury.

7.2 Proving the hypothesis

The hypothesis stated in this thesis is that quantitative image analysis of the peripheral nerves involved in whiplash injuries might help identify imaging biomarkers that could be used to assess the injury in cases where no clinical manifestation of injury exists.

Therefore, in order to prove the hypothesis, an attempt was made to characterise the nerves in a case-controlled study of 22 subjects where 15 were normal subjects and 7 were patients who had suffered from a whiplash injury. To study the nerve segments on MRI images, clinicians selected the area of the brachial plexus and the median nerve in the carpal tunnel of the subjects. As seen in Chapter 2, for each subject, three locations in the carpal tunnel were chosen, namely: proximal carpal row; distal carpal row; and radioulnar joint.

In this thesis, we used texture and shape analysis to find cues to the underlying pathology of the nerves in patients with whiplash. Texture analysis was used to extract features that described the surface pattern of the nerves as seen on T2- weighted MRI images. The texture analysis methods used were: first order features; co-occurrence matrices; run length matrices; and the autocorrelation function. The results of texture analysis demonstrated that the texture measures could be reliably used to build classification models that would enable effective differentiation and detection of the patient nerves.

In addition to texture analysis, shape analysis was performed in the fourth chapter to study the morphology of the median nerve in the carpal tunnel of the subjects. Shape measures such as eccentricity, circularity and aspect ratio were used to extract quantitative values that demonstrated the differences between controls and patient nerves. The statistical significance of the shape measures was $P<0.05$ which proved that differences in shape

existed in the nerves of patients and this quantitative assessment could help classify the median nerve as belonging to a normal subject or patient.

One of the major limitations on the work reported in this thesis was the size of the dataset available. The data was small, comprising of 22 subjects of which 15 were normal and 7 were patients. It was thus a preliminary study to quantitatively analyse nerves in controls and patients. Although from a pilot study point of view, the data can be considered as sufficient, from the supportive tool design aspect, it cannot be considered entirely conclusive. This was a case-controlled study used to compare patients who had WAD symptoms to those who did not have any symptoms and were considered as normal subjects.

It was seen that SVM and PCA demonstrated good accuracy in differentiating the patient nerves from control subjects despite the small sample size. The Bootstrapping method did not work as expected in creating resampled data. Overall, the classification model designed was successful at classifying the nerves. However, the robustness of the models need to be tested on a larger dataset.

The second most important limitation of the study was the quality of the images. As the images were acquired from a 1.5 Tesla MRI, the 16- bit DICOM images obtained were noisy. To accurately locate the median nerve in the carpal tunnel, an advanced correlation filter known as the OT-MACH was implemented. The results of using this filter are presented in Chapter 5. The filter was trained to handle most of the in-class variation present in the image data. It was observed that with a suitable combination of non-negative parameters, the filter could be adequately trained and was successful at generating a correlation peak at the location of the nerve inside the carpal tunnel.

7.3 Future Research

In the future, the imaging peripheral nerves will exploit Magnetic Resonance Neurography. As seen briefly in section 1.8 of the first chapter, magnetic resonance neurography could greatly improve the acquisition process of the images and thereby improve the quality of the images acquired for medical image analysis.

The work reported in this thesis has demonstrated the utility of medical image analysis for the quantitative study of peripheral nerves specific to a whiplash injury. To the best of our knowledge, this has not been previously. A computer-assisted diagnostic tool to automatically perform the texture and shape analysis can be developed. The tool developed can be specifically used to detect and quantify nerve segments presented in the medical imagery. This would not only improve the diagnosis and treatment of patients suffering from whiplash, but also could be extended to analysing peripheral neuropathies in the lower extremities such as from diabetes and sciatica nerve disorders.

Also, with the ongoing research and development of deep learning algorithms, specific models could be trained to automatically extract the images of the proximal, distal and radioulnar carpal row in the wrist of subjects. In recent years, medical image analysis has seen vast improvement in the ability to detect and classify patterns in medical imagery. The advances in the parallel processing capabilities of computers and the implementation of complex machine learning algorithms, which are called deep learning algorithms, has completely changed the face of object recognition and classification. The framework of deep convolution layers that extract features dynamically, instead of using handcrafted features, has alllowedmore information extraction at each layer. This advance will reduce time taken by clinicians to go through multiple MRI slices to select the appropriate locations.

References

[1] M. A. Haidekker, *Advanced Biomedical Image Analysis,* Wiley, 2011.

[2] B. V. Dasarathy and A. P. James, "Medical Image Fusion: A survey of state of the art," *Information Fusion,* vol. 19, pp. 4-19, 2013.

[3] "Medical Imaging for improved patient care," *European Science Foundation,* September 2007.

[4] H. Grant, "Reducing the number of whiplash claims: A Consulation on arrangements concerning whiplash injuries in England and Wales," The Stationery Office Limited, 2012.

[5] [Online]Available:http://www.cityoflondon.police.uk/CityPolice/Departments/ECD/IFED/. "www.cityoflondon.police.uk,"[Accessed 13/04/2017]

[6] R. Ferrari, The Whiplash Encyclopedia: The Facts and Myths of Whiplash, Jones and Bartlett Publishers.

[7] A. Cesarani, D. Alpini, R. Boniver, C. F. Claussen, P. M. Gagey, L. Magnusson and L. M. Odkvist, Whiplash Injuries Diagnosis and Treatments, Springer, 1996.

[8] [Online]. Available: http://www.chiropractic-in-malaysia.com/2016/01/whiplash-injury.html. [Accessed 17 08 2016].

[9] M. Sterling and J. Kenardy, "Physical and psychological aspects of whiplash: Important considerations for primary care assessment," *Manual Therapy,* vol. 13, pp. 93-102, 2008.

[10] S. D. Daffner, A. S. Hilibrand, B. S. Hanscom, B. T. Brislin, A. R. Vaccaro and T. J. Albert, "Impact of Neck and Arm Pain on Overall Health Status," *SPINE,* vol. 28, no. 17, pp. 2030-2035, 2003.

[11] G. Stoll, E. Wilder-Smith and M. Bendszus, "Chapter 8- Imaging of the peripheral nervous system," *Handbook of Clinical Meurology,* vol. 115, pp. 137-153, 2013.

[12] "www.corewalking.com," [Online]. Available: https://corewalking.com/wrist-carpal-tunnel/. [Accessed 08 04 2017].

[13] "emedmd.com," [Online]. Available: http://www.emedmd.com/content/diseases-peripheral-nerves. [Accessed 12 04 2017].

[14] G. Stoll, M. Bendszuz, J. Perez and M. Pham, "Magnetic resonance imaging of the peripheral nervous system," *Journal of Neurology,* vol. 256, pp. 1043-1051, 2009.

[15] A. G. Filler, F. A. Howe, C. E. Hayes, M. Kliot, H. R. Winn, B. A. Bell, J. R. Griffiths and J. S. Tsuruda, "Magnetic resonance neurography," *The Lancet,* vol. 341, pp. 659-661, 1993.

[16] W. Middleton, J. B. Kneeland, G. M. Kellman, J. D. Cates, J. R. Sanger, A. Jesmanowicz, W. Froncisz and J. S. Hyde, "MR Imaging of the Carpal Tunnel: Normal Anatomy and Preliminary Findings in the Carpal Tunnel Syndrome," *American Journal of Radiology,* vol. 148, pp. 307-316, 1987.

[17] C. Pierre-Jerome, S. Bekkelund, M. SI and R. Nordstrom, "Bilateral fast magnetic resonance imaging of the operated carpal tunnel," *Scandinavian Journal of Plastic and Reconstruction surgery and Hand Surgery,* vol. 31, pp. 171-177, 1997.

[18] T. Yoshikawa, N. Hayashi, S. Yamamoto, Y. Tajiri, N. Yoshioka, T. Masumoto, H. Mori, O. Abe, S. Aoki and K. Ohtomo, "Brachial Plexus Injury: Clinical Manifestations, Conventional Imaging Findings, and the Latest Imaging Techniques," *RadioGraphics,* vol. 26, pp. S133-S143, 2006.

[19] A. T. Dailey, J. S. Tsuruda, A. G. Filler, K. R. Maravilla, R. Goodkin and M. Kliot, "Magnetic resonance neurography of peripheral nerve degeneration and regeneration," *The Lancet,* vol. 350, pp. 1221-1222, 1997.

[20] A. Chhabra, G. Andreisek, T. Soldatos, K. C. Wang, A. J. Flammang, A. J. Belsberg and J. A. Carrino, "Mr Neurography: Past, Present, and Future," *American Journal of Radiology,* vol. 197, pp. 583-591, 2011.

[21] "Radiopaedia.org," [Online]. Available: https://radiopaedia.org/articles/short-tau-inversion-recovery. [Accessed 27/08/2017 August 2017].

[22] R2017a, *Mathworks Inc, Natick, MA, USA.*

[23] R. M. Haralick, K. Shanmugam and I. Dinstein, "Textural Features for Image Classification," *IEEE Transactions on Systems, Man and Cybernetics,* Vols. SMC-3, no. 6, pp. 610-621, 1973.

[24] A. Materka and M. Strzelecki, "Texture Analysis Methods-A Review," 1998.

[25] M. Levine, Vision in Man and Machine, McGraw Hill, 1985.

[26] W. Pratt, Digital Image Processing, Wiley, 1991.

[27] A. Papoulis, Probability, Random Variables and Stochastic Processes, McGraw Hill, 1965.

[28] M. Petrou and P. Garcia Sevilla, Dealing with Texture, London: John Wiley & Sons Ltd, 2006.

[29] A. Kassner and R. E. Thornhill, "Texture Analysis: A Review of Neurologic MR Imaging Applications," *American Journal of Neuroradiology,* vol. 31, no. 5, pp. 809-816, May 2010.

[30] E. Radulescu, B. Ganeshan, L. Minati, F. Beacher, M. A. Gray, C. Chatwin, R. Young, N. A. Harrison and H. D. Critchley, "Gray matter textural heterogeneity as

a potential in-vivo biomarker of fine structural abnormalities in Asperger syndrome," *The Pharmacogenomics Journal,* pp. 1-10, 2012.

[31] B. Ganeshan, K. Miles, R. Young and C. Chatwin, "Texture Analysis in non-contrast enhanced CT: Impact of malignancy on texture in apparently disease-free areas of liver," *Elsevier Journal of Radiology,* vol. 70, pp. 101-110, 2009.

[32] E. Orphanidou-Vlachou, N. Vlachos, N. P. Davies, T. N. Arvanitis, R. G. Grundy and A. C. Peet, "Texture analysis of T1- and T2- weighted MR images and use of probabilistic neural network to discriminate posterior fossa tumours in children," *NMR in Biomedicine,* vol. 27, pp. 632-639, 2014.

[33] N. Aggarwal and R. K. Agrawal, "First and second order statistics features for classification of magnetic resonance brain images," *Journal of Signal and Information Processing,* vol. 3, no. 2, pp. 146-153, 2012.

[34] X. Li, J. Li and M. Karmarkar, "Age-related differences in quantitative echo texture of the median nerve," *Journal of Ultrasound in Medicine,* vol. 34, no. 5, pp. 797-804, May 2015.

[35] M. R2017a, *The Mathworks Inc, Natick, MA.*

[36] M. M. Galloway, "Texture Analysis Using Gray Level Run Lengths," *Computer Graphics and Image Processing,* vol. 4, pp. 172-179, 1975.

[37] X. Tang, "Texture Information in Run Length Matrices," *IEEE,* vol. 7, no. 11, pp. 1602-1609, 1998.

[38] H. Yu, A.-S. Touret, B. Li, M. O'Brien, M. M. Qureshi, J. A. Soto, H. Jara and S. W. Anderson, "Application of Texture Analysis on Parametric T1 and T2 MAps for detection of hepatic fibrosis," *Journal of Magnetic Resonance Imaging,* vol. 45, pp. 250-259, 2016.

[39] S. H. Rezatofighi, A. Roodaki, R. A. Zoroofi, R. Sharifian and H. Soltanian-Zadeh, "Automatic Detection of Red Blood Cells in HEamatological Images using Polar Transformation and Run-length Matrix," *IEEE,* pp. 806-809, 2008.

[40] A. Mohammadi and A. Gharbali, "Diagnosis of Breast Tumours with Sonographic texture Analysis using Run-Length Matrix," *International Journal of Cancer Management,* 2017.

[41] N. Gupta, P. Bhatele and P. Khanna, "Identification of gliomas form the brain MRI through adaptive segmentation and run length of centralised patterns," *Journal of Computational Science,* vol. 619, 2017.

[42] L. A. Hunter, Y. P. Chen, L. Zhang, J. E. Matney, H. Choi, S. K. Kry, M. K. Martel, F. Stingo, Z. Liao, D. Gomez, J. Yang and L. E. Court, "NSCLC tumor shrinkage prediction using quantitative image features," *Computerised Medical Imaging and Graphics,* vol. 49, pp. 29-36, 2016.

[43] J. Cai, T.-X. Wu, K. Zhou and W. Li, "Recognition of osteoporosis based on texture analysis and a support vector machine," *International Journal of BioAutomation,* vol. 19, no. 1, pp. 107-118, 2015.

[44] M. R2017a, *The Mathworks Inc, Natick, MA.*

[45] G. N. Srinivasan and G. Shobha, "Statistical Texture Analysis," *Proceedings of World Academy of Science, Engineering and Technology,* vol. 36, pp. 2070-3740, 2008.

[46] L. Van Gool, P. Dewaele and A. Oosterlinck, "Texture Analysis Anno 1983," *Computer Vision, Graphics and Image Processing,* vol. 29, pp. 336-357, 1985.

[47] M. Unser and F. Ade, "Feature extraction and decision procedure for automkated inspection of textured materials," *Pattern Recognition Letters,* vol. 2, no. 3, pp. 185-191, 1984.

[48] E. Wood, "Applying fourier and associated transforms to pattern characterization in textiles," *Textile Research Journal,* vol. 60, pp. 212-220, 1990.

[49] M. A. Haidekkar, Advanced Biomedical Image Analysis, Singapore: John Wiley & Sons, 2011.

[50] D. Zhang, "Review of shape representation and description techniques," *Pattern Recognition,* pp. 1-19, 2004.

[51] Y. Yoshii, T. Ishii, W.-L. Tung, S. Sakai and A. C. Peter, "Median Nerve Deformation and Displace,ent in the Carpal Tunnel During Finger Motion," *Journal of Orthopaedic Research,* 2013.

[52] Y. Wang, A. Filius, C. Zhao, S. M. Passe, T. R. Andrew, K.-N. An and A. C. Peter, "Altered Median Nerve Deformation and Transverse Displacement during Wrist Movement in Patients with Carpal Tunnel Syndrome," *Elsevier,* pp. 472-480, 2014.

[53] A. Filius, M. Scheltens, H. G. Bosch, P. A. V. Doom, H. J. Stam, S. E. R. Hovious, P. C. Amadio and S. W. Ruud, "Multidimensional Ultrasound Imaging of the Wrist: Changes of shape and Displacement of the Median Nerve and Tendons in Carpal Tunnel Syndrome," *Journal of Orthopaedic Research,* pp. 13332-1340, 2015.

[54] N. Bhooshan, M. L. Giger, S. A. Jansen, H. Li, L. Lan and G. M. Newstead, "Cancer Breast Leasions on Dynamic Contrast -enhanced MR Images: Computerised Characterization for Image-based Prognostic Markers," *RSNA Radiology,* vol. 254, no. 3, pp. 680-690, 2010.

[55] S. C. Agner, S. Soman, E. Libfeld, M. McDonald, K. Thomas, S. Englander, M. A. Rosen, D. Chin, J. Nosher and A. Madabhushi, "Textural Kinetics: A Novel Dynamic Contrast-Enhanced (DCE)-MRI Feature for Breast Lesion Classification," *Journal of Digital Imaging,* vol. 24, no. 3, pp. 446-463, 2011.

[56] M. R2017a, *The Mathworks Inc, Natick, MA, 2008.*

[57] A. Mahalonobis, B. V. K. Kumar, S. Song, S. Sims and J. F. Epperson, "Unconstrained correlation filters," pp. 3751-3759, 1994.

[58] B. V. K. Kumar, A. Mahalanobis, S. Song and D. Casasent, "Minimum Squared Error Synthetic discriminant functions," *Optical Engineering.*

[59] A. Mahalanobis, B. V. K. Kumar and D. Casasent, "Minimum average correlation energy filters," *Applied Optics,* vol. 26, pp. 3633-3630, 1987.

[60] A. Mahalanobis and B. V. K. Kumar, "Optimality of the maximum average correlation height filter for detection of target in noise," *Optical Engineering,* vol. 36, no. 1, pp. 2642-2648, 1997.

[61] B. V. K. Kumar and L. Hasserbrook, "Performance measures for correlation filters," *Allied Optics,* vol. 29, pp. 2997-3006, 1990.

[62] M. Savvides and B. V. K. Kumar, "Efficient design of advanced correlation filters for robust distortion tolerant face recognition," *IEEE,* 2003.

[63] R. A. Kerekes and B. K. Kumar, "Selecting a composite correlation filter design: a survey and comparative study," *Optical Engineering ,* vol. 47, 2008.

[64] K. Venkataramani and B. Kumar, "Performance of composite correlation filters for fingerprint verification," *Optical Engineering,* vol. 43, pp. 1820-1827, 2004.

[65] Q. Han and Z. Yao, "An automatic pedestrian detection and tracking method: BAsed on MACH and particle filter," in *Network Computing and Information Security (NCIS),* Guilin, China, 2011.

[66] M. D. Rodriguez, J. Ahmed and M. Shah, "A spatio-temporal Maximum Average Correlation Height Filter for Action recognition," *Computer Vision and Pattern Recognition IEEE,* pp. 1-8, 2008.

[67] M. Alam and B. Sharif, "Trends in correlation -Based Pattern Recognition and Tracking in Forward- Looking Infrared Imagery," *SENSORS,* pp. 13437-13475, 2014.

[68] A. Alkandri, N. Bangalore, A. Gardezi, P. Birch, R. Young and C. Chatwin, "Human detection using OT-MACH filter in cluttered FLIR imagery," *IEEE,* 2013.

[69] N. M. Bangalore, R. Young, P. Birch and C. Chatwin, "Tracking of motor vehicles from aerial video iagery using the OT-MACH correlation filter," *Information Technologies and Security,* 2012.

[70] A. Gardezi, T. Umer, F. Butt, R. Young and C. R. Chatwin, "Vehicle monitoring under Vehicular Ad-Hoc Networks (VANET) parameters employing illumination

invariant correlation filters for the Pakistan motorway police," *Optical Pattern Recognition SPIE,* vol. XXVIII, 2016.

[71] N. H. Ruparel, N. M. Shahane and D. P. Bhamare, "Learning from Small Data set to Build Classification Model: A Survey," *Internationla Journal of Computer Applications,* vol. 0975, no. 8887, pp. 23-26, 2013.

[72] A. R. Webb and K. D. Copsey, "Rule and decision tree induction," in *Statistical Pattern Recognition*, Chichester, West Sussex, United Kingdom, John Wiley & Sons, Ltd, 2011, pp. 322-323.

`[73] A. R. Webb and K. D. Copsey, "Ensemble Methods-Classifier Combinaion Methods," in *Statistical Pattern Recognition*, Chichester, West Sussex, United Kingdom, John Wiley & Sons, Ltd, 2011, p. 389.

[74] T. K. Ho, "Random Decision Forests," in *Proceedings of the 3rd International Conference on Document Analysis and Recognition Pages 14-16,* Montreal, QC, August 1995.

[75] T. K. Ho, "The Random Subspace Method for Constructing Decision Forests," *IEEE Transactions on Pattern Analysis amd Machine Intelligence,* vol. 20, no. 8, pp. 832-844, 1998.

[76] A. R. Webb and K. D. Copsey, "Linear Discrimant Analysis- Support Vector Machines," in *Statistical Pattern Recognition*, Chichester, West Sussex, United Kingdom, John Wiley & Sons, Ltd, 2011, pp. 249-253.

[77] G. P. Zhang, "Neural Networks for Classification: A Survey," *IEEE Transactions on Systems,Man and Cybernetics,* vol. 30, no. 4, pp. 451-462, 2000.

[78] M. Lee Minsky and P. Seymour, Perceptrons: An Introduction to Computational Geometry, MIT Press, 1972.

[79] I. Goodfellow, Y. Bengio and A. Courville, Deep Learning, London, England: The MIT Press, 2017.

[80] C. Huang and C. Moraga, "A diffusion-neural-network for learning from small samples," *International Journal of Approximate Reasoning,* vol. 35, pp. 137-161, 2004.

[81] C. F. Huang and Y. Shi, "Towards Effecient Fuzzy Information Processing- Using the Principle of Information Diffusion," Physica-Verlag, Heidelberg, 2002.

[82] L. Der-Chiang, W. Chih-Sen, T. Tung-I and L. Yao-San, "Using mega-trend-diffusion and artificial samples in small data set learning for early flexible manufacturing system scheduling knowledge," *Computers and Operations Research,* vol. 34, pp. 966-982, 2007.

[83] L. Der-Chiang and L. Chiao-Wen, "Extending Attribute Information for Small Data Set Classification," *IEEE Transactions on Knowledge and Data Engineering,* vol. 24, no. 3, pp. 452-464, March 2012.

[84] "Bootstrap Methods for standard Errors, Confidence Intervals and other Measures of Statistical Accuracy," *Statistical Science,* vol. 1, no. 1, pp. 54-77, 1986.

[85] B. Efron and R. J. Tibshirani, "An Introduction to the bootstrap," *Monographs on Statistics and Applied Probability,* vol. 57, p. 436, 1993.

[86] K. Pearson, "On lines and planes of closest fit to systems of points in space," *Philosophical Magazine,* vol. 2, no. 11, 1901.

[87] A.-M. Simundic, "Measures of Diagnostic Accuracy: Basic Definitions," *The Journal of the International Federation of Clinical Chemistry and Laboratory Medicine,* vol. 19, no. 4, pp. 203-211, 2009.

[88] R. Parikh, A. Mathai and R. Thomas, "Understanding and using sensitivity, specificity and predictive values," *Indian Journal of Opthalmology,* vol. 56, no. 1, pp. 45-50, 2008.

[89] M. M. Al Sammarraie, M. J. Nordin and G. J. Al-Anizy, "Texture Classification using Random Forests and Support Vector Machines," *Journal of Theoretical and Applied Information Technology,* vol. 73, no. 2, pp. 232-238, 2015.

[90] H. Yu-Len, W. Kao-Lun and D.-R. Chen, "Diagnosis of breast tumours with ultrasonic texture analysis using support vector machines," *Neural Computing and Applications,* vol. 15, pp. 164-169, 2006.

[91] C. Pulido, L. Solaque and N. Velasco, "Weed recognition by SVM feature classification in outdoor vegetable crop images," *Ingeniera E Investigation,* vol. 37, no. 1, pp. 68-74, 2017.

[92] R. Kumari and R. K. Soni, "Classifying brain anomalies using PCA and SVM," *International Journal of Scientific Research and Management,* vol. 2, no. 5, pp. 935-939, 2014.

[93] M. K. Soumya, K. Sneha and C. Arunvinodh, "Cervical Cancer Detection and Classification Using Texture Analysis," *Biomedical and Pharmacology Journal,* vol. 9, no. 2, pp. 663-671, 2016.

Appendices

The Appendices for this thesis are divided into four parts.

The contents of each appendices are listed below

Appendix A: Results of First Order Features

Appendix B: Results of Run Length Matrices

Appendix C: Plots of the Autocorrelation Function

Appendix D: Results of Shape Metrics

Key Notes

The subjects are listed as patient or control using their unique ID.

Controls:

CISC816; CISC 10195; CISC10414; CISC10709; CISC10886; CISC11329; CISC11345; CISC11414; CISC14779; CISC14801; CISC14817; CISC14850; CISC14898

Patients:

CISC8577; CISC9424; CISC10283; CISC10405; CISC10903; CISC10927; CISC13565

Appendix A: Results of First Order Features

Part 1: Results of First Order Features of the Brachial Plexus

Table A.1: Mean Grey Level values in Brachial Plexus

CODE	Mean										
	LC5	LC6	LC7	LC8	L-Avg	RC5	RC6	RC7	RC8	R-Avg	L+R
816	3.9167	5.3519	5.8958	3.942	4.7766	4.3583	4.7282	4.1797	4.7762	4.5106	9.2872
10195	0	4.9286	4.0769	4.1818	3.296825	0	3.5231	4.9514	4.5385	3.25325	6.550075
10414	4.4467	4.1389	5.0341	0	3.404925	0	0	3.7857	4.8111	2.1492	5.554125
10709	4.3071	4.3485	4.7473	4.2611	4.416	4.4603	4.6434	3.683	4.05	4.209175	8.625175
10886	3.4242	4.4537	4.98	0	3.214475	3.7692	4.5133	3.8667	4.1375	4.071675	7.28615
11329	4.9074	4.7692	4.2208	3.9152	4.45315	4.7733	4.7963	3.9286	4.0556	4.38845	8.8416
11345	4.6667	4.2875	4.9929	0	3.486775	4.103	3.8636	3.6543	0	2.905225	6.392
11417	4.6068	3.8977	4.3	3.746	4.137625	4.3651	3.1616	3.9545	3.6591	3.785075	7.9227
14779	3.3712	4.3308	4.6084	0	3.0776	4.5152	4.7813	4.02	5.1481	4.61615	7.69375
14801	4.2182	5.0833	5.1875	4.0417	4.632675	4.6771	3.8125	4.8929	4.7818	4.541075	9.17375
14817	3.5556	4.0256	4.2479	3.7385	3.8919	0	3.8571	4.5364	4.6061	3.2499	7.1418
14850	4	4.287	3.9583	4.6154	4.215175	4.3333	3.1714	3.6133	4.6204	3.9346	8.149775
14898	4.1354	4.7077	3.9931	5.8632	4.67485	4.1319	4.2821	5.4727	4.4685	4.5888	9.26365
Mean	3.812	4.508492	4.634077	2.946531	3.975275	3.345131	3.779531	4.195323	4.127146	3.8617827	7.837058
Std Dev	1.191888	0.413875	0.5498	2.031848	0.587434	1.84834	1.227601	0.56406	1.252136	0.7351599	1.157713
SEM	0.344068	0.119475	0.158714	0.586544	0.169578	0.53357	0.354378	0.16283	0.361461	0.2122224	0.334203
	LC5	LC6	LC7	LC8	L-Avg	RC5	RC6	RC7	RC8	R-Avg	L+R
8577	4.1368	3.8042	3.9056	4.3889	4.058875	4.4394	4.5337	4.4722	4.4429	4.47205	8.530925
9424	4.1339	3.719	4.6256	4.2136	4.173025	4.3359	3.6923	4.3462	4.2153	4.147425	8.32045
10283	0	3.9141	4.7366	4.0338	3.171125	0	3.7193	4.6013	3.6863	3.001725	6.17285
10405	3.9091	3.8563	4.1278	3.9286	3.95545	4.2074	3.9911	4.5989	4.8256	4.40575	8.3612
10452	3.9333	4.25	4.2105	5.2941	4.421975	3.6429	4.5641	4.78	3.8392	4.20655	8.628525
10903	0	4.8035	5.5667	4.8854	3.8139	3.1026	4.4978	4.4808	3.381	3.86555	7.67945
10904	3.62	3.7867	4.6061	4.2244	4.0593	4.303	4.6044	5.4611	4.1834	4.637975	8.697275
10927	4.7083	4.3212	4.8083	4.2444	4.52055	4.4071	3.9295	3.6667	3.7976	3.950225	8.470775
13565	4.6643	4.6513	4.6875	4.254	4.564275	3.716	3.7933	3.7863	4.4762	3.94295	8.507225
mean	3.233967	4.122922	4.586078	4.385244	4.082053	3.5727	4.147278	4.465944	4.094167	4.0700222	8.152075
sdev	1.759276	0.378639	0.45461	0.408333	0.40379	1.332362	0.37151	0.498918	0.428579	0.4515538	0.753382
SEM	0.621998	0.133869	0.160729	0.144367	0.142761	0.471061	0.131349	0.176394	0.151525	0.1596484	0.266361
T-test	0.430925	0.045385	0.833973	0.03265	0.635254	0.752509	0.345868	0.274028	0.933994	0.4422082	0.469615

Table A.2: Variance in Grey Level values in Brachial Plexus

CODE	Variance										
	LC5	LC6	LC7	LC8	L-Avg	RC5	RC6	RC7	RC8	R-Avg	Kurt L+R
816	3.6042	3.4503	3.135	3.51	3.424875	3.2466	4.1261	4.6161	4.3166	4.07635	7.501225
10195	0	3.3235	3.6949	3.4215	2.609975	0	3.311	3.9212	4.1716	2.85095	5.460925
10414	3.9138	4.4529	2.4193	0	2.6965	0	0	4.0096	4.4865	2.124025	4.820525
10709	3.6699	4.4543	4.079	3.9818	4.04625	5.3754	2.9148	2.1629	4.3586	3.702925	7.749175
10886	2.1635	4.9701	3.7596	0	2.7233	2.2391	3.9432	2.8489	3.7186	3.18745	5.91075
11329	4.1951	3.7801	4.6396	3.3625	3.994325	4.2686	4.1067	3.3806	3.608	3.840975	7.8353
11345	3.4815	3.3048	3.4928	0	2.569775	2.6985	2.8147	4.6706	0	2.54595	5.115725
11417	5.0249	4.6145	4.5373	5.1101	4.8217	3.0572	2.6203	3.8616	3.0732	3.153075	7.974775
14779	2.3849	3.9906	2.9935	0	2.34225	3.4417	5.5042	2.0729	3.7855	3.701075	6.043325
14801	4.0615	3.5264	3.9023	4.9149	4.101275	2.9895	2.2982	2.4766	5.2433	3.2519	7.353175
14817	4.1102	3.8028	3.4096	4.547	3.9674	0	1.8163	3.176	4.7084	2.425175	6.392575
14850	5.2292	3.8898	3.4399	3.6323	4.0478	4.5926	2.0468	3.2905	2.6059	3.13395	7.18175
14898	4.0129	3.2992	2.1597	1.9642	2.859	4.2463	5.4845	3.7402	4.6966	4.5419	7.4009
Mean	3.527046	3.912254	3.5125	2.649562	3.40034	2.781192	3.152831	3.402131	3.751754	3.271977	6.672317
Std Dev	1.307693	0.532638	0.698407	1.919973	0.769808	1.724223	1.457273	0.812208	1.280265	0.664096	1.056956
SEM	0.377498	0.153759	0.201613	0.554249	0.222224	0.49774	0.420678	0.234464	0.369581	0.191708	0.305117
	LC5	LC6	LC7	LC8	L-Avg	RC5	RC6	RC7	RC8	R-Avg	Kurt L+R
8577	5.1437	5.3043	4.3633	4.7469	4.88955	4.2463	4.4027	3.9492	4.0182	4.1541	9.04365
9424	4.5446	3.8715	3.0445	4.668	4.03215	4.6137	3.4822	2.7359	4.4884	3.83005	7.8622
10283	0	3.2426	2.2208	3.5214	2.2462	0	2.8545	2.9391	3.2741	2.266925	4.513125
10405	3.2705	3.1856	3.3337	5.1735	3.740825	3.7199	4.1155	4.0094	4.7901	4.158725	7.89955
10452	3.0289	3.3413	1.9482	1.9723	2.572675	3.6724	4.951	3.6183	2.1741	3.60395	6.176625
10903	0	2.8386	4.0456	4.789	2.9183	1.4986	4.1522	4.1727	3.1088	3.233075	6.151375
10904	3.9023	2.8878	3.7691	2.674	3.3083	3.0698	3.5138	2.7707	2.565	2.979825	6.288125
10927	4.8066	2.9453	3.6049	2.2569	3.403425	4.2271	4.1425	2.8	3.5781	3.686925	7.09035
13565	3.7055	4.4733	2.4456	2.1704	3.1987	3.2404	4.1506	2.8176	3.5161	3.431175	6.629875
mean	3.155789	3.565589	3.1973	3.552489	3.367792	3.143133	3.973889	3.312544	3.501433	3.48275	6.850542
sdev	1.807776	0.789678	0.795339	1.233155	0.746986	1.404988	0.573159	0.577113	0.799477	0.565765	1.2366
SEM	0.639145	0.279193	0.281195	0.435986	0.2641	0.496738	0.202642	0.20404	0.282658	0.200028	0.437204
T-test	0.62505	0.296808	0.376177	0.215066	0.925941	0.61263	0.096827	0.776148	0.596537	0.456223	0.742708

Table A.3: Skewness values in Brachial Plexus

CODE	Skewness										
	LC5	LC6	LC7	LC8	L-Avg	RC5	RC6	RC7	RC8	R-Avg	Skew L+R
816	0.6737	0.30351	0.4051	0.6829	0.516303	0.0594	0.1621	0.4141	0.1593	0.198725	0.715028
10195	0	0.1488	0.5405	0.4655	0.2887	0	0.6868	0.1533	0.1139	0.2385	0.5272
10414	0.4175	0.5159	0.5278	0	0.3653	0	0	0.6129	0.2413	0.21355	0.57885
10709	0.5644	0.4365	0.4988	0.6407	0.5351	0.3199	0.3871	1.4327	0.6516	0.697825	1.232925
10886	0.9391	0.6354	0.013	0	0.396875	0.7143	0.274	0.7005	0.537	0.55645	0.953325
11329	0.1919	0.3316	0.6219	0.6736	0.45475	0.0644	0.1513	0.7739	0.2559	0.311375	0.766125
11345	0.5816	0.2311	0.1811	0	0.24845	0.5403	0.562	0.9707	0	0.51825	0.7667
11417	0.3601	1.0062	0.4241	0.7617	0.638025	0.6978	1.295	0.8336	1.2615	1.021975	1.66
14779	1.6366	0.2987	1.4044	0	0.834925	0.2609	0.0119	0.4609	0.3947	0.2821	1.117025
14801	0.6069	0.2641	0.032	0.5096	0.35315	0.3834	1.1712	0.0579	0.2595	0.468	0.82115
14817	1.058	0.5656	0.0595	0.7284	0.602875	0	0.711	0.1476	0.1695	0.257025	0.8599
14850	0.4861	0.334	0.5076	0.519	0.461675	0.143	1.1999	1.0334	0.549	0.731325	1.193
14898	0.529	0.392	0.524	0.9296	0.59365	0.4934	0.5772	0.5091	0.1994	0.444775	1.038425
Mean	0.618838	0.420262	0.441523	0.454692	0.483829	0.282831	0.553038	0.623123	0.368662	0.456913	0.940743
Std Dev	0.395861	0.214568	0.346198	0.323865	0.154537	0.253912	0.43082	0.378968	0.315322	0.23727	0.296345
SEM	0.114275	0.06194	0.099939	0.093492	0.044611	0.073298	0.124367	0.109399	0.091026	0.068494	0.085547
	LC5	LC6	LC7	LC8	L-Avg	RC5	RC6	RC7	RC8	R-Avg	Skew L+R
8577	0.7098	0.4766	0.5569	0.4633	0.55165	0.3878	0.4337	0.4976	0.4491	0.44205	0.9937
9424	0.6545	1.0194	0.3572	0.6781	0.6773	0.54	0.9445	0.351	0.4529	0.5721	1.2494
10283	0	0.55	0.2457	0.4153	0.30275	0	0.6369	0.4871	0.5965	0.430125	0.732875
10405	0.6766	0.5598	0.3802	0.5616	0.54455	0.3617	0.7423	0.3167	0.1264	0.386775	0.931325
10452	0.6145	0.2704	0.0777	0.1143	0.269225	1.0203	0.1158	0.2817	1.6802	0.7745	1.043725
10903	0	0.0462	0.3309	0.2712	0.162075	1.4332	0.3987	0.4609	0.6275	0.730075	0.89215
10904	0.8566	0.3759	0.2278	0.2264	0.421675	0.3211	0.167	0.0427	0.4173	0.237025	0.6587
10927	0.2314	0.3228	0.1005	0.3121	0.2417	0.5693	0.9304	1.6395	0.3451	0.871075	1.112775
13565	0.0304	0.1956	0.1637	0.2601	0.16245	0.911	0.56	0.7183	0.3037	0.62325	0.7857
mean	0.419311	0.424078	0.271178	0.366933	0.370375	0.616044	0.5477	0.532833	0.555411	0.562997	0.933372
sdev	0.328874	0.263024	0.143425	0.167831	0.175757	0.409528	0.282165	0.428264	0.422237	0.194613	0.178584
SEM	0.116274	0.092993	0.050708	0.059337	0.06214	0.14479	0.09976	0.151414	0.149283	0.068806	0.063139
T-test	0.235913	0.973217	0.146613	0.437838	0.157944	0.062329	0.973621	0.635527	0.303834	0.288081	0.945431

Table A.4: Kurtosis values in Brachial Plexus

CODE	Kurtosis										
	LC5	LC6	LC7	LC8	L-Avg	RC5	RC6	RC7	RC8	R-Avg	Kurt L+R
816	2.7263	2.1523	2.8579	2.7686	2.626275	2.4202	1.921	2.0878	2.0733	2.125575	4.75185
10195	0	2.3485	2.3535	2.7099	1.852975	0	2.8405	1.8708	2.0947	1.7015	3.554475
10414	2.2308	2.0978	3.4857	0	1.953575	0	0	2.451	2.0647	1.128925	3.0825
10709	2.341	1.9956	2.1243	2.4366	2.224375	1.8634	2.8575	5.6063	2.2412	3.1421	5.366475
10886	4.4272	2.3299	2.1581	0	2.2288	4.1241	2.072	2.9323	2.3646	2.87325	5.10205
11329	2.0544	2.4028	2.2128	2.6419	2.327975	1.9448	2.0183	2.695	2.173	2.207775	4.53575
11345	2.6951	2.4716	1.9752	0	1.785475	2.8096	3.4611	3.1517	0	2.3556	4.141075
11417	2.0351	2.707	2.002	2.5653	2.32735	3.0208	4.2041	2.8099	3.9495	3.496075	5.823425
14779	5.9041	2.2999	2.7484	0	2.7381	2.3687	1.7446	3.267	2.4182	2.449625	5.187725
14801	2.3098	2.032	2.0388	1.8707	2.062825	2.4922	4.5148	2.6645	1.8875	2.88975	4.952575
14817	3.1141	2.4096	2.2567	2.6823	2.615675	0	4.0569	2.3179	1.9356	2.0776	4.693275
14850	2.1066	2.1128	2.7081	2.7141	2.4104	1.9901	4.9654	3.3402	3.2045	3.37505	5.78545
14898	2.098	2.4934	3.4565	5.5436	3.397875	2.4624	1.9541	2.3765	1.9401	2.183275	5.58115
Mean	2.618654	2.2964	2.490615	1.994846	2.350129	1.961254	2.816177	2.890069	2.180531	2.462008	4.812137
Std Dev	1.321431	0.200074	0.501978	1.55825	0.414732	1.20831	1.335966	0.892475	0.844099	0.649721	0.795728
SEM	0.381464	0.057756	0.144909	0.449828	0.119723	0.348809	0.38566	0.257635	0.24367	0.187558	0.229707
	LC5	LC6	LC7	LC8	L-Avg	RC5	RC6	RC7	RC8	R-Avg	Kurt L+R
8577	2.3668	1.946	2.097	1.9676	2.09435	1.9631	2.1763	2.4789	1.9083	2.13165	4.226
9424	2.388	3.2639	2.3835	2.6153	2.662675	2.2429	3.3185	2.6207	2.1796	2.590425	5.2531
10283	0	2.6518	2.7959	2.3768	1.956125	0	2.8388	2.6135	2.5828	2.008775	3.9649
10405	2.7936	2.5563	2.5411	2.1236	2.50365	2.2437	2.5889	2.137	1.9849	2.238625	4.742275
10452	2.5088	2.4007	3.277	3.096	2.820625	3.3177	1.826	2.0409	5.5171	3.175425	5.99605
10903	0	2.6105	2.0461	2.1419	1.699625	6.5298	2.2416	2.1543	2.3304	3.314025	5.01365
10904	2.929	2.5657	2.1194	2.5424	2.539125	2.4155	2.0862	2.5223	2.6747	2.424675	4.9638
10927	1.8732	2.4386	2.2603	2.8603	2.3581	2.3883	2.8693	3.6555	2.225	2.784525	5.142625
13565	2.3531	1.9662	2.5528	2.6876	2.389925	3.3515	2.1037	3.1223	2.2608	2.709575	5.0995
mean	1.9125	2.488856	2.452567	2.490167	2.336022	2.716944	2.449922	2.593933	2.629289	2.597522	4.933544
sdev	1.059804	0.369783	0.374141	0.350077	0.336982	1.629555	0.454674	0.48688	1.047193	0.423906	0.556287
SEM	0.374697	0.130738	0.132279	0.123771	0.119141	0.576135	0.160752	0.172138	0.370239	0.149873	0.196677
T-test	0.202045	0.20488	0.848216	0.306652	0.934302	0.281111	0.393834	0.351007	0.327792	0.578729	0.692335

Table A.5: Energy values in Brachial Plexus

CODE	Energy										
	LC5	LC6	LC7	LC8	L-Avg	RC5	RC6	RC7	RC8	R-Avg	Energy L+R
816	0.1644	0.1562	0.1637	0.1718	0.164025	0.1518	0.1469	0.1402	0.1314	0.142575	0.3066
10195	0.1608	0.165	0.1722	0	0.1245	0	2.8405	1.8708	2.0947	1.7015	1.826
10414	0.1486	0.1603	0.2379	0	0.1367	0	0	0.1553	0.1389	0.07355	0.21025
10709	0.1699	0.1498	0.1654	0.1761	0.1653	0.1321	0.1771	0.2421	0.1736	0.181225	0.346525
10886	0.2109	0.1559	0.142	0	0.1272	0.2031	0.1572	0.1897	0.1575	0.176875	0.304075
11329	0.1351	0.1515	0.1577	0.1899	0.15855	0.134	0.1382	0.1859	0.146	0.151025	0.309575
11345	0.1678	0.1566	0.1585	0	0.120725	0.1815	0.1746	0.1742	0	0.132575	0.2533
11417	0.1349	0.2082	0.1453	0.159	0.16185	0.1822	0.2856	0.1741	0.2259	0.21695	0.3788
14779	0.261	0.1451	0.1645	0	0.14265	2.3687	1.7446	3.267	2.4182	2.449625	2.592275
14801	0.174	0.1574	0.1488	0.1701	0.162575	0.1847	0.2352	0.1882	0.1307	0.1847	0.347275
14817	0.2283	0.165	0.1583	0.1524	0.176	0	0.2189	0.156	0.1375	0.1281	0.3041
14850	0.1437	0.1559	0.1553	0.1627	0.1544	0.1361	0.2381	0.2051	0.1987	0.1945	0.3489
14898	0.1704	0.1575	0.2011	0.252	0.19525	0.1429	0.1647	0.1512	0.1311	0.147475	0.342725
Mean	0.1746	0.160338	0.166977	0.110308	0.153056	0.293623	0.501662	0.546138	0.468015	0.45236	0.605415
Std Dev	0.035964	0.014788	0.024861	0.090223	0.020906	0.603123	0.795966	0.905283	0.766835	0.708357	0.701417
SEM	0.010382	0.004269	0.007177	0.026045	0.006035	0.174107	0.229775	0.261333	0.221366	0.204485	0.202482
	LC5	LC6	LC7	LC8	L-Avg	RC5	RC6	RC7	RC8	R-Avg	Energy L+R
8577	0.1533	0.1497	0.1657	0.1535	0.15555	0.1527	0.14	0.1495	0.1706	0.1532	0.30875
9424	0.1563	0.189	0.165	0.1522	0.165625	0.1522	0.1837	0.1681	0.1444	0.1621	0.327725
10283	0	0.1618	0.1892	0.1579	0.127225	0	0.1797	0.1745	0.1668	0.13025	0.257475
10405	0.169	0.1757	0.1573	0.1478	0.16245	0.1471	0.1686	0.1421	0.1302	0.147	0.30945
10452	0.1835	0.1543	0.2087	0.2053	0.18795	0.1926	0.1326	0.1495	0.3303	0.20125	0.3892
10903	0	0.1726	0.1499	0.1428	0.116325	0.2767	0.1411	0.1551	0.1965	0.19235	0.308675
10904	0.1801	0.1692	0.1452	0.1741	0.16715	0.1598	0.1499	0.1716	0.1807	0.1655	0.33265
10927	0.1333	0.1643	0.1446	0.1913	0.158375	0.1598	0.2	0.208	0.1484	0.17905	0.337425
13565	0.1432	0.1355	0.1815	0.1894	0.1624	0.1826	0.1764	0.188	0.1641	0.177775	0.340175
mean	0.1243	0.163567	0.167456	0.168256	0.155894	0.158167	0.163556	0.167378	0.181333	0.167608	0.323503
sdev	0.068167	0.014821	0.020573	0.021171	0.020353	0.06753	0.022083	0.019926	0.055885	0.021189	0.03314
SEM	0.024101	0.00524	0.007274	0.007485	0.007196	0.023875	0.007807	0.007045	0.019758	0.007492	0.011717
T-test	0.081614	0.638953	0.963126	0.050709	0.76603	0.455209	0.167067	0.172976	0.221008	0.189237	0.189622

Table A.6: Entropy values in Brachial Plexus

CODE	Entropy										
	LC5	LC6	LC7	LC8	L-Avg	RC5	RC6	RC7	RC8	R-Avg	Entropy L+R
816	1.9434	1.9541	1.9482	1.9303	1.944	1.9795	2.0132	2.0498	2.0882	2.032675	3.976675
10195	1.9604	1.9392	1.9403	0	1.459975	0	1.9232	1.9596	2.0749	1.489425	2.9494
10414	1.9962	1.9812	1.9762	0	1.4884	0	0	1.9901	2.0691	1.0148	2.5032
10709	1.9138	2.007	1.9579	1.9307	1.95235	2.102	1.8868	1.6133	1.932	1.883525	3.835875
10886	2.02	2.0216	2.0332	0	1.5187	1.8999	1.9564	1.8303	1.9635	1.912525	3.431225
11329	2.0603	2.0119	1.99	1.8826	1.9862	2.6608	2.0491	1.8691	1.9961	2.143775	4.129975
11345	1.9494	1.9597	1.941	0	1.462525	1.8387	1.8824	1.8993	0	1.4051	2.867625
11417	2.0908	1.7894	2.0193	1.9788	1.969575	1.8743	1.5907	1.915	1.7266	1.77665	3.746225
14779	2.0013	2.0374	1.9349	0	1.4934	1.9912	2.1228	1.9893	1.9917	2.02375	3.51715
14801	1.9368	1.9438	2.0008	1.9385	1.954975	1.8611	1.6952	1.8285	2.1076	1.8731	3.828075
14817	1.7952	1.9525	1.9548	2.0182	1.930175	0	2.0012	1.9325	2.069	1.500675	3.43085
14850	2.0648	1.9716	1.9698	1.971	1.9943	2.0676	1.9123	1.8151	1.8322	1.9068	3.9011
14898	1.919	1.9672	1.7419	1.6262	1.813575	2.0516	1.9753	1.9867	2.0844	2.0245	3.838075
Mean	1.973185	1.964354	1.954485	1.1751	1.766781	1.563592	1.769892	1.898354	1.841177	1.768254	3.535035
Std Dev	0.075656	0.058814	0.06823	0.933257	0.227302	0.87925	0.528605	0.107838	0.542264	0.310725	0.469931
SEM	0.02184	0.016978	0.019696	0.269408	0.065616	0.253818	0.152595	0.03113	0.156538	0.089699	0.135657
	LC5	LC6	LC7	LC8	L-Avg	RC5	RC6	RC7	RC8	R-Avg	Entropy L+R
8577	2.0129	2.0146	1.9525	2.002	1.9955	1.9933	2.0553	2.0249	1.9085	1.9955	3.991
9424	2.0032	1.8759	1.9103	2.0281	1.954375	0.0268	1.8907	1.8924	2.0355	1.46135	3.415725
10283	0	1.9415	1.8031	1.9606	1.4263	0	1.8562	1.8976	1.9188	1.41815	2.84445
10405	1.9195	1.8814	1.9694	2.0267	1.94925	2.0073	1.9565	2.038	2.0925	2.023575	3.972825
10452	1.8428	1.9668	1.7181	1.7436	1.817825	1.8654	2.0817	1.976	1.4593	1.8456	3.663425
10903	0	1.9107	2.0067	2.0639	1.495325	2.0814	2.0494	2.0041	2.0916	2.056625	3.55195
10904	1.9218	1.8806	2.018	1.8639	1.921075	1.9247	1.9817	1.8864	1.847	1.90995	3.831025
10927	2.083	1.9187	2.0209	1.8039	1.956625	2.0022	1.8811	1.7812	1.9744	1.909725	3.86635
13565	2.0346	2.0664	1.8311	1.7875	1.9299	1.8809	1.9227	1.8225	1.955	1.895275	3.825175
mean	1.535311	1.939622	1.914456	1.920022	1.827353	1.531333	1.963922	1.924789	1.920289	1.835083	3.662436
sdev	0.823418	0.062044	0.101625	0.114236	0.201785	0.813865	0.078474	0.085696	0.180873	0.220797	0.340418
SEM	0.291122	0.021936	0.03593	0.040389	0.071342	0.287745	0.027745	0.030298	0.063948	0.078064	0.120356
T-test	0.17162	0.385423	0.346759	0.017512	0.539678	0.933924	0.233334	0.549893	0.646326	0.580376	0.490512

Part 2: Results of First Order Features of the Median Nerve

Table A.7: First order Features of the Median Nerve in Controls

Controls	Mean	Variance	Skewness	Kurtosis	Energy	Entropy
816	4.2532	3.9683	0.7132	2.587	0.1739	1.9397
10195	3.7615	4.1508	0.6465	0.4415	0.1575	0.9838
10414	4.05	3.4475	0.591	2.4435	0.1653	1.9245
10709	3.75	5.5833	0.8302	2.2977	0.2072	1.8813
10886	3.5852	3.5041	0.8047	3.1311	0.1672	1.9286
11329	3.254	2.526	1.117	3.8489	0.2248	1.7089
11345	3.0694	3.3887	1.1715	3.5935	0.2379	1.7469
11417	3.8769	3.2772	0.4947	2.4417	0.1654	1.917
14779	2.6148	1.1405	1.6155	8.2642	0.3352	1.6783
14801	3.8034	2.6024	0.8947	3.493	0.1984	1.7948
14817	3.4266	2.4824	0.1663	1.8995	0.1411	2.043
14850	3.6333	2.5846	0.8141	3.4525	0.1922	1.8048
14898	2.4887	1.9115	1.453	5.942	0.2696	1.5263
mean	3.505154	3.120562	0.870185	3.372008	0.202746	1.759838
sd	0.505136	1.070389	0.376786	1.863582	0.051609	0.259735
SEM	0.14582	0.308995	0.108769	0.53797	0.014898	0.074979

Table A.8: First order Features of the Median Nerve in Patients

Patients	Mean	Variance	Skewness	Kurtosis	Energy	Entropy
8577	3.0031	4.0464	1.3285	3.774	0.2372	1.7416
9424	3.8333	4.0648	0.8451	2.5909	0.1961	1.858
10283	4.0625	3.1697	0.4226	2.4886	0.1613	1.9331
10405	4.0089	2.6517	0.3826	2.9894	0.1735	1.879
10903	4.4063	4.3037	0.0315	2.1379	0.1363	2.0663
10904	4.32	2.9976	0.3217	2.9326	0.1692	1.9258
10927	4	2.7085	0.5815	3.2377	0.1752	1.8793
13565	4.2605	4.2935	0.1602	2.1506	0.1351	2.0676
mean	3.986825	3.529488	0.509213	2.787713	0.172988	1.918838
sd	0.41224	0.670239	0.386974	0.523605	0.030812	0.101484
SEM	0.155812	0.253326	0.146262	0.197904	0.011646	0.038357

Appendix B: Results of Run Length Matrices

Part 1: Theoretical Explanation of Run Length Matrices

For an image, the run length matrix $p(i, j)$ is explained as the number of runs with pixels having gray value i and run length j.

Short Run Emphasis

The short run emphasis feature measures the distribution of short runs and is expected to be large for fine textures. SRE is given by the equation below:

$$SRE = \frac{1}{n_r}\sum_{i=1}^{M}\sum_{j=1}^{N}\frac{p(i, j)}{j^2} = \frac{1}{n_r}\sum_{j=1}^{N}\frac{p_r(j)}{j^2} \quad \text{(B.1)}$$

Where:

n_r is the total number of runs in the image

M is the number of gray levels in the image

N is the number of run lengths

Long Run Emphasis

The LRE is dependent on the occurrence of long runs and is expected to be large for coarse textures. LRE is given by the equation below

$$LRE = \frac{1}{n_r}\sum_{i=1}^{M}\sum_{j=1}^{N}p(i, j).j^2 = \frac{1}{n_r}\sum_{j=1}^{N}p_r(j).j^2 \quad \text{(B.2)}$$

Gray- Level Non-uniformity (GLN)

GLN measures the similarity in the gray level values across the image. If the GLN value is low, it means the gray-level values are similar through the image. GLN is given by the equation below

$$GLN = \frac{1}{n_r}\sum_{i=1}^{M}\left(\sum_{j=1}^{N} p(i,j)\right)^2 = \frac{1}{n_r}\sum_{i=1}^{M} p_g(i)^2 \quad \text{(B.3)}$$

Run length Non-uniformity (RLN)

RLN measures the similarity of the length of runs across the image. A low RLN value signifies that the run lengths are similar across the image. RLN is given by the equation below:

$$RLN = \frac{1}{n_r}\sum_{i=1}^{M}\left(\sum_{j=1}^{N} p(i,j)\right)^2 = \frac{1}{n_r}\sum_{j=1}^{N} p_r(i)^2 \quad \text{(B.4)}$$

Run Percentage (RP)

RP is the measure of homogeneity and the distribution of runs in any given direction in the image. The equation of RP is given below:

$$RP = \frac{n_r}{n_p}$$

Low Gray -Level Run Emphasis (LGRE)

LGRE measures the distribution of low gray level values in the image and is given by the equation below:

$$LGRE = \frac{1}{n_r}\sum_{i=1}^{M}\sum_{j=1}^{N}\frac{p(i,j)}{i^2} = \frac{1}{n_r}\sum_{i=1}^{M}\frac{p_g(i)^2}{i^2} \quad \text{(B.5)}$$

High Gray Level Run Emphasis (HGRE)

HGRE measures the distribution of high gray level values in the image and is given by the equation below:

$$LGRE = \frac{1}{n_r}\sum_{i=1}^{M}\sum_{j=1}^{N} p(i,j).i^2 = \frac{1}{n_r}\sum_{i=1}^{M} p_g(i)^2.i^2 \quad \text{(B.6)}$$

Part 2: Results of Run Length Matrices in the Median Nerve

Table B.1: Short Run Emphasis (SRE) & Long Run Emphasis (LRE) Values of the Median Nerve

CODE	SRE				LRE			
	Prox	RU	Distal	P+M+D	Prox	RU	Distal	P+M+D
816	0.8467	0.8162	0.8879	2.5508	1.9371	2.1716	1.5225	5.6312
10195	0.8264	0.8719	0.8632	2.5615	1.8231	1.7513	1.755	5.3294
10414	0.8509	0.8859	0.8806	2.6174	1.7565	1.6342	1.5908	4.9815
10709	0.8594	0.8581	0.8208	2.5383	1.6442	1.814	2.0033	5.4615
10886	0.8622	0.8784	0.859	2.5996	1.6689	1.5423	1.7548	4.966
11329	0.886	0.8077	0.854	2.5477	1.6347	2.3092	1.8956	5.8395
11345	0.8985	0.85	0.8356	2.5841	1.5573	1.9561	2.0749	5.5883
11417	0.865	0.8179	0.8444	2.5273	1.6474	2.1429	1.7477	5.538
14779	0.8839	0.8758	0.799	2.5587	1.5912	1.6619	2.2337	5.4868
14801	0.7946	0.8556	0.882	2.5322	2.2878	1.7935	1.5522	5.6335
14817	0.8677	0.8456	0.8713	2.5846	1.729	1.8831	1.6451	5.2572
14850	0.8558	0.8606	0.8342	2.5506	1.7868	1.7855	1.9504	5.5227
14898	0.8112	0.8378	0.7528	2.4018	2.0131	1.9974	2.9101	6.9206
mean	0.854485	0.850885	0.844985	2.550354	1.775162	1.880231	1.895085	5.550477
sdev	0.028404	0.024131	0.036358	0.050006	0.195399	0.21791	0.357826	0.463162
SEM	0.007878	0.006693	0.010084	0.013869	0.054194	0.060437	0.099243	0.128458
CODE	SRE				LRE			
	Prox	RU	Distal	P+M+D	Prox	RU	Distal	P+M+D
8577	0.876	0.814	0.7744	0.821467	1.6514	2.4676	2.9791	2.366033
9424	0.8924	0.8859	0.8484	0.875567	1.4963	1.5643	1.7928	1.6178
10283	0.8763	0.8783	0.8729	0.875833	1.6076	1.623	1.5789	1.603167
10405	0.8671	0.7614	0.8447	0.8244	1.6416	2.63787	1.8767	2.052057
10903	0.853	0.8525	0.8454	0.8503	1.9252	1.856	1.5717	1.7843
10904	0.8668	0.8635	0.8714	0.867233	1.6835	1.6858	1.5996	1.6563
10927	0.7296	0.8796	0.9086	0.839267	3.8929	1.5152	1.4214	2.2765
13565	0.887	0.8367	0.9667	0.8968	1.5429	2.0488	2.1333	1.908333
mean	0.856025	0.846488	0.866563	0.856358	1.930175	1.924821	1.869188	1.908061
sdev	0.049148	0.039336	0.051971	0.025173	0.751369	0.398301	0.468176	0.278867
SEM	0.017376	0.013907	0.018375	0.0089	0.265649	0.140821	0.165525	0.098594
TTest	0.941059	0.79422	0.353356	0.0000	0.607777	0.79048	0.901553	0.0000

Table B.2: Run Percentage(RP) & Run Length Non-Uniformity(RLN) Values of the Median Nerve

CODE	RP				RLN			
	Prox	RU	Distal	P+M+D	Prox	RU	Distal	P+M+D
816	3.2407	3.0727	3.3182	3.210533	235.0971	209.6923	381.1292	275.3062
10195	3.25	3.3056	3.4538	3.336467	166.2923	426.2807	314.461	302.3447
10414	3.3583	3.2662	3.4417	3.3554	273.4864	373.6759	304.799	317.3204
10709	3.2929	3.3077	3.1302	3.2436	226.0982	356.7171	377.6356	320.1503
10886	3.4846	3.5444	3.2443	3.424433	316.3113	232.1285	395.6375	314.6924
11329	3.3182	2.9008	3.1619	3.126967	325.5388	444.1464	481.6516	417.1123
11345	3.4909	3.162	3.0926	3.2485	294.8542	462.6867	435.8982	397.813
11417	3.4667	3.15	3.4154	3.344033	219.4744	236.127	293.527	249.7095
14779	3.5333	3.3681	2.9481	3.283167	234.8553	350.7773	472.7462	352.7929
14801	2.9852	3.2517	3.4359	3.224267	236.7469	319.3527	390.6294	315.5763
14817	3.3545	3.1825	3.3497	3.295567	261.5149	307.1521	342.4781	303.715
14850	3.2222	3.3021	3.0714	3.198567	219.163	441.1041	419.3597	359.8756
14898	2.974	3.0437	2.6767	2.898133	281.0044	303.444	374.6348	319.6944
mean	3.3055	3.219808	3.210762	3.245356	253.1106	343.3296	383.4298	326.6233
sdev	0.17019	0.156009	0.220735	0.125455	42.71822	81.89959	57.30147	43.98518
SEM	0.047202	0.043269	0.061221	0.034795	11.8479	22.71486	15.89257	12.1993
CODE	RP				RLN			
	Prox	RU	Distal	P+M+D	Prox	RU	Distal	P+M+D
8577	3.3642	2.9583	2.1814	2.834633	394.5046	438.3127	505.5919	446.1364
9424	3.3471	3.4427	3.2176	3.3358	305.5333	490.649	468.5281	421.5701
10283	3.3997	3.3561	3.5	3.4186	457.6962	637.3047	477.2707	524.0905
10405	3.3227	2.8669	3.2431	3.144233	517.0109	523.7307	703.8653	581.5356
10903	3.1031	3.2436	3.2265	3.191067	420.0276	517.2187	504.9868	480.7444
10904	3.4941	3.3813	3.3646	3.413333	419.9259	758.2187	692.6821	623.6089
10927	2.4	3.6667	3.2449	3.103867	382.8452	396.3788	125.1132	301.4457
13565	3.40228	2.9286	3.75	3.360293	482.3143	407.3537	582.1111	490.593
mean	3.229148	3.230525	3.216013	3.225228	422.4823	521.1459	507.5187	483.7156
sdev	0.330443	0.267261	0.427196	0.186502	61.03178	115.1224	168.4788	93.08713
SEM	0.116829	0.094491	0.151037	0.065939	21.57799	40.70192	59.56624	32.91127
TTest	0.583037	0.924751	0.976512	0.804304	0.0000	0.004135	0.096211	0.002392

Table B.3: High Gray Level Run Emphasis (HGRE) values of the Median Nerve

CODE	HGRE			P+M+D
	Prox	RU	Distal	
816	40.4743	46.2071	44.9687	43.88337
10195	35.5769	56.7882	37.9176	43.42757
10414	46.1861	42.0775	68.9952	52.4196
10709	35.9448	44.2558	59.6689	46.62317
10886	34.9382	26.5611	50.9405	37.47993
11329	39.7169	90.2093	108.0783	79.33483
11345	29.6327	64.7247	79.0299	57.79577
11417	30.641	39.2963	39.4775	36.4716
14779	29.9434	51.3876	130.9472	70.7594
14801	74.4094	44.4667	80.8731	66.58307
14817	34.1003	73.2646	35.5511	47.63867
14850	36.1223	67.7571	63.6233	55.83423
14898	41.2576	85.9596	104.0927	77.1033
mean	39.14953	56.3812	69.55108	55.02727
sdev	11.17153	18.20105	28.83619	13.89671
SEM	3.098424	5.048064	7.997721	3.854255
CODE	HGRE			
	Prox	RU	Distal	P+M+D
8577	44.6257	83.8113	103.473	77.30333
9424	41.0642	58.1952	67.6446	55.63467
10283	56.2816	81.07	59.9865	65.77937
10405	56.409	163.5779	119.0797	113.0222
10903	67.3545	68.0856	77.6887	71.04293
10904	49.7003	97.6063	91.4107	79.57243
10927	49.1667	12.6667	14.9874	25.60693
13565	64.6327	23.2073	78.4	55.41333
mean	53.65434	73.52754	76.58383	67.9219
sdev	8.649499	43.80691	29.37427	23.37229
SEM	3.05806	15.48808	10.38537	8.263352
TTest	0.005564	0.351091	0.619948	0.213534

Table B.4: Mean values of the extracted RLM features of the median nerve (Proximal Location)

	SRE	LRE	RP	RLN	LGRE	HGRE
Controls	**0.8544**	**1.7751**	**3.3055**	**253.1105**	**60.6177**	**39.3033**
Patients	**0.8560**	**1.9301**	**3.2291**	**422.4822**	**68.9045**	**53.6543**

Table B.5: Mean values of the extracted RLM features of the median nerve (RU Joint)

	SRE	LRE	RP	RLN	LGRE	HGRE
Controls	**0.8508**	**1.8802**	**3.2198**	**343.3296**	**48.2365**	**56.3812**
Patients	**0.8464**	**1.9248**	**3.2305**	**521.1458**	**48.2365**	**73.5275**

Table B.6: Mean values of the extracted RLM features of the median nerve (Distal Location)

	SRE	LRE	RP	RLN	LGRE	HGRE
Controls	0.8449	1.8950	3.2107	383.4297	52.5496	69.5510
Patients	0.8665	1.8691	3.2160	507.5186	56.8736	76.5838

Part 3: Results of Run Length Matrices in the Brachial Plexus

Table B.7: Mean RLM values of the Brachial Plexus

	SRE										
	LC5	LC6	LC7	LC8	L-Avg	RC5	RC6	RC7	RC8	R-Avg	L+R
Controls	0.7896	0.7983	0.8081	0.7988	0.7990	0.7993	0.7939	0.7336	0.7837	0.7778	1.5767
Patients	0.7776	0.7863	0.7857	0.7646	0.7787	0.7756	0.7693	0.7722	0.7462	0.7648	1.5435

	LRE										
	LC5	LC6	LC7	LC8	L-Avg	RC5	RC6	RC7	RC8	R-Avg	L+R
Controls	2.4665	2.3415	2.2827	2.5285	2.3830	2.2660	2.4566	2.5428	2.2849	2.3906	4.7737
Patients	2.4192	2.6096	2.5029	2.7872	2.5921	2.6835	2.7472	2.6009	3.3517	2.8603	5.4525

	RP										
	LC5	LC6	LC7	LC8	L-Avg	RC5	RC6	RC7	RC8	R-Avg	L+R
Controls	2.9311	2.9915	3.0004	2.9279	2.9711	2.9856	2.9171	2.8928	2.8768	2.9172	5.8884
Patients	2.9283	2.8818	2.8984	2.7538	2.8598	2.8537	2.8297	2.8675	2.6403	2.7924	5.6522

	RLN										
	LC5	LC6	LC7	LC8	L-Avg	RC5	RC6	RC7	RC8	R-Avg	L+R
Controls	198.05	207.80	234.28	228.02	214.99	218.38	222.09	259.81	227.51	236.73	451.72
Patients	219.79	300.22	314.81	331.76	299.25	267.49	308.14	332.18	289.66	302.00	601.25

	LGRE										
	LC5	LC6	LC7	LC8	L-Avg	RC5	RC6	RC7	RC8	R-Avg	L+R
Controls	22.19	25.41	26.07	23.93	24.42	23.54	21.35	22.22	24.83	22.89	47.32
Patients	22.02	19.75	25.07	23.72	22.89	20.88	22.33	24.27	21.80	22.30	45.20

	HGRE										
	LC5	LC6	LC7	LC8	L-Avg	RC5	RC6	RC7	RC8	R-Avg	L+R
Controls	49.97	48.21	54.45	57.09	51.83	51.75	58.19	70.22	53.74	59.58	111.41
Patients	54.98	73.05	82.33	91.98	77.53	73.09	79.09	83.79	84.88	80.64	158.17

Appendix C: Plots of the Autocorrelation Function

Figure C.1: The Autocorrelation Function of a patient nerve

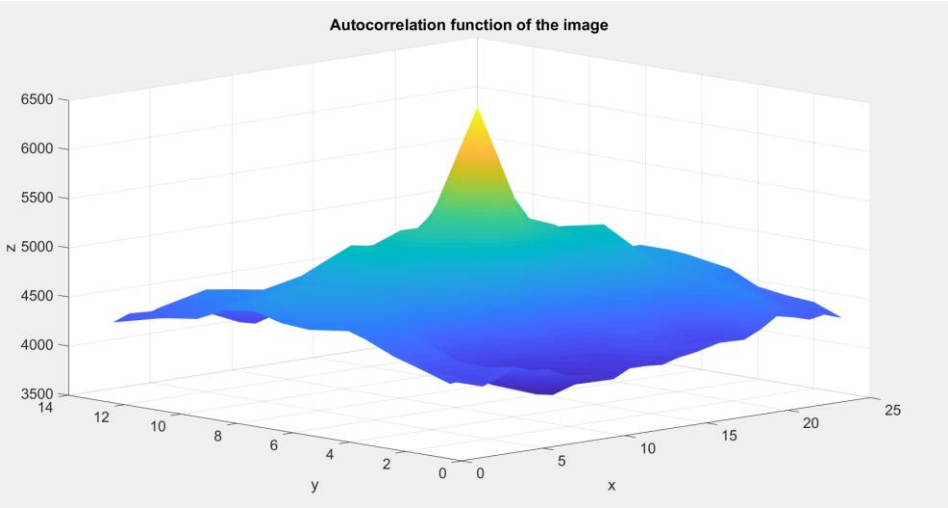

Figure C.2 The Autocorrelation signature of the x-axis in a patient nerve

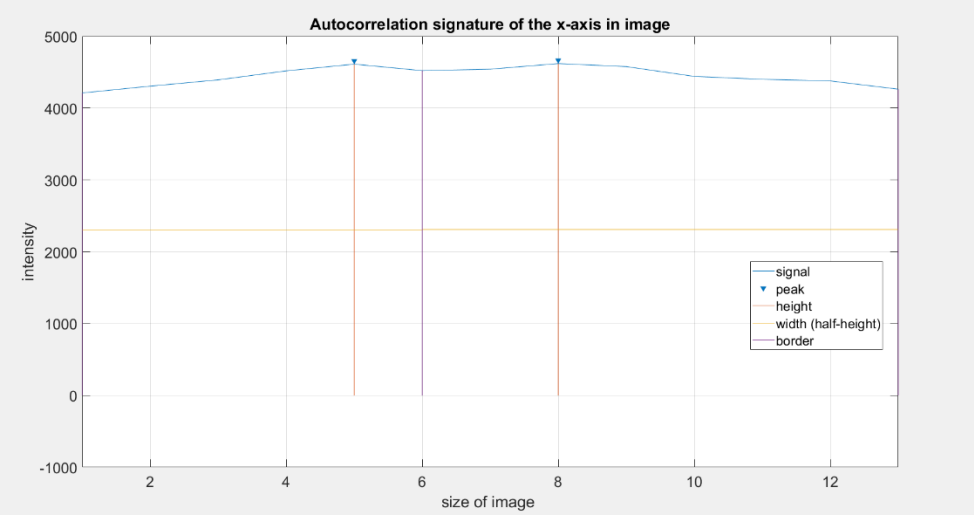

Figure C.3: The Autocorrelation signature of the y-axis in a patient nerve

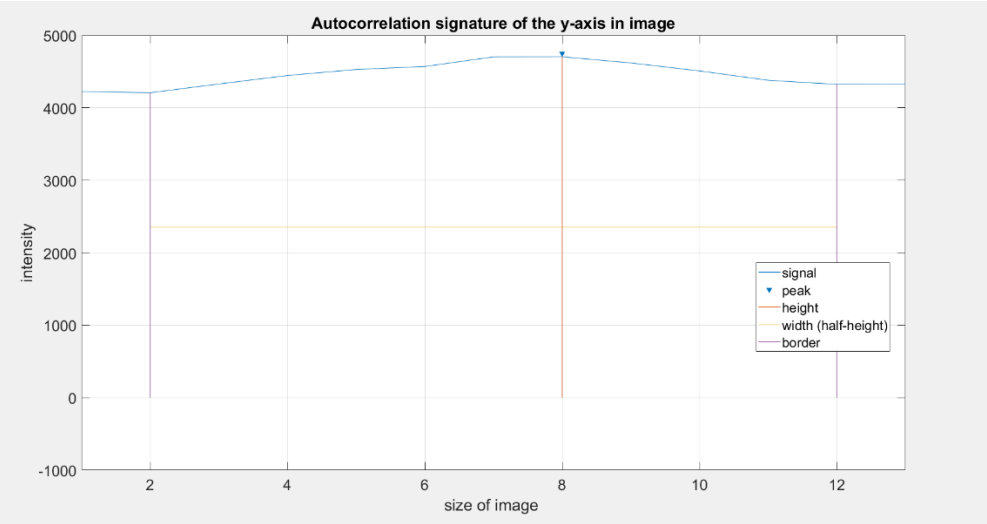

Figure C.4: The Autocorrelation Function of a patient nerve

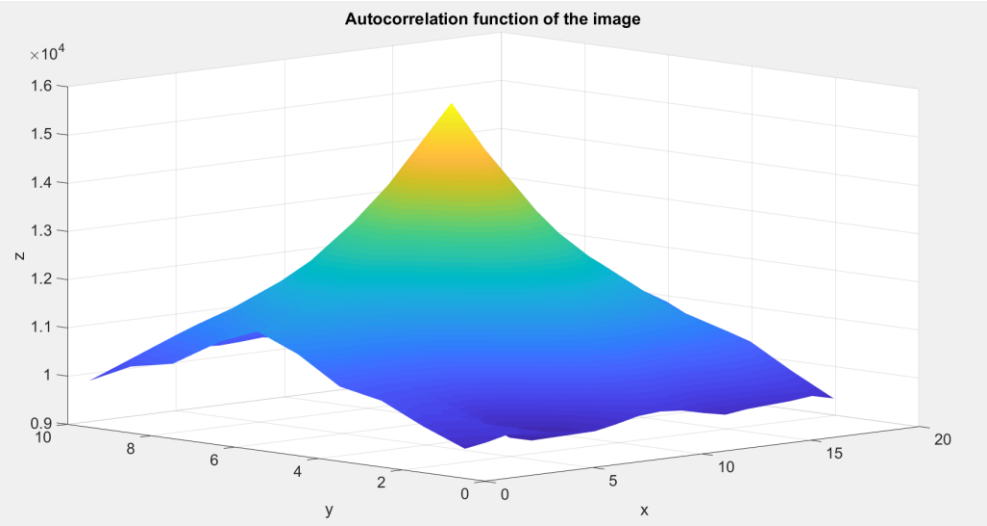

Figure C.5 The Autocorrelation signature of the x-axis in a patient nerve

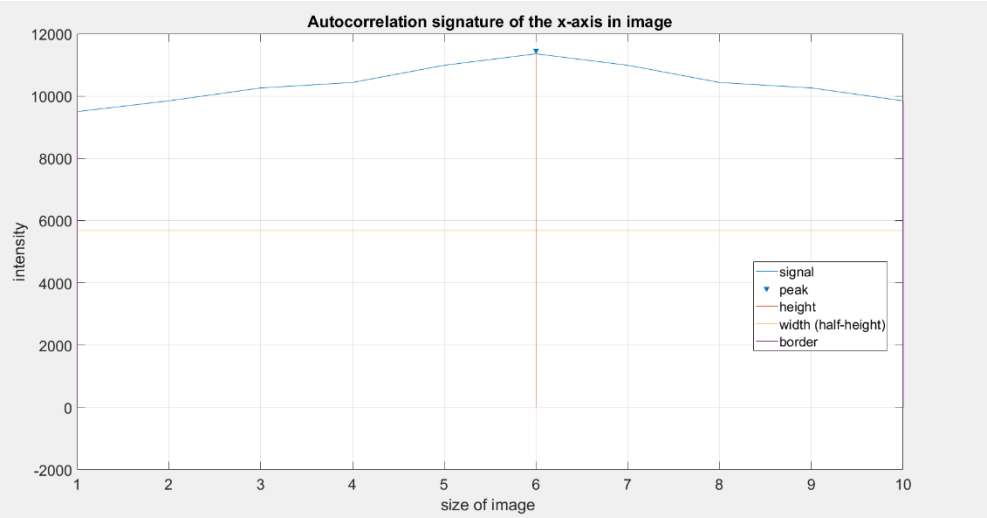

Figure C.6: The Autocorrelation signature of the y-axis in a patient nerve

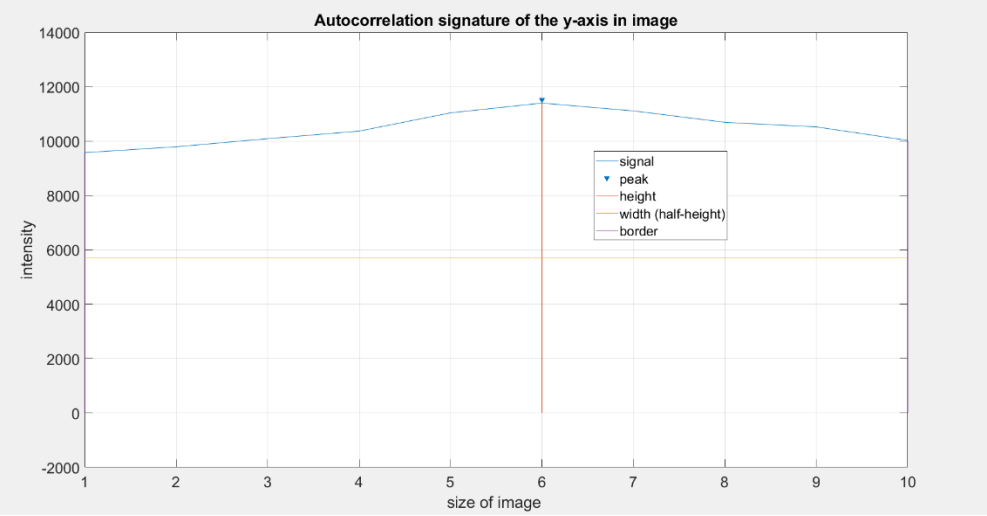

Figure C.7: The Autocorrelation Function of a control nerve

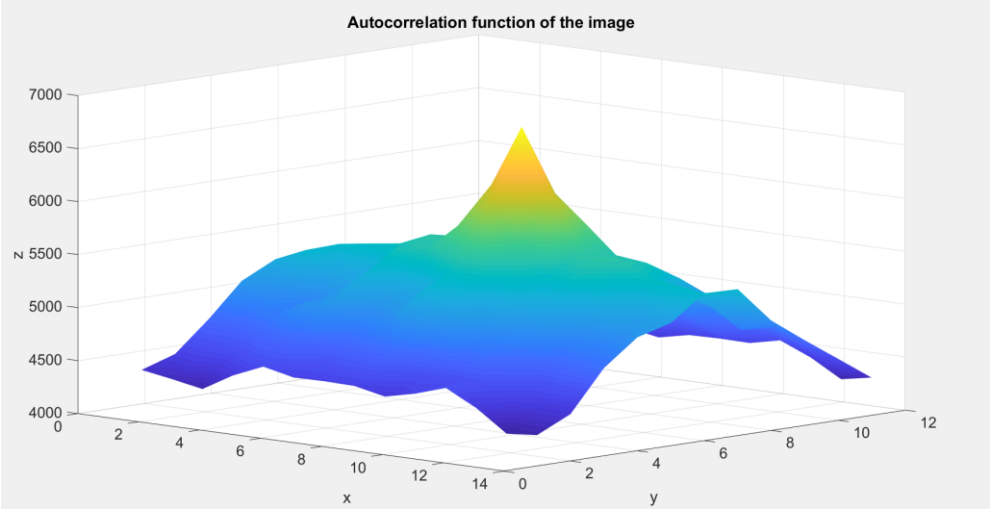

Figure C.8: The Autocorrelation signature of the x-axis in a control nerve

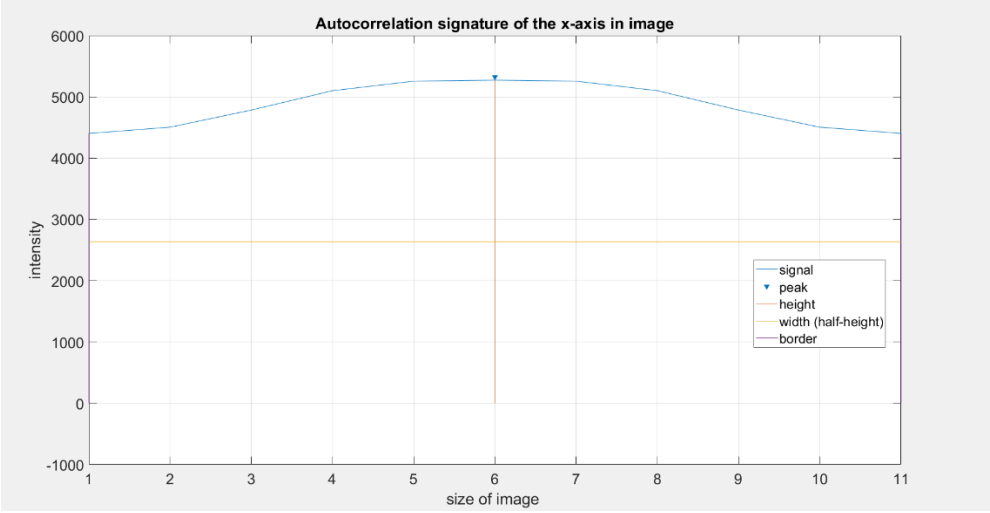

Figure C.9 The Autocorrelation signature of the y-axis in a control nerve

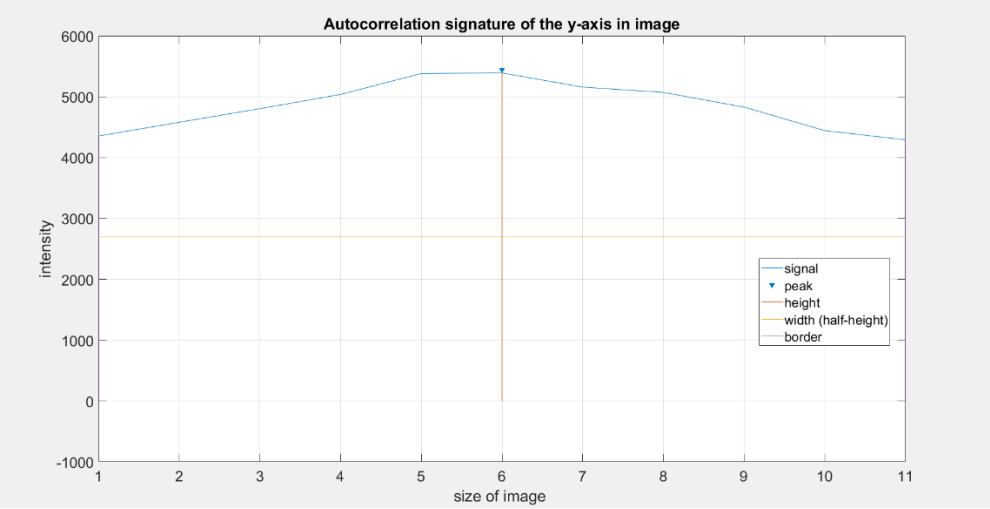

Figure C.10: The Autocorrelation Function of a control nerve

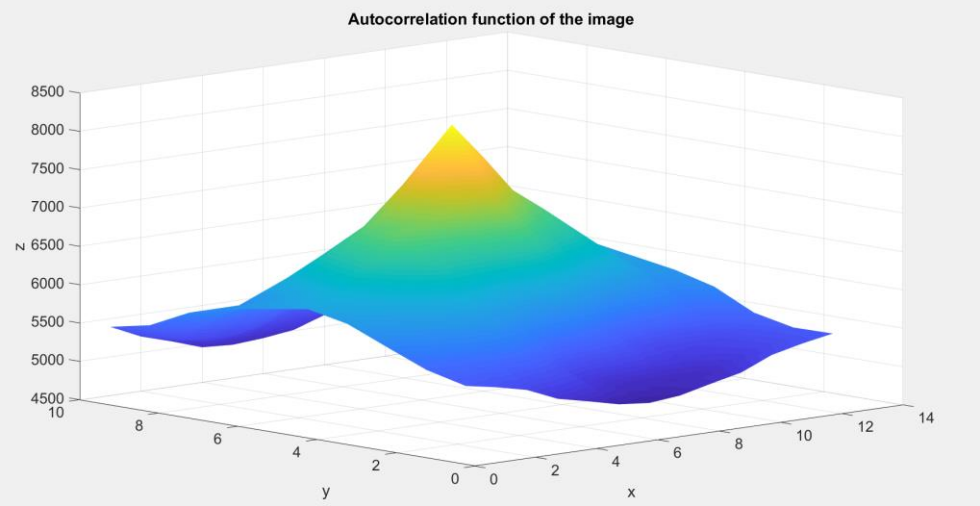

Figure C.11: The Autocorrelation signature of the x-axis in a control nerve

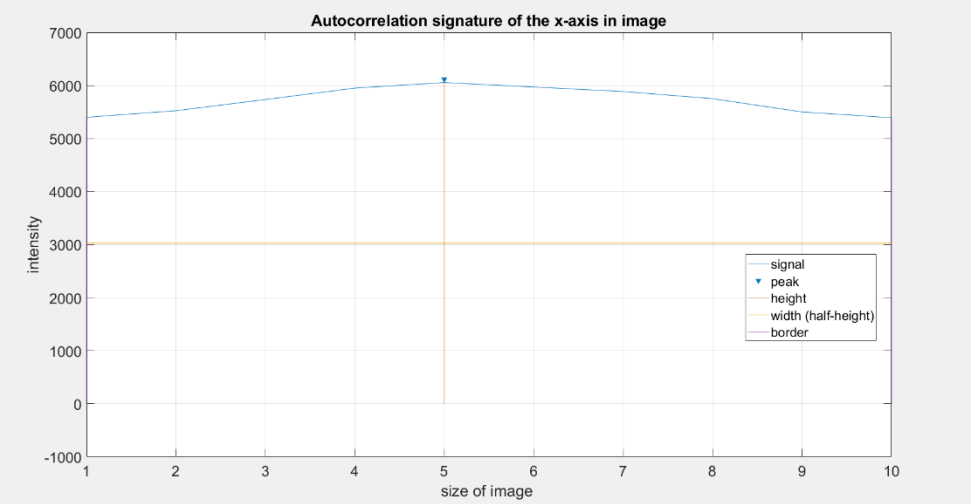

Figure C.12: The Autocorrelation signature of the y-axis in a control nerve

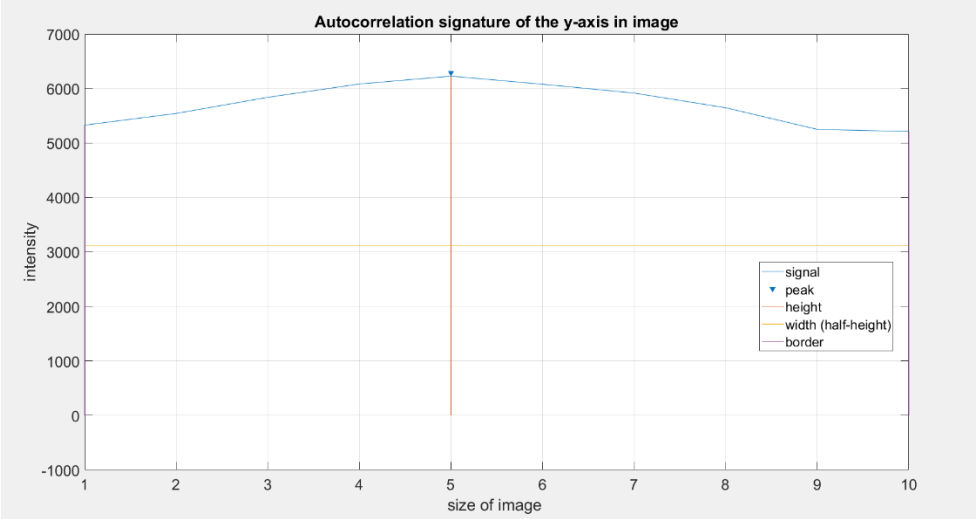

Appendix D: Results of Shape Metrics

Table D.1: Shape Metrics of the Median Nerve at the Proximal Location

Code	PROXIMAL				
	Eccentricity	Circularity	Area	Area (mm2)	Aspect Ratio
8577	0.9047	0.722279389	310.602	6.609	2.347571499
9424	0.6884	1.109762813	219.405	5.555	1.378649507
10283	0.9211	0.757164036	250.926	5.940	2.568456917
10405	0.863	0.485845779	476.666	8.187	1.979076965
10452					
10903	0.9415	0.670735328	307.212	6.573	2.967078333
10904	0.9009	0.851579108	266.850	6.126	2.304382916
10927	0.8991	0.544162658	664.922	9.670	2.284743579
13565	0.8373	0.839662902	335.828	6.872	1.828899179
816	0.7513	1.011630418	222.178	5.590	1.515237566
10195	0.5782	1.176658225	124.612	4.186	1.225614794
10414	0.7066	1.021118024	234.834	5.747	1.413177687
10709	0.494	1.15600171	204.465	5.362	1.150094382
10886	0.6238	1.126706855	176.407	4.981	1.279400444
11329	0.7447	1.015179249	178.871	5.015	1.498385867
11345	0.7159	1.14242856	147.665	4.557	1.432184751
11417	0.7158	1.140179774	136.573	4.382	1.432100334
14779	0.5443	1.100249783	201.218	5.319	1.192027503
14801	0.8183	0.994551019	239.778	5.807	1.739631928
14817	0.7537	1.068764359	176.502	4.982	1.521624646
14850	0.5647	1.023516637	157.905	4.712	1.211654013
14898	0.8043	0.924178734	291.262	6.400	1.682987295
Patient MEAN	0.870	0.748	354.052	6.941	2.207
SD	0.080	0.195	147.579	1.354	0.482
SEM	0.028	0.069	52.177	0.479	0.170
Control MEAN	0.678	1.069	191.713	5.157	1.407
SD	0.105	0.077	47.009	0.629	0.187
SEM	0.029	0.021	13.038	0.175	0.052
T TEST	0.000	0.000	0.001	0.001	0.000

Table D.2: Shape Metrics of the Median Nerve at the Distal Location

Code	DISTAL				
	Eccentricity	Circularity	Area	Area (mm2)	Aspect Ratio
8577	0.9692	0.546205304	350.893	7.025	4.063016155
9424	0.9134	0.726314933	332.347	6.836	2.456947789
10283	0.9473	0.672795643	291.0412	6.397	3.122753227
10405	0.9452	0.538894806	427.2283	7.751	3.062062963
10452					
10903	0.946	0.658919005	236.2191	5.764	3.083760303
10904	0.8582	0.76161904	406.3962	7.560	1.948296598
10927	0.9336	0.615253931	501.4049	8.397	2.790371418
13565	0.9109	0.74568085	376.5399	7.277	2.423148016
816	0.7425	1.035009724	257.1826	6.014	1.492937205
10195	0.8315	0.855645575	229.974	5.687	1.80015368
10414	0.7796	0.993277771	383.6822	7.345	1.596697844
10709	0.858	0.871548835	336.6738	6.881	1.946854825
10886	0.8088	0.842594393	354.4331	7.060	1.700308138
11329	0.9634	0.520547676	406.6723	7.562	3.730194028
11345	0.8876	0.792357351	298.3612	6.477	2.170889904
11417	0.7178	1.080288176	255.8692	5.998	1.436180384
14779	0.5198	0.981006335	372.8161	7.241	1.170525082
14801	0.8305	0.861844484	442.6302	7.890	1.795439408
14817	0.8561	0.904300524	199.4515	5.296	1.934934795
14850	0.8015	0.878393379	277.7559	6.250	1.672342181
14898	0.8125	0.896492707	441.9761	7.884	1.715366268
Patient MEAN	0.93	0.66	365.26	7.13	2.87
SD	0.03	0.09	82.50	0.82	0.63
SEM	0.01	0.03	29.17	0.29	0.22
			11.5%	5.8%	
Control MEAN	0.80	0.89	327.50	6.74	1.86
SD	0.10	0.14	80.60	0.85	0.62
SEM	0.03	0.04	22.35	0.24	0.17
T TEST	0.00	0.00	0.31	0.31	0.00

Table D.2: Shape Metrics of the Median Nerve at the RU Joint Location

Code	RU Joint				
	Eccentricity	Circularity	Area	Area (mm2)	Aspect Ratio
8577	0.9434	0.677237478	333.7331	6.851	3.016142349
9424	0.6746	0.962292202	359.6167	7.111	1.354724658
10283	0.918	0.661554308	551.3556	8.805	2.521918941
10405	0.9385	0.444193331	553.8155	8.825	2.896328958
10452					
10903	0.896	0.605014616	271.198	6.176	2.25158675
10904	0.9252	0.643570783	599.71	9.183	2.63554861
10927	0.9337	0.613903321	686.7024	9.827	2.793788792
13565	0.8945	0.813060834	409.8407	7.592	2.23664432
816	0.7138	1.003203673	231.2487	5.703	1.427922783
10195	0.8157	0.886762063	363.3914	7.149	1.728567412
10414	0.7911	0.950567493	271.0021	6.173	1.634779257
10709	0.8543	0.878393379	271.9263	6.184	1.92377417
10886	0.6206	1.011630418	223.8098	5.610	1.27529736
11329	0.8768	0.705994935	331.5007	6.828	2.079913516
11345	0.8665	0.892797015	327.1172	6.782	2.003509453
11417	0.7945	1.027060674	199.2738	5.294	1.646618116
14779	0.6624	0.992567014	281.7632	6.295	1.3348583
14801	0.7679	1.027494828	247.8899	5.904	1.5611444
14817	0.5247	1.082516381	395.1765	7.455	1.174658395
14850	0.8517	0.863101751	248.9906	5.917	1.908097876
14898	0.6531	0.940586067	635.8486	9.456	1.320573506
Patient MEAN	0.89	0.68	470.75	8.05	2.46
SD	0.09	0.15	147.03	1.29	0.53
SEM	0.03	0.05	51.98	0.46	0.19
			51.9%	23.4%	
Control MEAN	0.75	0.94	309.92	6.52	1.62
SD	0.11	0.10	113.39	1.08	0.30
SEM	0.03	0.03	31.45	0.30	0.08
T TEST	0.01	0.00	0.01	0.01	0.00